



UNIVERSITÀ DEGLI STUDI DI BERGAMO
DEPARTMENT OF ENGINEERING AND APPLIED SCIENCE
DOCTORAL PROGRAMME IN ENGINEERING AND APPLIED SCIENCES

**SYNTHESIS AND
CHARACTERIZATION OF BIO-BASED
POLYMERS FOR INNOVATIVE
ADDITIVE MANUFACTURING
APPLICATIONS VIA
STEREOLITHOGRAPHY 3D
PRINTING**

Doctoral dissertation of:

Raphael Rosa

Tutor:

Prof. Giuseppe Rosace

The Chair of the Doctoral Program:

Prof. Alessandra Marini

XXXV Cycle

SUMMARY

SUMMARY I

ACKNOWLEDGEMENTS VII

ABSTRACT..... VIII

PUBLICATIONS..... XI

LIST OF ABBREVIATIONS XIII

CHAPTER 1 – INTRODUCTION..... 1

CHAPTER 2 – BIBLIOGRAPHIC RESEARCH..... 5

2.1 Additive Manufacture..... 5

2.1.1 Material extrusion..... 8

2.1.2 Vat polymerization 9

2.1.3 Powder bed fusion 11

2.1.4 Material jetting 12

2.1.5 Binder jetting..... 13

2.1.6 Direct energy deposition..... 15

2.1.7 Sheet lamination 16

2.1.8 3D-printing process 18

2.2 Vat polymerization 20

2.2.1 Types of vat polymerization technologies..... 20

2.2.2 Photopolymer chemistry..... 25

2.2.3	Photopolymerization reaction.....	32
2.2.4	Irradiance and exposure influence on photopolymers properties.....	39
2.3	bio-based, (bio)degradable and biocompatible materials for vat photopolymerization	40
2.3.1	Bio-based materials	41
2.3.2	(Bio)degradable materials	44
2.3.3	Biocompatible materials.....	46
2.4	Epoxy-acrylate soybean oil (AESO)	49
CHAPTER 3 – MATERIALS, METHODS, AND CHARACTERIZATIONS		53
3.1	Materials.....	53
3.1.1	Photosensitive acrylates containing bio-based epoxy-acrylate soybean oil.	54
3.1.2	Synthesis of a biobased resin for multipurpose applications.....	54
3.1.3	Synthesis of a biobased and biocompatible resin for medical applications.....	54
3.1.4	Reinforcement and characterization of biobased resins with micro- or nanocrystalline cellulose	55
3.2	Preparation of samples and characterizations.....	55
3.2.1	3D printing process	56
3.2.2	FTIR Spectroscopy	57
3.2.3	Rheological analysis.....	58
3.2.4	Tensile measurements	58
3.2.5	Scanning electron microscopy.....	59
3.2.6	Thermogravimetric analysis	59
3.2.7	Swelling analysis.....	59

3.2.8	Contact angle measurement.....	60
3.2.9	Working curve.....	60
CHAPTER 4 – PHOTSENSITIVE ACRYLATES CONTAINING BIO-BASED EPOXY-ACRYLATE SOYBEAN		
OIL	64
4.1	Introduction.....	64
4.2	Experimental part.....	69
4.2.1	Photocurable resin formulation.....	69
4.3	Results and discussion.....	69
4.3.1	FT-IR analysis.....	70
4.3.2	Rheology.....	76
4.3.3	Mechanical properties.....	77
4.3.4	Thermogravimetric analyses.....	81
4.3.5	Effect of AESO on PY wettability.....	82
4.3.6	Swelling properties.....	83
4.3.7	AESO load effect on working curve.....	85
4.3.8	Visual evaluation.....	87
4.4	Conclusions.....	88
CHAPTER 5 – SYNTHESIS OF A BIOBASED RESIN FOR MULTIPURPOSE APPLICATIONS.....91		
5.1	Introduction.....	91
5.2	Experimental part.....	93
5.2.1	Photocurable resin formulation.....	93
5.3	Results and discussion.....	94

5.3.1	FT-IR Analysis	94
5.3.2	Rheology	98
5.3.3	Mechanical properties	99
5.3.4	Effects of the AESO concentration on contact angle	103
5.3.5	Thermogravimetric analyses	104
5.3.6	Working curve	105
5.4	Conclusions	107
CHAPTER 6 – SYNTHESIS OF BIOBASED RESIN FOR BIOMEDICAL APPLICATIONS.....		109
6.1	Introduction	110
6.1.1	Vat polymerization used for medical applications	110
6.2	Experimental part	112
6.2.1	Photocurable resin formulation	112
6.3	Results and discussion.....	113
6.3.1	FT-IR analysis	113
6.3.2	Rheological behavior.....	118
6.3.3	Mechanical properties	119
6.3.4	Thermogravimetric Analysis	122
6.3.5	Contact angle.....	123
6.3.6	Swelling properties.....	125
6.3.7	PEGDA/AESO working curve	126
6.4	Conclusions	128

CHAPTER 7 – REINFORCEMENT AND CHARACTERIZATION OF BIOBASED RESINS WITH MICRO- OR NANOCRYSTALLINE CELLULOSE.....131

7.1	Introduction	132
7.1.1	Types of reinforcement fillers used in photopolymerization.....	133
7.1.1.1	Carbon nanotubes and multi-wall carbon nanotubes.....	133
7.1.1.2	Nano-clays.....	134
7.1.1.3	Ceramics.....	135
7.1.1.4	Silicates	136
7.1.1.5	Metallic particles	136
7.1.2	Lignocellulosic materials.....	137
7.2	Experimental part	139
7.2.1	Photocurable resin formulation	139
7.3	Results and discussions	139
7.3.1	Influence of nano fillers on UV curing process.....	139
7.3.2	Viscosity analyses	143
7.3.3	Mechanical properties	145
7.3.4	Scanning electron microscopy.....	148
7.3.5	Thermogravimetric characteristics	150
7.3.6	Swelling analyses	152
7.3.7	Contact angle.....	153
7.3.8	Working curve parameters	154
7.4	Conclusions	157

CHAPTER 8 – CONCLUSION AND FUTURE PERSPECTIVES	160
REFERENCES	164
LIST OF TABLES	177
LIST OF FIGURES.....	179
LIST OF SCHEMES	184

ACKNOWLEDGEMENTS

I am grateful to Prof. Giuseppe Rosace for providing me the possibility to work in his laboratory with the additive manufacturing project that I submitted. Working on this project not only improved my professional and researcher skills, but also allowed me to discover a new culture and way of living. I would also like to thank him for his expert guidance and assistance in each aspect of the research study, for precious advice, for stimulating discussions and for the confidence in me.

I wish to thank all those with which the research activities were developed, in particular to Prof. Dr. Giulio Malucelli, (Politecnico di Torino), for his support, precious suggestions, and interesting discussions. Without his assistance, I would not be able to reach this far.

I also extend my thanks to my colleagues, Dr. Claudio Colleoni, and Dr. Valentina Trovato, for supporting me with my experiments, for stimulating discussions, and for precious suggestions. Additionally, I would also like to thank both for helping me outside the university, in the times I needed the most, both were always available.

To my family in Brazil, that always were supportive with my decision of doing my PH.D. in Italy, where even distant, they motivated me to overcome difficulties and to believe in myself.

Finally, I wish to thank all those who helped me. Without them, I could not have completed my research activity.

ABSTRACT

This thesis focused on the study and development of bio-based and biocompatible photosensitive resin for stereolithography 3D printing.

The necessity for transitioning to a more environmentally friendly economy is becoming more urgent as the world population is demanding more action. Especially in the last few years, when the effects of global warming started to be more frequent. To prevent the situation from worsening, the world must decrease the use of petroleum materials. Particularly plastic, whose production and poor disposal management are causing significant damage to the oceans and marine lifeforms. Thus, it is utterly important to invest in the development of materials and technologies that can substitute or minimize its usage.

Additive manufacturing, commonly known as 3D printing, has been continuously attracting a lot of attention and investment as an alternative form to improve product production while reducing their amount of energy and raw materials. The technology consists of fabricating objects from a computer model design by depositing thin layers of materials in an incremental process. This method allows the creation of complex structures that otherwise would not be possible. Moreover, it can help decentralize production (reducing the environmental impact of long transportation), is scalable, and can fabricate different types of structures simultaneously (sometimes using different materials).

One of the seven additive manufacturing technologies, vat photopolymerization, utilizes a combination of liquid photosensitive polymers with a photoinitiator and a UV emitter to fabricate objects. The main advantage of this method is that it allows the creation of highly detailed objects. Indeed, this is the main reason why vat photopolymerization is interesting for biomedical applications, whereby combining it with other imaging techniques, it is possible to create patient-made prosthesis and implants. Unfortunately, most resins used nowadays are derived from petroleum, limiting their application.

Different types of materials were proposed to expand the variety of bio-resins. Among all, vegetable oils and plant-based resins demonstrated some promising properties. They are available worldwide and have relatively low production costs. Moreover, they can be easily functionalized to be suitable for photopolymerization. Soybean oil being a good example. Its functionalization is already used for UV coating, but its full potential in 3D printing is yet to be explored.

In this research study, the utilization of functionalized soybean oil, more precisely, acrylated epoxidized soybean oil (AESO), for 3D-printing was investigated. Here, AESO was tested for different application: from improving the biobased content of commercial a resin, to the synthesis and optimization of complete biobased and biocompatible resins.

For the first study, increasing concentrations of neat AESO were combined with Peopoly moai standard clear resin, where its influence on the resin performance was tested using different characterization techniques. Tensile test results were also compared with data from other standards of commercial resins to see how it would scale. The doping of petroleum-based resins with biobased resins is interesting since it is a simple method to increase the bio-renewable content of such materials.

However, the main objective is the transitioning from petroleum-based to complete bio resins, thus for that, in the subsequent study, AESO was combined with another plant-based material to develop a biobased resin. The mechanical and curing properties of this new resin were again compared with various standard resins to verify its performance. Furthermore, other characterization analyzes were done to better understand its photopolymerization reaction and final application.

Based on the information obtained from developing a biobased resin, AESO was used for creating a biocompatible resin. For that, it was combined with a known biocompatible material, poly(ethylene) diacrylate, and different physical and chemical properties were studied. Furthermore, the mixture which demonstrated the best performance was used in a following study that had the objective to add nanoparticles to improve its mechanical properties. The fillers used were micro- and nano-crystalline cellulose, a natural material that has already shown remarkable properties at low dosages.

The studies presented in this work are only the beginning. Further research needs to be carried out to test the performance of the biocompatible resins developed in cell cultures. Future perspectives can also consist of the evaluation of different vegetable oils, or the usage of non-food related materials (ex: algae) to develop these new bio-resins. Additionally, other types of particles can be explored as well to add new properties, such as flame retardancy, conductivity, memory shape, and others.

PUBLICATIONS

● PEER REVIEWED

1. Palucci Rosa, R. and Rosace, G. (2021), Nanomaterials for 3D Printing of Polymers via Stereolithography: Concept, Technologies, and Applications. *Macromol. Mater. Eng.* 2100345. <https://doi.org/10.1002/mame.202100345>
2. Rosace, G., Palucci Rosa, R., Arrigo, R., Malucelli, G., *J Appl Polym Sci* 2021, Photosensitive acrylates containing bio-based epoxy-acrylate soybean oil for 3D printing application. 138(44), e51292. <https://doi.org/10.1002/app.51292>
3. Palucci Rosa R, Rosace G, Arrigo R, Malucelli G. Preparation and Characterization of 3D-Printed Biobased Composites Containing Micro- or Nanocrystalline Cellulose. *Polymers*. 2022; 14(9):1886. <https://doi.org/10.3390/polym14091886>
4. Palucci Rosa R, Rosace G, Arrigo R, Malucelli G. Preparation and Characterization of a Fully Biobased Resin System for 3d-Printing, Suitable for Replacing Fossil-Based Acrylates. *J Polym Res* **30**, 139 (2023). <https://doi.org/10.1007/s10965-023-03523-x>

● **CONFERENCE PROCEEDINGS**

1. XII Congresso Nazionale Associazione Italiana Chimica per L'ingegneria - AICIng 2021 -
Poster titled: "Sintesi di una resina biobased per applicazioni in stereolitografia"
2. XXIV Convegno Nazionale dell'associazione Italiana di Scienza e Tecnologia delle
Macromolecole: "*Investigation of epoxy-acrylate soybean oil as a bio-enhancer for 3D-printing
application*", Trento 04 September 2022
3. XXIV Convegno Nazionale dell'associazione Italiana di Scienza e Tecnologia delle
Macromolecole: "*Evaluation of a biobased resin with micro- or nanocrystalline cellulose for
3D-printing application*", Trento 04 September 2022

LIST OF ABBREVIATIONS

2PP or TPP	Two-photon polymerization
ABS	Acrylonitrile Butadiene Styrene
AESO	Acrylated Epoxidized Soybean Oil
AM	Additive Manufacturing
ANOVA	One-Way Analysis of Variance
ATR	Attenuated Total Reflectance
BC	Bio-content
Bis-GMA	Bisphenol A-Glycidyl Methacrylate
BJ	Binder Jetting
BRC	Bio-renewable Carbon
CA	Contact Angle
CAD	Computer-Aided Design
CLIP	Continuous Light Interface Production
CNC	Cellulose Nanocrystals
CNT	Carbon Nanotubes
DED	Direct Energy Deposition
DLP	Digital Light Processing
DMD	Digital Micromirror Device
DMLS	Direct Metal Laser Sintering
DW	Direct Writing
EBM	Electron Beam Melting
EPU	Elastomeric Polyurethane
ESOA	Epoxidized Soybean Oil Acrylate

ESOMA	Epoxidized Soybean Oil Methacrylate
FDM	Fused Deposition Modeling
FEP	Fluorinated Ethylene Propylene
FFF	Fused Filament Fabrication
FTIR	Fourier-Transform Infrared Spectroscopy
GelMA	Gelatin Methacryloyl
GMD	Generate Glycerol Dimethacrylate
IBOMA	Isobornyl Methacrylate
LCD	Liquid Crystal Display
LCD-DLP	Light Crystal Displays Digital Light Processing
LDM	Liquid Deposition Modeling
LOM	Sheet Lamination or Laminated Object Manufacture
MCC	Micro Crystalline Cellulose
MJ	Material Jetting
MJF	Multi Jet Fusion
MMA	Methyl Methacrylate
MV	Methacrylated Vanillin
MWCNT	Multiwalled Carbon Nanotubes
PA	Polyamide
PBF	Power Bed Fusion
PC	Polycarbonate
PDMS	Polydimethylsiloxane
PE	Polyethylene
PEG	Poly(ethylene) Glycol
PEGDA	Poly(ethylene glycol) diacrylate
PLA	Poly(lactic Acid)

PP	Polypropylene
PPF	Poly(propylene) Fumarate
PTMC	Poly(trimethylene carbonate)
PVC	Polyvinylchlorid
PY	Peopoly Moai standard clear resin
SBO	Soybean Oil
SEM	Scanning Electron Microscope
SL	Stereolithography
SLA	Stereolithography Apparatus
SLS	Selective Laser Sintering
STL	Standard Tessellation Language
TEGDMA	Triethylene Glycol Dimethacrylate
TG	Thermogravimetric
TPO	Diphenyl(2,4,6-Trimethylbenzoyl) Phosphine Oxide
VP	Vat Photopolymerization

CHAPTER 1

INTRODUCTION

The history of manufacturing goes back centuries, before the advent of machines and robots, where skilled artisans would work on their products by hand. These crafters usually would have some apprentices to help them with the tasks, and in exchange for their services they would learn and become artisans themselves. At that time, the secrets of their products were confined to their family or to a guild, which assured that no one could copy their work. Because of the small scale and manual labor characteristics of the process, it usually took a lot of time to fabricate complex products.

The changes in the manufacturing process would only come in the 18th century, with the first industrial revolution. Machines substituted some of the processes that were hand-made, allowing products to be fabricated in large amounts. It was during that time period that the American system of manufacturing appeared, where the industries would be divided into sectors, and employees only needed to perform a single task. This methodology of mass product fabrication and stocking would continue to be employed until 1960s, when a system known as “just-in-time” started to be implemented. Under this new system, the parts would only be

fabricated according to the demand, without the need for stocking, thus saving a lot of money. In the following decades, many companies began to adopt this method. Then in the late 2000s, companies started to move their manufacture lines to different countries, taking advantage of cheap labor in order to fabricate their components, reducing the cost even more. However, since most of the parts were fabricated on-demand and in different parts of the world, any disruption (or delay) of the supply chain could provoke a global shortage of products.

Recently, a new industrial revolution has started, and new forms of technologies are being developed. Among them, additive manufacturing (AM) is getting a lot of attention by its potential and capability to revolutionize various industrial sectors. Commonly known as 3D-printing, AM is defined as the process of creating objects from a 3D model by incrementally adding layers upon layers of materials. This technology has become predominantly used in high value-added industries such as aerospace, automotive, and biomedical, where highly complex and customized designs are required.^[1]

Besides being used for industrial applications, AM has been growing in popularity in education and for personal use. Schools are starting to adopt it to provide new ways for students to visualize problems and improve their understating of science and mathematics.^[2] Furthermore, there has been a lot of research of using AM for special education to create objects for children with motion or visual imparities.^[3]

Additive manufacturing has just started to be implemented, but as the technology becomes more affordable and new applications are developed one can expect an increase in its demand. According to a Grand View Research 2021 report, AM had a global market size valued at USD 13.84 billion and it is projected to grow annually by 20.8% for the next 6 years, reaching a gross value of \$76.16 billion by 2030.^[4] The stereolithography segment dominated the market and accounted for more than 8% of the entire revenue share. Moreover, compared to the 2020 report ^[5], there has been an increase in the AM market growth by 40.5%, even during the COVID-19 global crisis, showing the resilience of AM to adapt to new challenges.

Although the market growth prospective of AM is positive and many companies are starting to implement the technology, there is a growing concern among many scientists regarding its consumption and production of plastics. According to Zhu et al. 2021, the plastic consumption for AM in 2020 was approximately 18,500 tons, where the most common materials were polymers such as polylactic acid (PLA), acrylonitrile butadiene styrene (ABS), polyamide (PA), polycarbonate (PC).^[6] Even though some polymers of this list are biobased and under certain conditions are degradable (like PLA), the other materials could still end up polluting the environment. Furthermore, the problem becomes even more significant as domestic use increases, in which without proper handling, their residues could be incorrectly disposed, ending up land fields and oceans.^[7]

Incorrect disposal of plastic is causing severe problems for marine life, and in extend, to human fishing activities and health. The amount of plastic in the oceans is so great that a new marine microbial habitat, known as “plastisphere”, was created. The 2021 United Nations Environment Programme (UNEP) report estimates that there are currently around 75-199 million tons of plastic on the oceans, where more 23-37 million tons are added each year.^[8] In the oceans, plastics are broken down into micro- and/or nano- particles and can end up acting as vectors for pathogenic organisms harmful to humans, fish and aquaculture stocks. Therefore, it is fundamental to develop materials that are not only biobased but also environmentally friendly.

This thesis has the objective to expand the limited number of biobased, biocompatible and (bio)degradable resins available nowadays. To that order, acrylate epoxy soybean oil (AESO), a biobased material derived from soybean oil, was used as base to develop new materials. These new materials are presented in four studies, through Chapters 4 to 7, where different challenges of developing new materials for stereolithography 3D printing are discussed.

A complete understanding of the mechanism behind the photopolymerization reaction wouldn't be possible without a theoretical background. Therefore, in the following chapter, an overview of the different types of additive manufacturing, their advantage and disadvantage, raw materials used, and applications are explored. Furthermore, a deeper analysis of vat

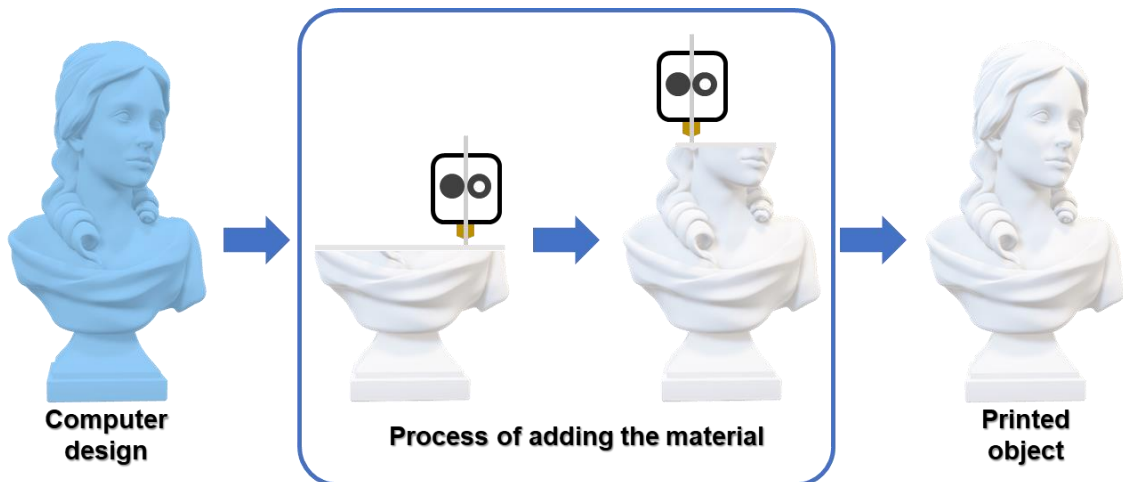
photopolymerization and stereolithography is shown, where the technological differences, the materials chemistry, their reaction process, and light influence. Finally, special attention to sustainable materials is presented, especially on the properties and usage of AESO.

CHAPTER 2

BIBLIOGRAPHIC RESEARCH

2.1 ADDITIVE MANUFACTURE

Additive manufacturing (AM), also known as solid free-form fabrication or 3D printing, is a method of creating physical objects from digital models by depositing thin layers of materials in a “layer-by-layer” process (**Scheme 1**).^[9–11] It is different from traditional subtractive manufacturing, which consists of removing material from a bulk (e.g. milling), since it uses less material, generate less waste and can produce parts more cost-effective.^[12] AM also enables their users to design more complex structures, decentralize the manufacture, create customer-specific parts, decentralize the production and quickly adapt it according to the demand.^[13–18]



Scheme 1: Layer-by-layer process of creating an object.

According to the ISO/ASTM 52900,^[19] it is possible to divide additive manufacturing process into seven categories (**Figure 1**), where each technology can fabricate objects using different types of materials (polymer/plastic, metal, ceramic, concrete, etc.).^[11,20,21] A summary of the advantages and disadvantages of each technology is shown in **Table 1**.

ADDITIVE MANUFACTURING TECHNOLOGIES

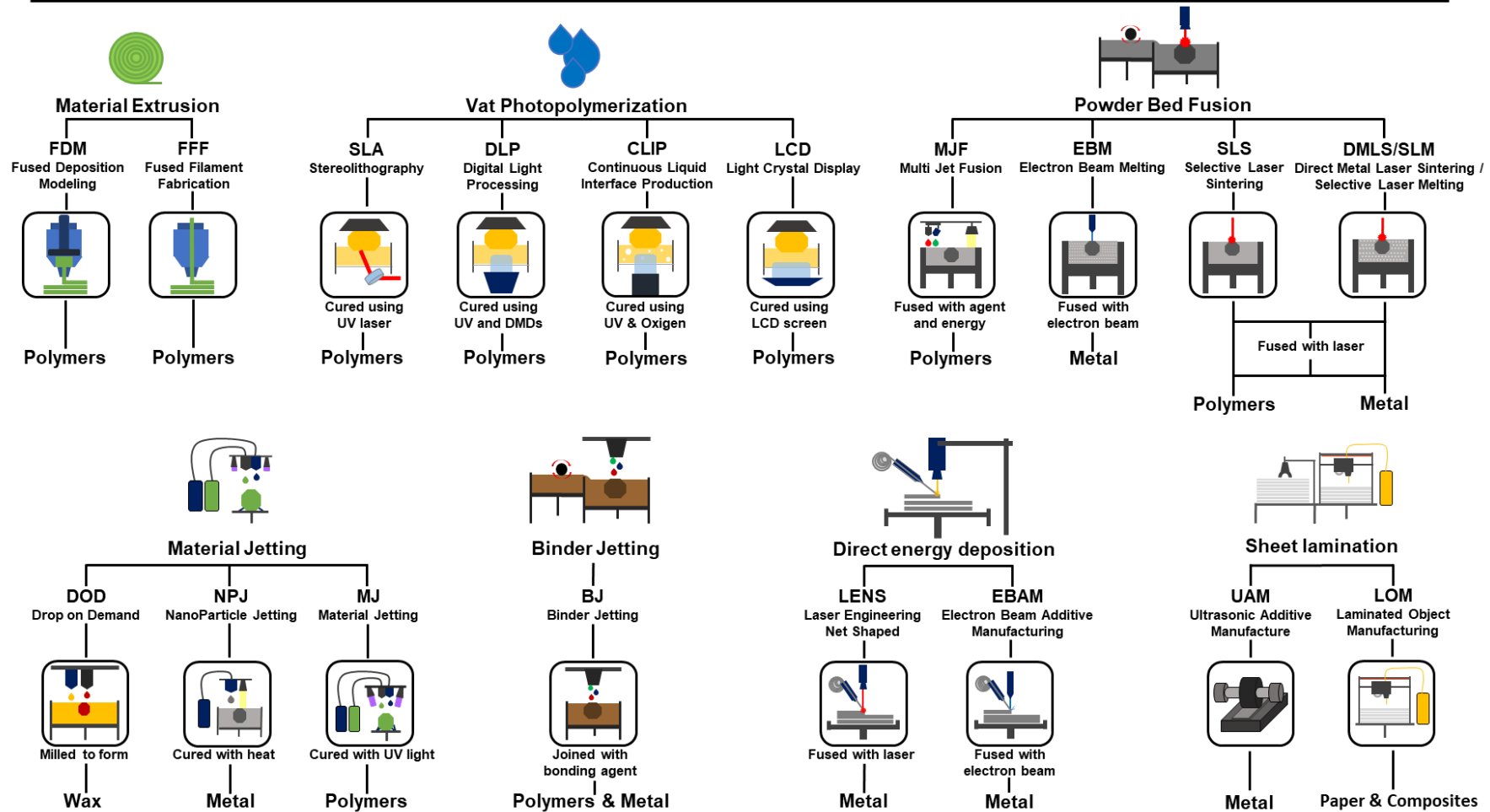


Figure 1. The seven types of additive manufacturing technologies and some of their processes according to the ISO/ASTM 52900.^[19]

2.1.1 Material extrusion

Extrusion-based printers are considered to be the most common machines on the market. Their popularity can be attributed to the expiration of many patents in 2013-2014, which lead to the arise of many companies and a drop in the printer's prices.^[22] Moreover, extrusion-based machines are capable to process a wide range of materials (polymers^[23], metals^[24], concrete^[25], food^[26], etc) and have low maintenance and feedstock cost.^[18,27]

Even though there are several types of material extrusion machines, their operational mechanisms can be divided into two major groups: (1) fused filament fabrication (FFF) and fused deposition modeling (FDM) and (2) paste extrusion.^[23] As shown by **Figure 2a**, in FFF, a filament is pushed by a set of screws (or gears) to a chamber where a heater melts it. Inside the chamber, the molten material needs to be kept as close as possible to its melting temperature, in order to avoid degradations or burns. The molten material is then pushed through a nozzle to a building platform where it solidifies. The printing platform or/and the extruder can move in the x-, y-, and z-axes to deposit the molten material accordingly to a set of coordinates (from the drawing. Finally, it is the nozzle shape and diameter that determines the size of the structure that can be created, since no structure can be smaller than its diameter.^[28]

Paste extrusion methods, such as direct writing (DW), robocasting, or liquid deposition modeling (LDM), differs from FFF because it uses viscous paste-like materials instead of filaments to print an object (**Figure 2b**). The fluid can be extruded through the nozzle by using a pump or by syringe like mechanism, where similarly to FFF, it also determines the size of the object.^[29] However, different to FFF, where the material solidifies after exiting the nozzle, in DW it normally continues liquid. Usually, the solidification occurs by evaporation of a solvent, using UV-light, or by applying heat. Furthermore, high viscous pastes are preferred for printing since them can resist better to deformations and can hold better the shape.^[29]

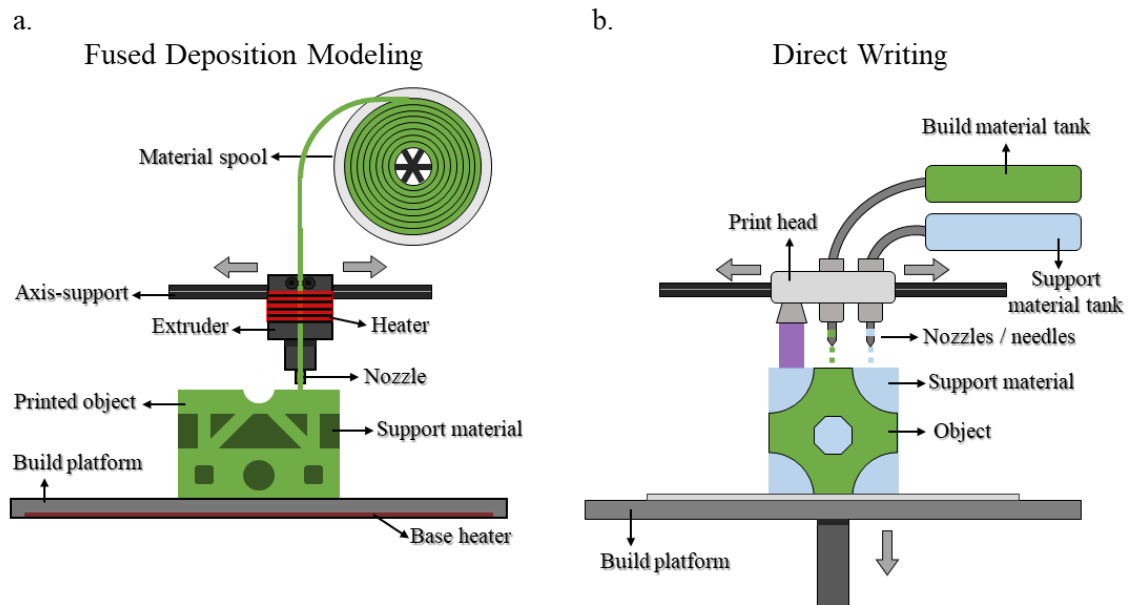


Figure 2: Schematic diagrams of two material extrusion technologies: (a) fused deposition modeling and (b) direct writing.

2.1.2 Vat polymerization

Developed in mid 1980s, vat polymerization, known as vat photopolymerization, or VP, is the oldest of the AM technologies.^[20] Its processes consist of using radiation (UV, visible light, gamma rays, X-rays or electron beams) to selectively curing a thin layer of a liquid photopolymer contained in a vat or tank (**Figure 3**). After a layer of the photosensitive liquid is cured, the building platform slowly goes down, which allows another layer of resin to be cured. This process continues until the object is finished printed. Usually, the printed object needs to be post cured under UV light to achieve its maximum performance.^[30]

Currently, there are three types of technologies that are based on vat polymerization:

1. Pointwise, or vector scan, in which a computer guided light beam cures the resin. This approach is typically used in stereolithography (SL) machines.
2. Layer-wise, or mask projector, where at each passing layer, the entire vat is irradiated with the object form. This approach is used in digital light processing

(DLP), continuous light interface production (CLIP), light crystal displays digital light processing (LCD-DLP) machines.

3. Two-photon process, which basically is a high-resolution point-by-point approach.

Where each technology has its advantages, disadvantages, applications, and materials that can be used in it. A more deeply discussion on each VP technology, as well as the photopolymerization mechanisms, is presented in section §2.2.

Compared to others AM technologies, VP has the advantage that it can fabricate high resolution objects (down to the nanoscale), with good surface finishing in a wide range of sizes.^[31] However, VP has also its drawbacks. Most of its photosensitive polymers are derived from petroleum and are toxic, needing personal protection equipment to handle. Moreover, the objects produced by this method have shown lower durability, stability, and strength.^[32]

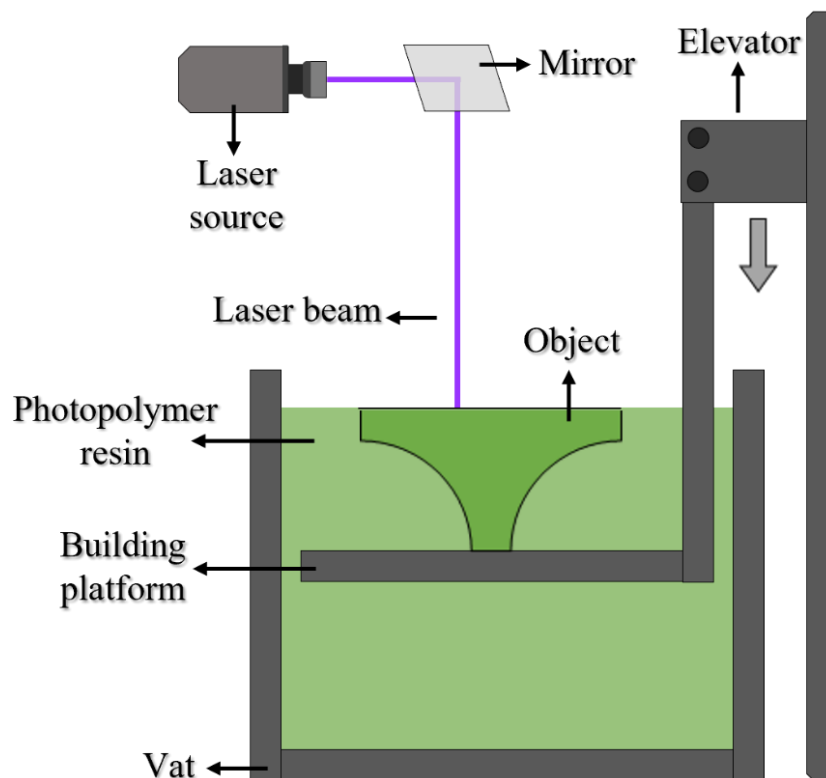


Figure 3: Visual representation of “top-down” vat photopolymerization process.

2.1.3 Powder bed fusion

Powder bed fusion (PBF) is an AM technology that uses energy sources such as lasers, electron beams, or heat lamps to melt (or fuse) powdered materials together in order to create an object.^[33] As demonstrated by **Figure 4**, a thin layer (normally between 0.075 to 0.1 mm thick) of a powdered material is deposited and spread in the building platform by a leveling roller. Then a focused energy source is redirected using a set of mirrors to fuse the powders together. The surrounding powder that was not melted remains loose and acts as support material.^[34] Additionally, they can be recyclable and reused on other 3D-prints. Usually, the printing process takes place under a nitrogen atmosphere to avoid material oxidation, fire and explosions. Finally, for polymeric materials, the powdered material is preheated and is kept warm by heaters around the building platform to reduce the energy required for melting and prevent warping.^[35]

Currently there are four technologies that are defined as a PBF, which are: selective laser sintering (SLS), electron beam melting (EBM), direct metal laser sintering (DMLS) and multi jet fusion (MJF).^[34] Depending of the technology, parts can be fabricated using ceramics, polymers and metals. Furthermore, PBF has shown to be excellent in producing overhangs structures and downward facing surfaces.^[36]

Unfortunately, when compared to other AM technologies, PBF is very slow and demands a lot of energy (to keep the powder warm and melt/fuse it). Additionally, the postprocessing can be costly and time consuming, since the unfused/unmelt material needs to be separated manually, using compressed air or brushing it.^[35,37]

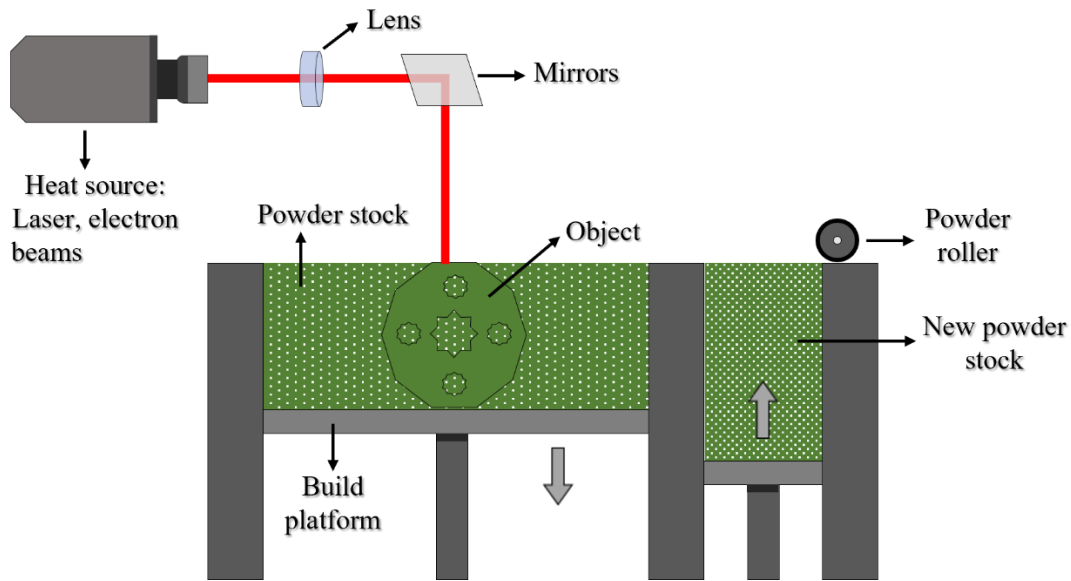


Figure 4: Representation of a power bed fusion machine using a computer aided laser to select melt the particles together on the build platform.

2.1.4 Material jetting

The principle of using droplets to print documents and images from a computer exists since the late 1960s. This technology was commercialized by companies such as Hewlett-Packard, Cannon and Epson, and nowadays inkjet printers are affordable, and present in many households and offices.^[38]

Material jetting (MJ) is a technique similar to inkjet printers, but instead of using inks, it uses droplets of wax and polymers to create a 3D-object. The first generation of material jetting 3D printers started to appear in the late 1990s, where waxy thermoplastics were used as building materials and their commercial application was limited to producing concept models.^[38] Today, MJ technology is able to 3D-print high resolution objects using different types of materials, such as polymers, metals, and ceramics.^[39]

The printing process of a MJ machine is demonstrated in **Figure 5**. In a building platform, droplets of a liquid materials are deposited by a nozzle and are cured using heat or an UV light. After the material is cured, the building platform decreases, allowing another layer to be printed.

This process repeats until the object is finished.^[40] It is also possible to print using different materials and colors, since the machine can have multiple nozzles. Moreover, the extra nozzles can also be used to deposit support materials, that can be later removed by pressurized water or chemically.^[40]

The main drawbacks of material jetting are the lack of feedstock variety, more precisely the UV-activated photopolymers, which are costly and have shown inferior mechanical properties.^[41]

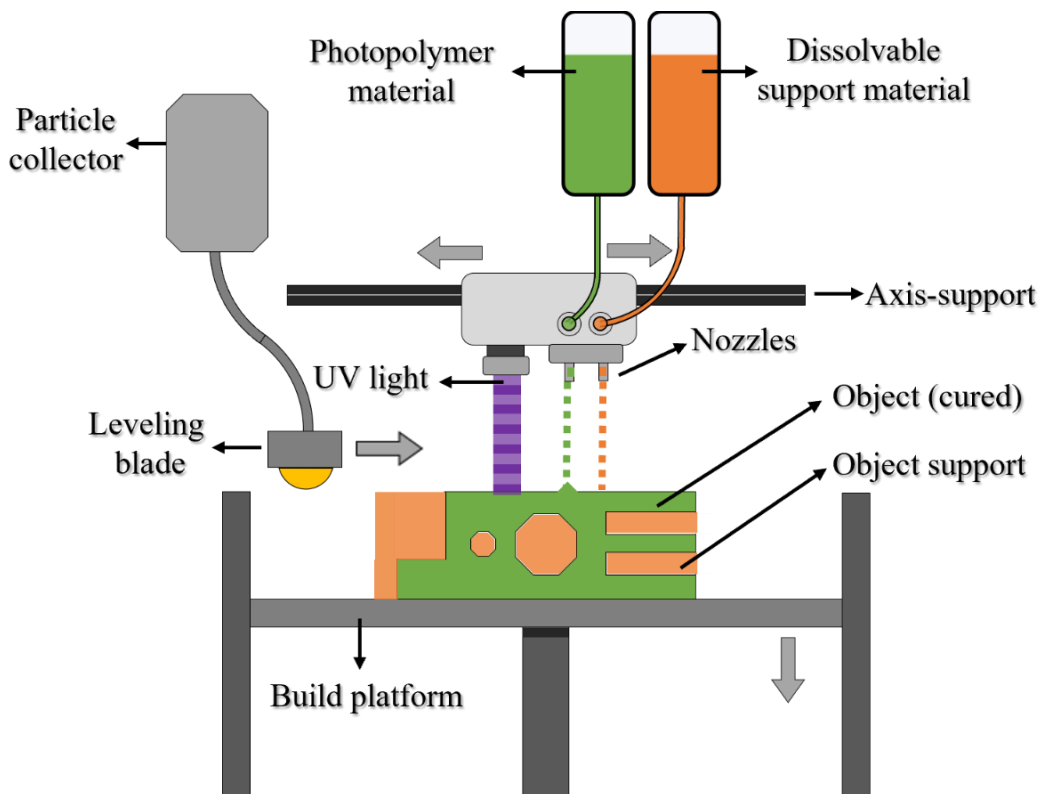


Figure 5: Material jetting 3D-printer using droplets of liquids (photopolymer and support material) and an UV light lamp to fabricate a 3D object.

2.1.5 Binder jetting

Originally known as “Three dimensional printing (3DP)”, binder jetting (BJ) is a process in which a binder material is jetted or sprayed over powdered materials to bond them into an

object.^[42] A description of the process is shown in **Figure 6**. At the beginning of the printing process, a roller containing the powdered material will deposit a thin layer of it on the building platform surface. Then, multiples nozzles (similar to an inkjet printer) will deposit droplets of the binder agent on the powder surface. The platform will then lower, and the roller will pass again, deposition another layer of powder. This process will repeat until the object is finished printing.^[42]

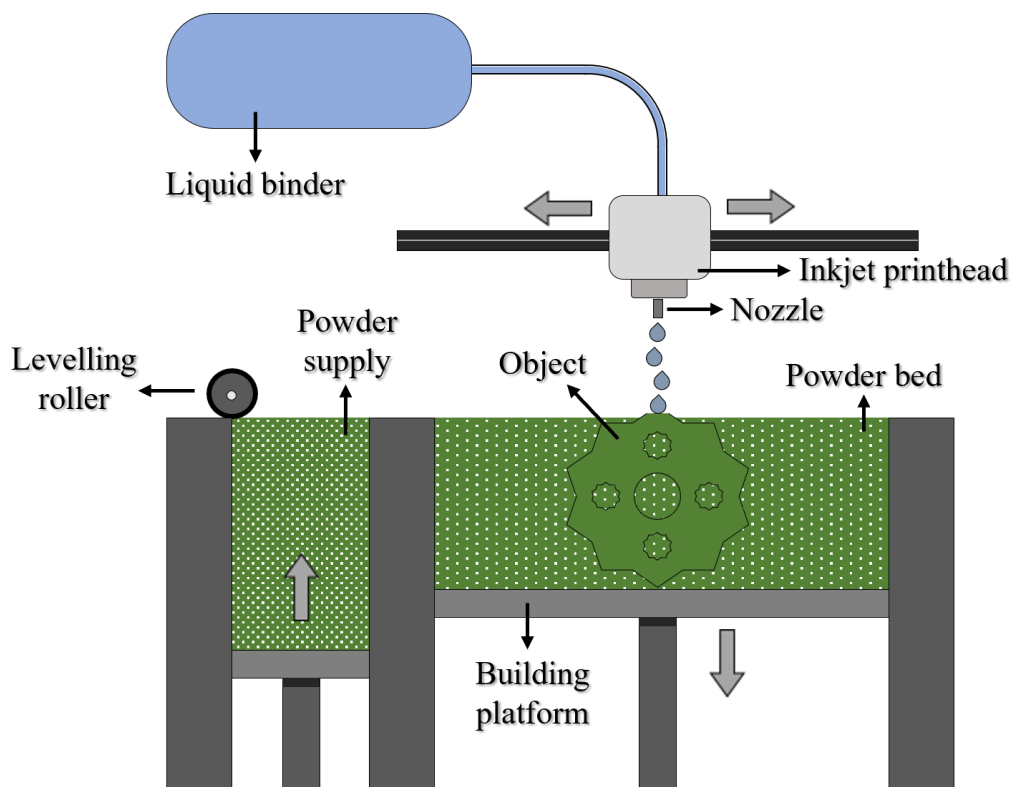


Figure 6: Description of a binder jetting 3D process. Droplets of a liquid binder is used to glue the particles together forming an object.

After the printing is over, the object needs to remain under the powder for some time for the binder agent to completely cure. Only after the green part gained some strength that the post-processing can begin. Usually, it involves removing the unbound powder via pressured air and applying infiltrants to make the object stronger.^[43]

BJ can process materials such as polymers, metals, and ceramics, where similarly to others powder-based technologies, the unbound powder acts as a support during the printing process.^[44,45] Additionally, BJ can print in multiple colors objects, it has a low feedstock cost and

has a fast-printing time. The main disadvantage of this technology is that the parts fabricated have poorer accuracy, mechanical properties and surface finishing.^[43]

2.1.6 Direct energy deposition

Direct energy deposition (DED), also known as laser cladding, is a category of AM techniques that melts a material powder (or wire) as it is being deposited.^[46] Even though DED can process polymers, ceramics, or metal composites, it is mainly used with a metallic feedstock.^[47] A typical DED system is described in **Figure 7**. The printer's head is composed of laser optics, nozzles, an inert gas tubing and, in some cases, sensors. Its 3D printing process is like material extrusion, but instead of the feedstock being melted inside the heater chamber, its process occurs outside, as it is being deposited.^[48]

Compared to others AM technologies, the fused material can be deposited on an empty building platform (to build a new object) or on existent parts (to modify or repair it). Moreover, since the head is mounted in a multi-axis arm (4-5 axis), DED has the ability to print complex objects in multiple directions without requiring support structures.^[49]

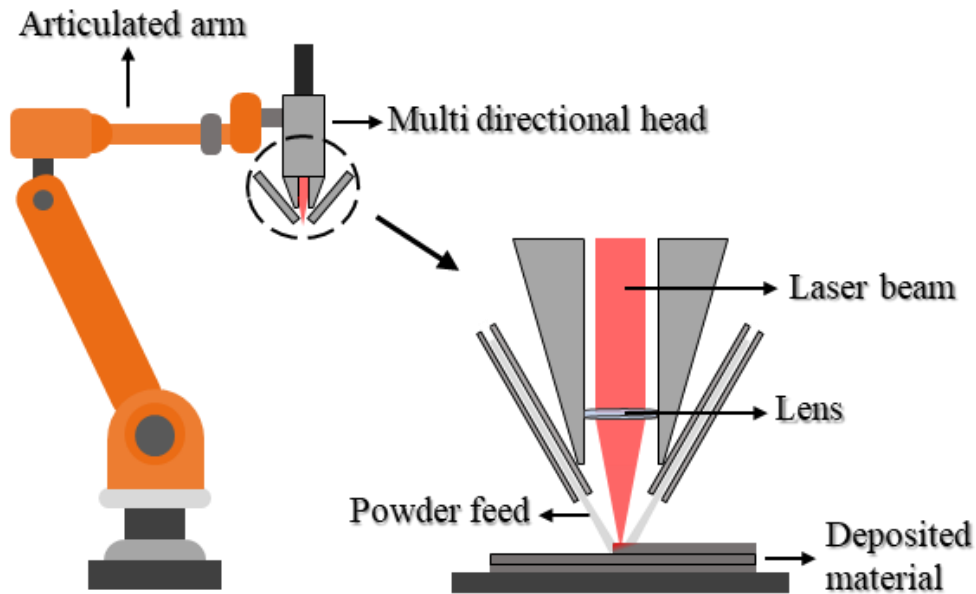


Figure 7: Direct energy deposition using an articulated robotic arm and a powerful laser beam to melt powder or thin filaments of metal on a surface.

The main limitations of DED are its resolution, printing speed and poor surface finishing. Typically, a DED printer has a deposition rate of 25-40 g/h, whereas a vat polymerization machine can achieve rates of 70-130 g/h. It is possible to improve its speed by reducing its resolution and surface finishing. On the other hand, by decreasing its speed and laser power can improve its resolution.^[50]

2.1.7 Sheet lamination

Sheet lamination or laminated object manufacture (LOM) is an AM technology that does not use liquid, powders, or filaments to 3D-print. Instead, as the name suggests, it uses a thin sheet of materials that are glued, ultrasonicated or laminated together to form an object.^[51] As shown in **Figure 8**, the process begins by placing a material sheet on top of a building platform. Then, a laser cuts it accordingly with the layer format. Next, the building platform goes down and another sheet is placed on top of the previous layer. After the sheets are on top of each other, a roller

passes, compressing them together. The process of sheet placement, compression and laser cutting repeats until the object is completed.^[52]

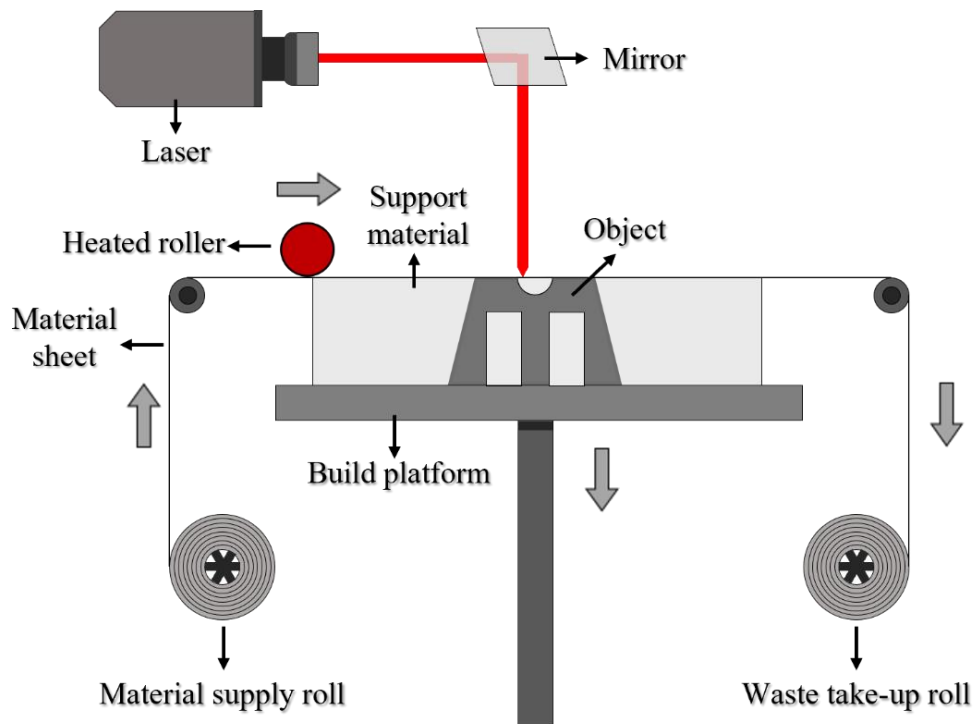


Figure 8: Description of the sheet lamination technique.

This technology can process materials such as paper, PVC polymers, and metals, where depending on the type, a different bonding procedure is used. For paper, an adhesive or glue is used. In the case of PVC sheets, a thermopolymer is melted and added between each layer. Lastly, metals can be bound together by using lasers or ultrasonic waves. Additionally, the metallic parts fabricated by ultrasonic waves suffer lower thermal stress than by other AM methods.^[53]

Normally, sheet lamination is used to fabricate low-cost, full color, and simple design parts. Moreover, it's possible to print hollow parts without the need for support materials. Unfortunately, the high equipment cost and limited geometry reduce its applicability.^[53]

Table 1: Advantages and disadvantages of the seven AM technologies.

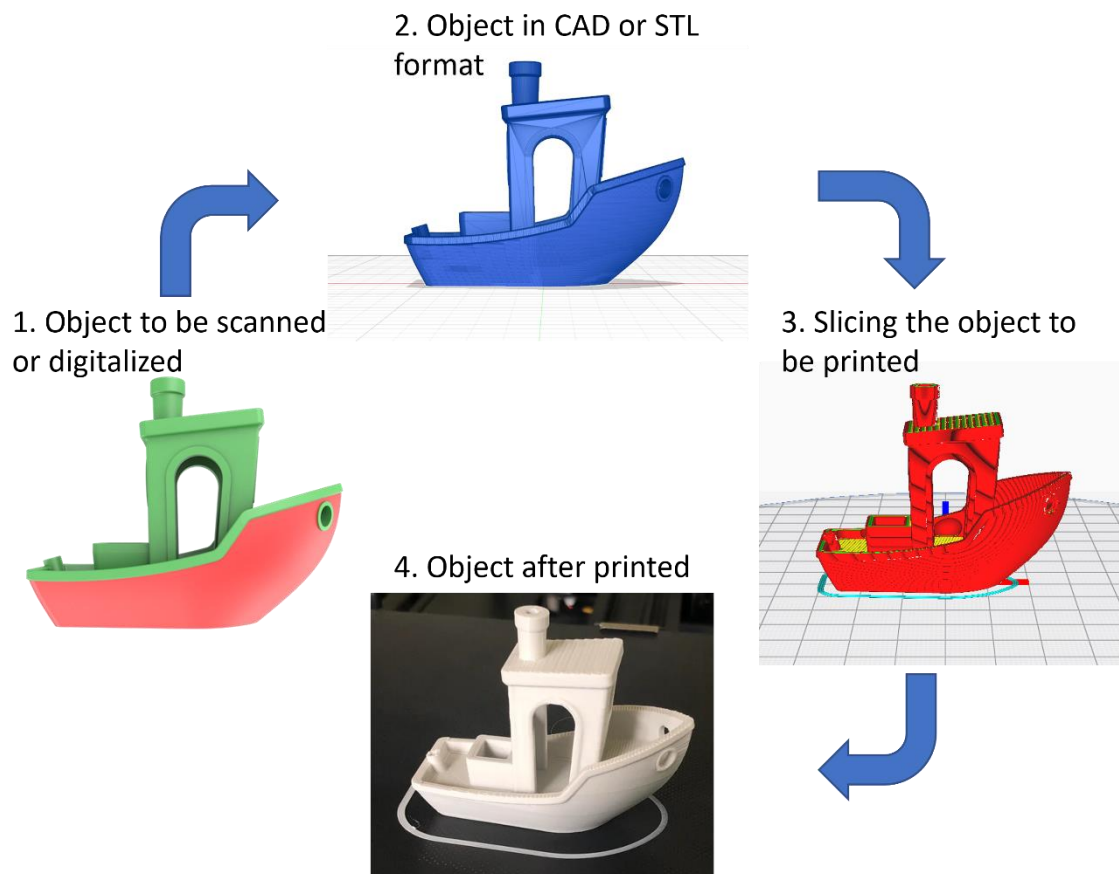
AM method	Resolution (μm)	Materials	Advantages	Disadvantages
-----------	---------------------------------	-----------	------------	---------------

Material extrusion	50 - 150	Thermoplastic polymers, metals, ceramics	Compact, inexpensive, good resolution	Anisotropy, limited mechanical properties
Vat polymerization	5 - 100	Photopolymers	High resolution, isotropic properties	Limited mechanical properties, anisotropy, limited feedstock
Powder bed fusion	50 - 100	Thermoplastics polymer, metals	High mechanical properties, low anisotropy	Thermal stress, rough surfaces, limited reusability, high temperature
Material jetting	25 - 100	Photopolymers	Multicolor printing, fast, multi-material printing	Limited feedstock, low mechanical properties
Binder jetting	50 - 100	Thermoplastic polymers, metals, ceramics, starch	Fast, inexpensive	Limited mechanical properties, rough surface
Direct energy deposition	200 - 300	Metals, metals composites, polymers	Allows print in multiple directions	High temperatures, thermal stress
Sheet lamination	200 - 300	PVC, paper, metals	Low cost, low thermal stress	Limited geometrical freedom

2.1.8 3D-printing process

Although there are different types of 3D-printers, each with specific software's and interfaces, the process of designing a part is similar to all, as shown by the **Scheme 2**. First, the user design or scan the model in a Computer-Aided Design (CAD) software, such as, AutoCAD, Solidworks, FreeCAD, Fusion 360, and save it as an STL format (standard tessellation language) file. The SLT file contains the model surface information in the form of triangulated sections. The user has to consider that the position of the object in the printer could affect its mechanical

properties, the printing time and the quantity of support material needed.^[54,55] Second, the STL file is sliced into vertical layers and converted to geometric code (G-code), containing a series of 2-dimensional horizontal cross-sections commands. Usually, the slicing software is provided by the printer manufacturers, but there are free software's available online, like Ultimaker Cura, that can be configured for different machines. Moreover, it is during this step that the support materials are added to the part and some printing configuration (type of material, process temperature, infill density, printing speed, etc) are defined. Finally, the file is transferred to the printer by LAN or using a USB stick or SD card.



Scheme 2: Simplified process of fabricating a part using a 3D-printer: (1-2) designing or scanning the object, (3) converting it to a series of coordinates and (4) printing it.

After the object has finished printing, it often needs some type of post-processing to remove any support structure, remained unprocessed material and/or perform an additional curing step.^[39]

Usually, the removal of the support materials is done mechanically by hand (using pliers), but there are occasions that it is possible to chemically dissolve it (for microfluid channels). Furthermore, after the support structure is removed, the part may undergo sanding, grinding, cleaning, washing, and other, to remove any uncured or unprocessed material.^[56]

2.2 VAT POLYMERIZATION

As discussed in the previous section, VP is one of the earliest AM technologies,^[11] and their machines uses a combination of photosensitive polymers resins and a light source to print high detailed parts with resolutions down to 5 microns.^[57] Currently, VP accounts for nearly half of the AM market,^[5] and it is proving to be an economical method to produce highly accurate parts having good thermal, mechanical and chemical properties.^[58]

2.2.1 Types of vat polymerization technologies

The two major limiting factors of early vat polymerization machines were: oxygen inhibition and large bulk size. The first problem was due to the first resins composition, that was a combination of acrylic resins and a photoinitiator. Under ultraviolet light, the photoinitiator is activated, creating two molecules, each containing an active radical group. These activated radical groups will then react with the acrylate groups, starting the polymerization reaction. However, in the presence of oxygen, these radical groups are blocked, generating dead-chain ends.^[59] The second problem was the vat size. Even to print a small object, large amounts of photosensitive resins were needed, which increased the cost.

In trying to address both problems a new vat polymerization process, known as “bottom-up”, was developed (**Figure 9**). In this process, instead of the light being emitted from the top of the printer (interacting with the resin surface), it is emitted from the bottom of the machine. Then,

the light goes to a set of mirrors (that moves in the X and Y directions) and it is redirected through a transparent tray, made of polydimethylsiloxane (PDMS) or a metallic structure with a sheet of fluorinated ethylene propylene (FEP) on the bottom. The photopolymerized layer is formed on the surface of the vat, which has the photosensitive liquid on it. By using this technique, oxygen inhibition is minimized, and smaller vats (and smaller printer) can be used. Furthermore, while the light is passing through the vat, a build base is being pressured into it. Using the adhesive force of the polymer, the building base peels the solidified layer from the vat and sticks it into itself. After that, the building base starts to slowly move upwards, allowing other layers to be printed.^[60] The downside of the “bottom-up process” is that the force necessary to peel the layers from the vat to the building base can provoke failures and distortions.^[61,62]

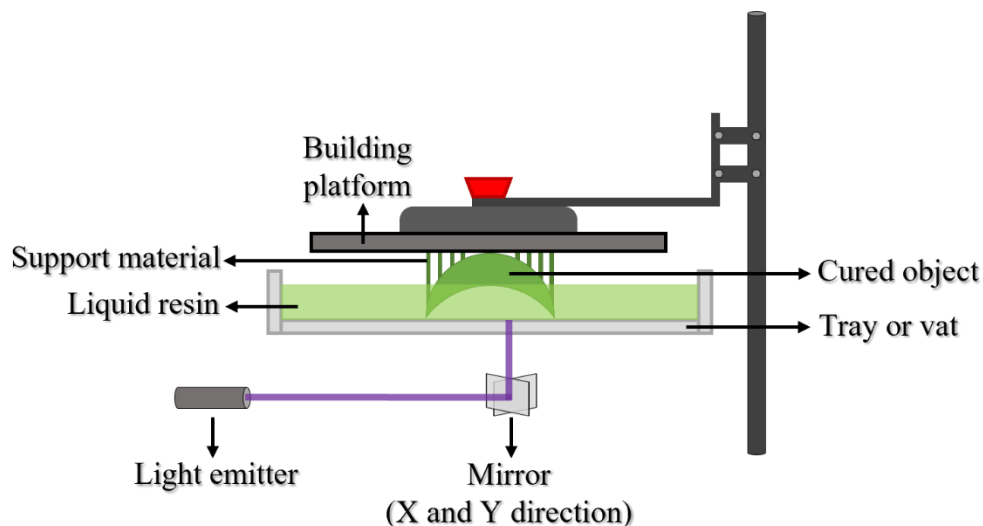


Figure 9: Schematics of a “bottom-up” stereolithography printer.

The “bottom-up” machines that use a laser and a set of mirrors are commonly known as stereolithography apparatus (SLA). These machines were the first generation using the “bottom-up” technique and were responsible for making vat polymerization affordable and popular. However, since the machines have only a set of mirrors to redirect the light, they have longer printing times.^[63]

To overcome the SLA slow printing speed, modifications were made to its design. digital light processing (DLP) is an illumination technique that was able to decrease the SLA printing time. This technique uses programmable light source, able to regulate the light passage through the vat according to the layer characteristics (**Figure 10**).^[64] In order to do so it controls an array of millions of tiny microscopes that hinge on each other, known as DMD (digital micromirror device), that can selectively block and/or redirect the light to the resin.^[63] Another advantage of a DLP printer is its precision, being capable of printing objects with 50 μm . However, it also has its drawbacks. The resolution of the object is limited by the size and numbers of DMDs in the display. Moreover, DMDs are expensive to manufacture and needs to be replaced after a certain number of prints.^[65]

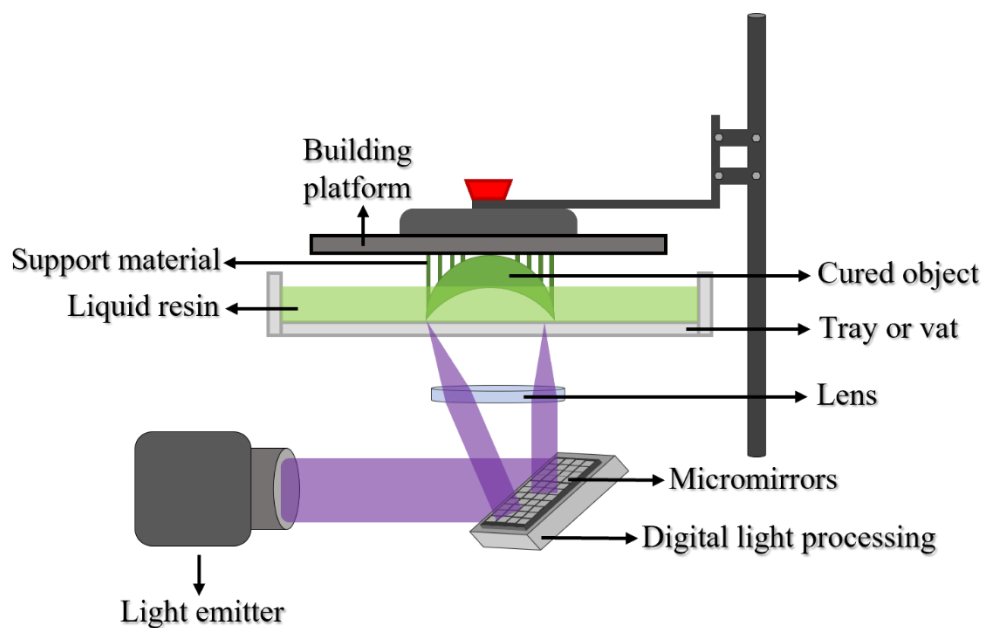


Figure 10: Description of the mechanisms behind a digital light processing 3D printer.

Recently, a new technology has emerged to address the size and cost limitation of DMDs, known as DLP-LCD (**Figure 11**). In these machines, instead of using DMDs the imaging system is a liquid crystal display (LCD). By applying an electric field to the LCD, it will change its molecular arrangement and block the light from passing through it.^[66] The printer resolution is

related to the screen pixel size and number, whereas recent machines were able to reach 8k resolutions.^[66] The main advantage of using LCD screens is that they are very cheap to manufacture. However, due to their short lifespan they need to be constantly replaced.

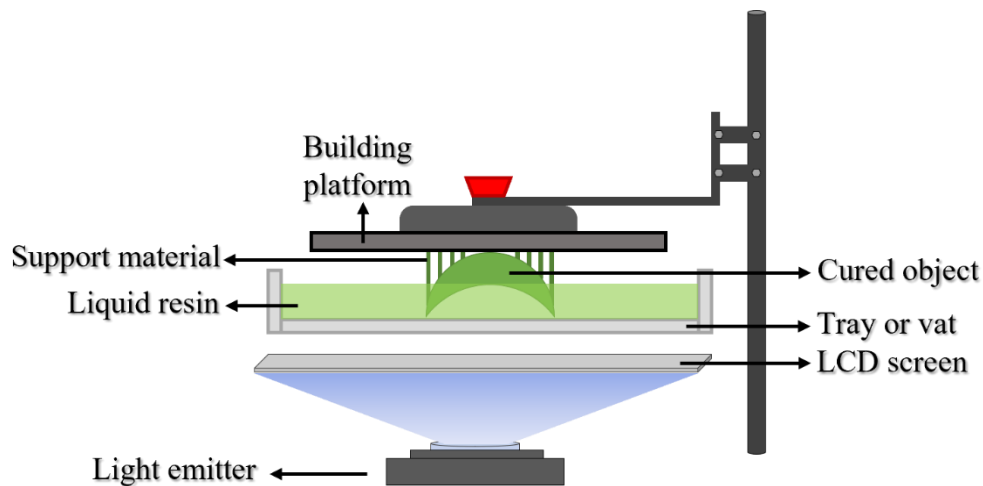


Figure 11: Visual representation of the interior of an LCD-DLP.

Another type of vat polymerization technique that was based on DLP and gained a lot of attention was Continuous Liquid Interface Production (CLIP), shown in **Figure 12**. CLIP machines use the same illumination technique as DLP machines. However, different from other vat polymerization techniques that want to reduce or remove oxygen inhibition from its printing process, CLIP do the opposite. Instead of using PDMS or FEP vat (that blocks oxygen from interacting with the resin), it uses an oxygen permeable membrane to create a “dead zone between the resin and building platform”, where the polymerization is inhibited.^[67] During the printing process, the building platform goes close to the “dead zone” but keeps a small distance from it, where a thin layer of resin can be polymerized. The light from the projector passes through the membrane and the dead zone, curing this thin layer into the platform base, while oxygen on the “dead zone” inhibits further polymerization. Moreover, by matching the thickness of the “dead zone” and the resin curing rate, it is possible to continuously rise the platform as the resin is being cured.^[10,67]

The advantage of CLIP is that it can print 25 to 100 times faster than traditional DLP, where the theoretical potential could go up to 1000 times.^[66] However, the downside is that the permeable membrane is expensive, the objects must be hollowed out, cannot have large flat horizontal surfaces, and the resins must have low viscosity and no (or low) fillers.^[68]

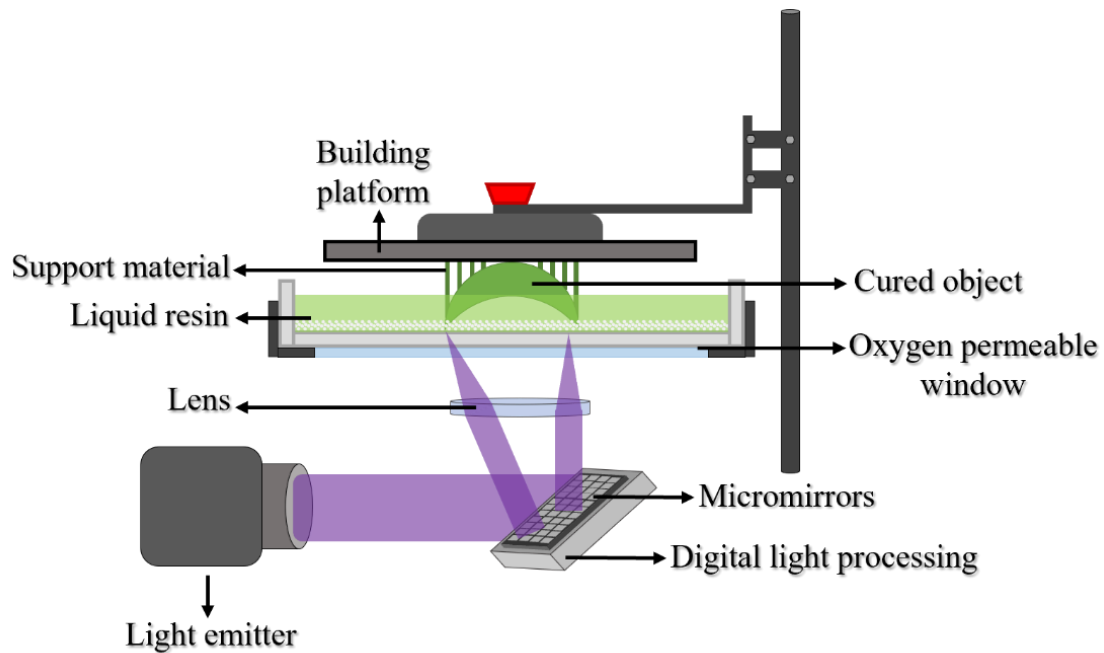


Figure 12: Using an oxygen-permeable membrane CLIP machines can control the photopolymerization reaction.

So far, the techniques based on vat polymerization were aimed at improving the printing speed. Two-photon polymerization (2PP or TPP) went on a different path, where its objective was to improve the printing resolution. Indeed, TPP has the highest resolution of all AM technologies, being capable of printing structures down to 50 nm.^[69] As demonstrated by **Figure 13**, its printing process diverges from other VP techniques, where the object is printed in the middle of the resin without needing a building platform or support structures. TPP accomplish that by applying the principle that an UV sensitive material can be polymerized by infrared light if its wavelength is approximately double ($\lambda_{IR}=2\lambda_{UV}$).^[70]

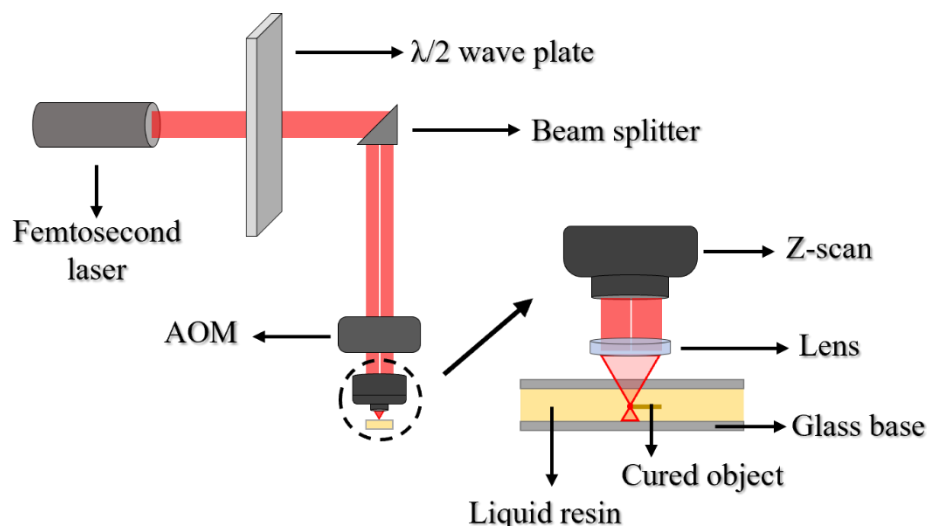


Figure 13: Schematic description of a 2PP process. By using a near-infrared laser (700 – 800 nm), the light can pass through the surface of the photosensitive material and will only react at the point where the two photons intersect.

According to Bass, M. 1994,^[71] the TPP absorption coefficient for two photons can be defined as (**Equation 1**):

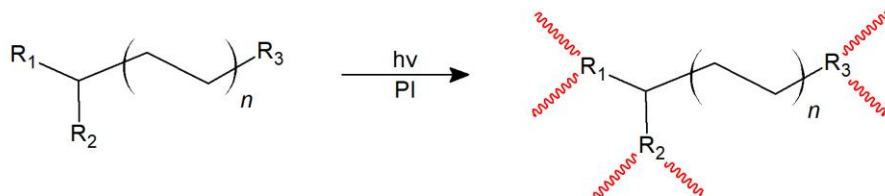
$$\alpha_2 = \frac{2\hbar\omega}{I^2} \nu_{2PA} = \frac{N}{E} \sigma_{2PA} \quad (\text{Eq. 1})$$

Where ω is the laser frequency, \hbar is the Dirac constant, I is the irradiance or power (radiation flux) per focused volume, ν is the rate transition of 2PA to the voxel, E is the photon energy, N is the density of the photoresist (number of reaction molecules in the voxel), σ is the cross-section of the 2PA ($\text{cm}^4 \text{ s} / \text{photon}$).

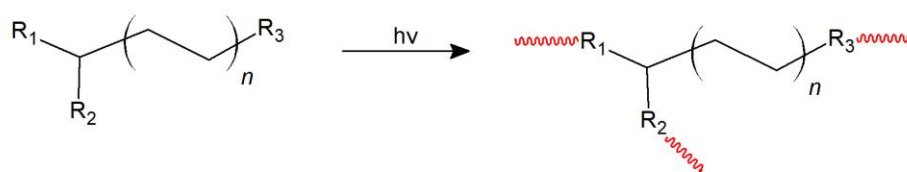
2.2.2 Photopolymer chemistry

A photopolymer is any substance that have its physical or chemical properties altered when exposed directly or indirectly to light. Encompassed with this definition, as shown in **Figure 14**, there are five reaction types that a photopolymer can undergo.

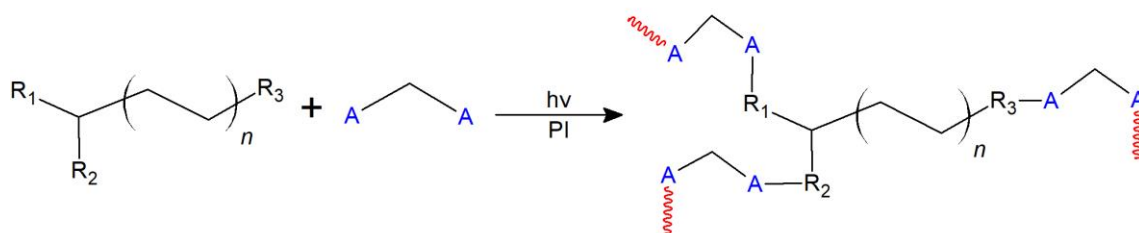
1. Photopolymers that undergo photoinitiated chain growth



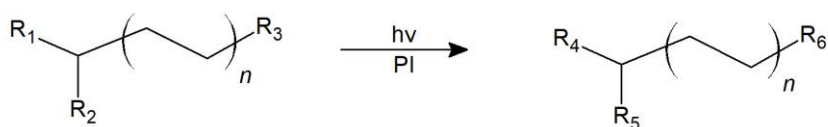
2. Photopolymers that undergo step-growth polymerization



3. Functional polymers that undergo photoinduced crosslinking



4. Polymers that undergo functional group modification under irradiation



5. Polymers that undergo photoinduced cleavage reactions

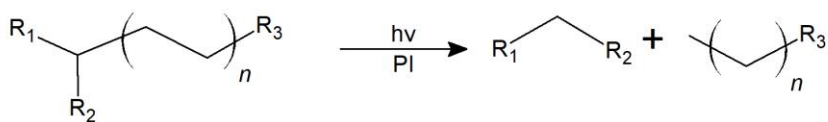
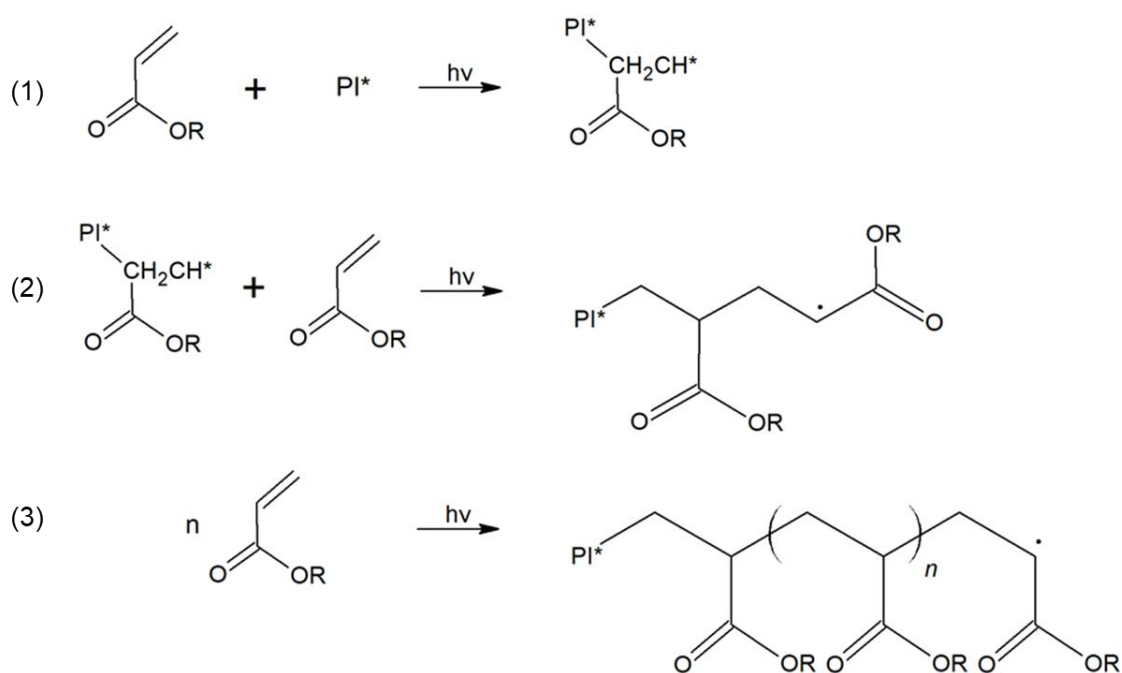


Figure 14: The five types of photopolymerization reaction.

The first type of photopolymers (type 1) are low molecular weight monomers, dimers and/or oligomers that, in combination with a photoinitiator can have their functional groups undergo radical, cationic, or anionic chain polymerization. Type 2 polymers are photoactive substances that are formed by step-growth polymerization, coupling or dimerization. These

substances are mostly used in negative tone photoresist technologies. The next one, type 3, are systems consisting of at least two photopolymers, each having reactive functional groups. Upon exposition to light, these groups start to react, and a cross-linked structure is formed. Type 4 are substances that have their functional groups modified in the presence of a photoactive compound whose photolysis generates a catalytically active species. Lastly, the type 5, are photopolymers that have their chain cleavage when irradiated with light. Usually to perform the reaction, a photoinitiator, an acid, base or free radical is required.^[72]

Among the five types of photopolymers, only the materials belonging to the type I group are used in vat polymerization. (Meth)acrylate-based resins were the first material widely applied for 3D printing due to their compatibility with most printers and fast reaction speed. The latter is attributed to its photopolymerization mechanism (**Scheme 3**) that follows a free-radical process.^[73]



Scheme 3: Free-radical photopolymerization steps: (1) Initiation, (2) first chain and (3) n-chain propagation.

The most common (meth)acrylate and diacrylates polymers used for 3D printing are: Poly(ethylene glycol) diacrylate (PEGDA),^[74-76] triethylene glycol dimethacrylate

(TEGDMA),^[77-79] bisphenol A-glycidyl methacrylate (Bis-GMA),^[80] isobornyl methacrylate (IBOMA),^[81,82] and methyl methacrylate (MMA)^[83,84]. These materials (**Figure 15**) have been used to fabricate shape memory polymers, siloxane-based hybrid polymer network, medical implants, and functional materials for bio-applications.^[65]

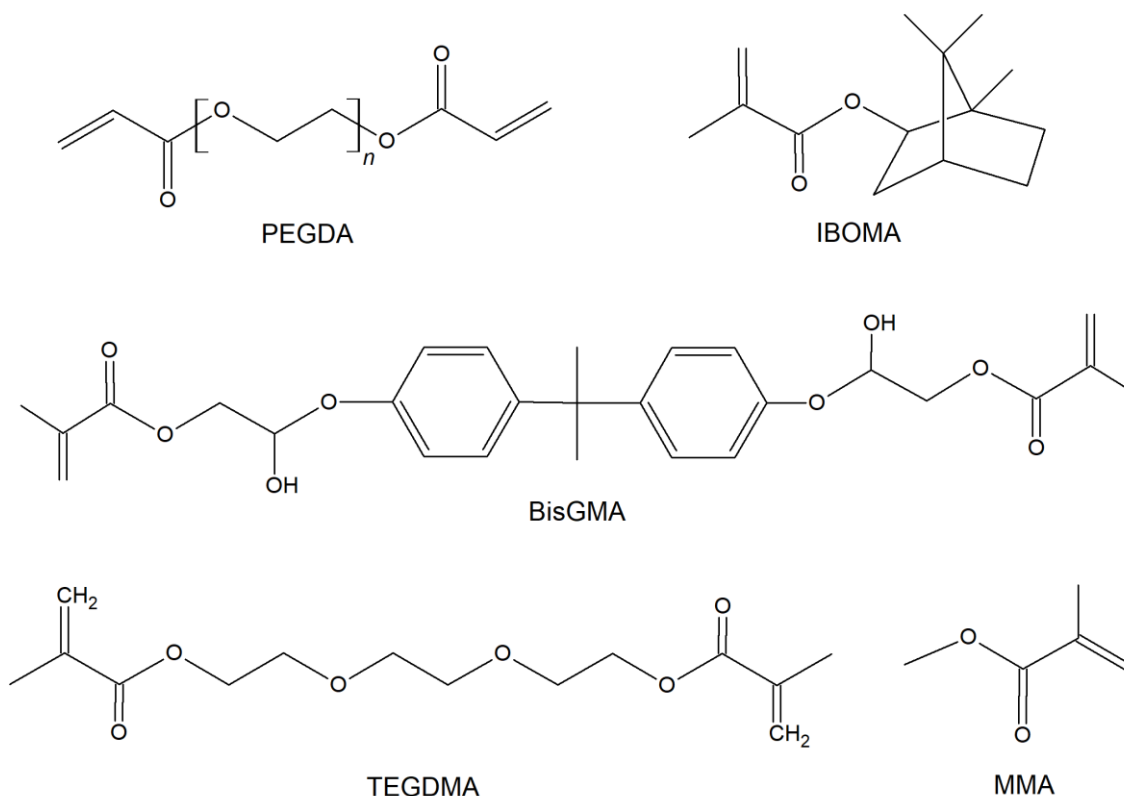
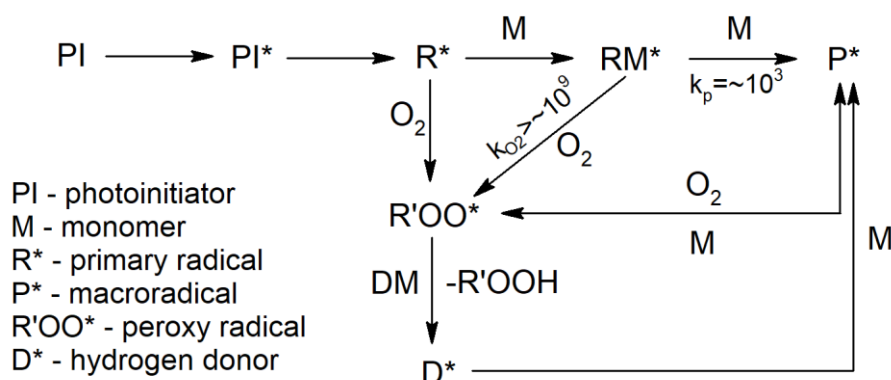


Figure 15: Chemical structure of commonly used acrylates monomers for developing SL resins.

Although (meth)acrylate-based resins are still very popular, some chemical and physical characteristics limit their application. Usually, the parts produced using pure (meth)acrylate-based resins tend to shrink, warp or curl and have shown low elasticity and high brittleness. This happens due to their inhomogeneous and highly cross-linked network structure.^[85] Moreover, under the presence of oxygen, both the initiator and propagation radical groups are subjected to inhibition and have the reaction terminated (**Scheme 4**).



Scheme 4: Effects of oxygen on the photopolymerization reaction.

As shown by **Scheme 4**, the oxygen rate constant (k_{O_2}) is almost 10^6 higher than the propagation rate coefficient (k_p), which results in the reaction being delayed until the oxygen dissolved is consumed in a peroxidation process. The peroxy radicals formed are inefficient as initiators (extremely low-rate constant), but they can still react with the hydrogen from monomers, polymers, or diluents, generating hydroperoxides that reinitiates the radicals (D^\bullet). After the oxygen concentration is reduced to the point in which $k_{O_2} < k_p$, the propagation phase begins. It is during this point that the diffusion of oxygen from the atmosphere becomes the problem.^[86]

To address the limitations of (meth)acrylate-based resins, other materials were tested as additives or substitutes. Thiol-ene and thiol-yne systems (**Figure 16**) were initially viewed as an interesting alternative. First, its photopolymerization reaction proceeds via a radical step-growth or Michael-addition reactions, resulting in a more homogeneous network structure and parts with lower shrinkage.^[87] Second, thiols can be potential hydrogen donors, forming peroxide and thiyl radical groups, which reduces oxygen inhibition. Third, thiol-ene systems are activated directly by UV-light, without the need of photoinitiators.^[88] This is particularly interesting for biomedical application since photoinitiators have often demonstrated to negatively impact its biocompatibility.^[89]

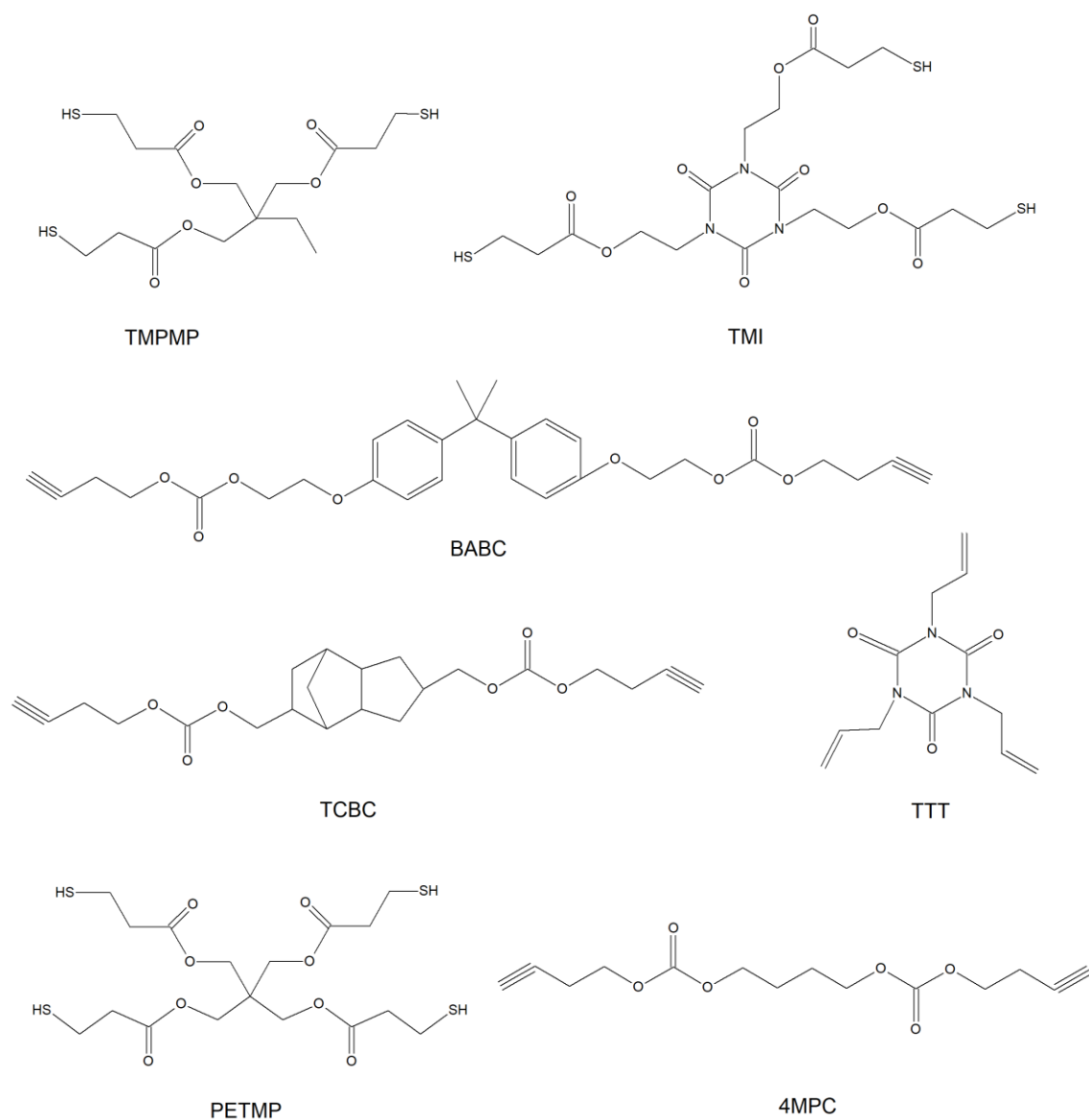


Figure 16: Chemical structure of thiol-ene and thiol-yne monomers for developing SL resins.

However, there are two major issues limiting the large-scale application of thiol-based resins: Its poor shelf life and strong odor.^[72,90] Even though in the past years some authors have proposed solutions to these problems,^[91,92] the general industry is reluctant to invest in thiol-based resins.

Another promising material are epoxy-based resins (**Figure 17**). Different from thiol-based or (meth)acrylic-based resins, epoxy-based resins, are cured using a cationic initiator following a step-growth type of polymerization. The parts produced using this resin have better

mechanical properties, water resistance, superior accuracy and a low shrinkage rate.^[93] Unfortunately, the photopolymerization of pure epoxy resins requires longer exposition to UV light to cure it, which was a problem for 3D printing.

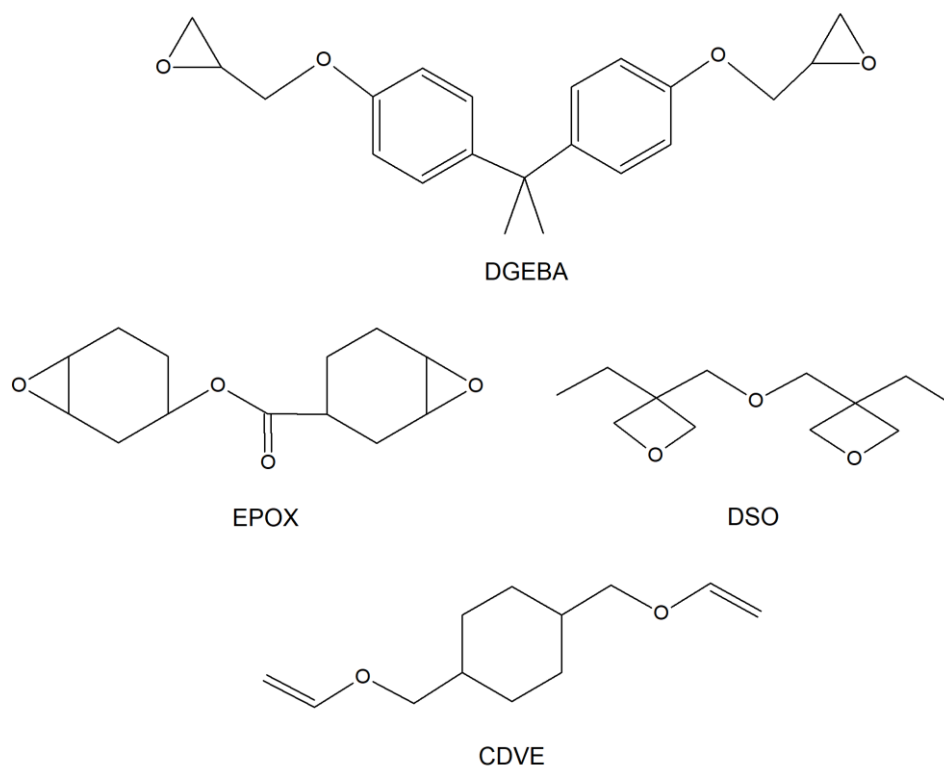
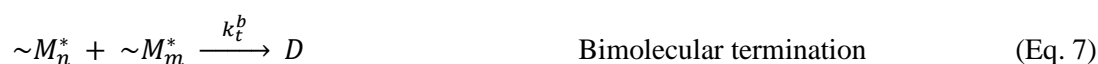
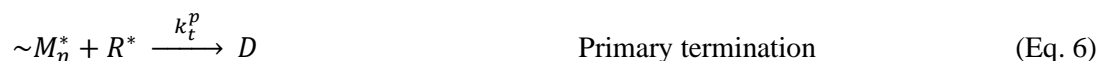


Figure 17: Chemical structure of epoxy monomers for developing SL resins.

Nevertheless, when combined with (meth)acrylate-based resins, it resulted in improvements in both properties of monomers. The acrylate groups enhanced the reaction speed and reduced its the energy requirement. On the other hand, the epoxy monomer acted as a plasticizer, increasing molecular mobility, and decreasing warping or distortion effects. Furthermore, it also reduced the sensitivity of acrylate to oxygen by slowing down the diffusivity to the atmosphere.^[66]

2.2.3 Photopolymerization reaction

The photopolymerization reaction for VP is an exothermic process (releasing heat around 85 kJ/mol) and depends on several factors (printer type, material type, resin composition, and more) that make developing a global model very difficult. However, the principle of most photopolymerization reactions is similar to a typical radical polymerization. As shown by **Equations 2-8**, it involves the initiation, propagation, chain transfer, and termination steps.



Where M, I and RH denotes monomer, initiator, and chain transfer agent molecules, respectively; $\sim M_n^*$ and M_n^* are macroradicals; k_d initiator decomposition rate constant and k_i , k_p , k_{tr} , are respectively the rate coefficients for; initiation, propagation, chain transfer; k_{tp} , k_{tb} , and k_{tm} are the primary, bimolecular, and monomolecular termination rate coefficients, respectively.

In the initiation step, after the photoinitiator is exposed to UV light it decomposes into two radicals (**Equation 2**), which react with the monomer creating growing polymer chain (**Equation 3**). The rate of this reaction (initiation rate) is expressed by **Equation 9**.

$$R_i = 2k_d[I] \quad (\text{Eq. 9})$$

The next step is the growth of the polymer chain, which occurs by adding the monomers molecules to the radical center. It is during this step that side reactions, like chain transfer, can happen. Moreover, these side reactions can result in a decrease in the polymer molecular weight, or its branching.^[86] Finally, the propagation reaction rate is described by **Equation 10**, where [M] and [P^{*}] represents the monomer and total reactive radical concentration, respectively.

$$R_p = k_p[M][P^*] \quad (\text{Eq. 10})$$

The polymer chain growth is stopped by a termination reaction, in which the radicals' centers are terminated or cancelled. In the first case, the polymer chains terminate by themselves in a process called disproportionation which creates dead chains. This can happen by the presence of inhibitors or the consumption of all monomers. In the second case, two active polymer chains combine with each other, forming one larger dead chain. These two processes can be represented by the termination reaction rate (**Equation 11**).

$$R_t^b = 2k_t^b[P^*]^2 \quad (\text{Eq. 11})$$

In some photopolymerization reaction there can be the formation of high branched structures, which can block the radicals' groups from reacting with other molecules. This can be considered as an additional form of termination and its reaction rate is shown by **Equation 12**.

$$R_t^m = k_t^m[P^*] \quad (\text{Eq. 12})$$

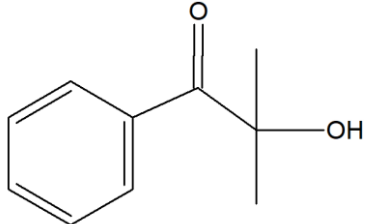
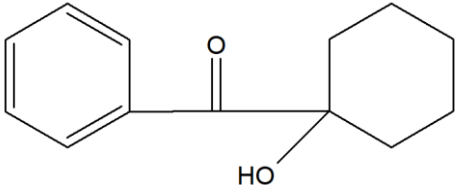
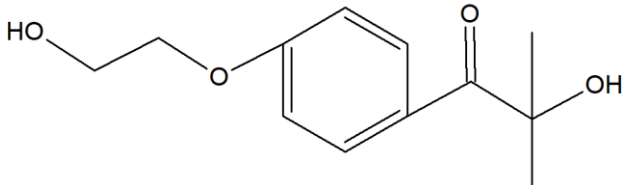
It is also possible to calculate the kinetic chain length (similarly to the average molecular weight) of the final polymer. This is done by dividing the rate of propagation (R_p) by the rate of initiation (R_i), as demonstrated by **Equation 13**.

$$C_l = \frac{R_p}{R_i} \propto \sqrt{\frac{[M]}{[I]}} \quad (\text{Eq. 13})$$

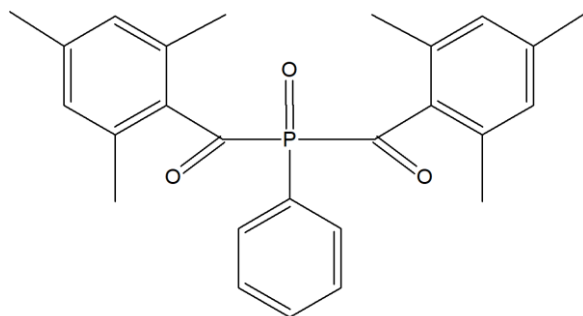
There are two main components controlling the reaction process, the concentration of monomer and photoinitiator. Usually, increasing the latter makes the reaction goes faster, but there is a limit on how much is possible to increase it. In some cases, if the concentration is doubled the polymerization rate will increase only by a factor of 1.4. Moreover, the polymer molecular weight will reduce by the same factor.^[94] Therefore, it is important to find the optimal amount of photoinitiator needed for each resin.

Another important factor is to find the adequate initiator for the photopolymerization reaction, since its efficiency is related to the light source range. **Table 2** shows the most used photoinitiators, their structures and operational range.

Table 2: Name, chemical structure, molecular weight and wavelength of popular photoinitiators.

Name	Chemical structure	Molecular weight	Absorption wavelength (nm)	Ref.
2-Hydroxy-2-methyl-1-phenylpropan-1-one (Darocur 1173)		164.2	245, 280, 331	[95]
1-Hydroxy-cyclohexyl-phenylketone (Irgacure 184)		204.3	244, 280, 330	[96]
1-[4-(2-Hydroxyethoxy)-phenyl]-2-hydroxy-2-methyl-1-propane-1-one (Irgacure 2959)		224.3	274, 365	[97]

Phenylbis(2,4,6-trimethylbenzoyl)phosphine oxide (BAPO)

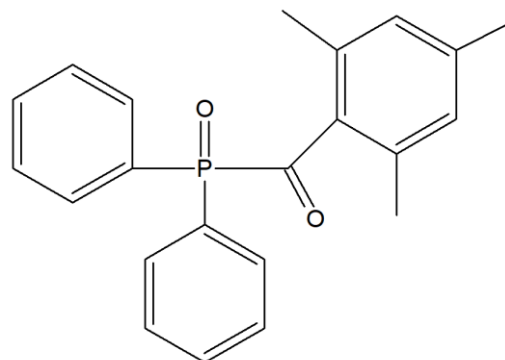


418.5

295 - 380

[98]

Diphenyl(2,4,6-trimethylbenzoyl)phosphine oxide (TPO)

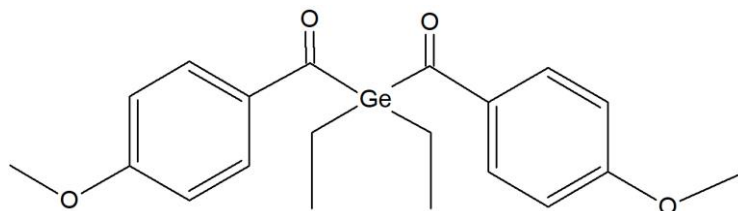


348.4

295, 370 - 395

[99]

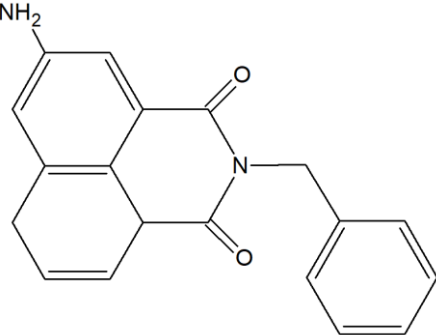
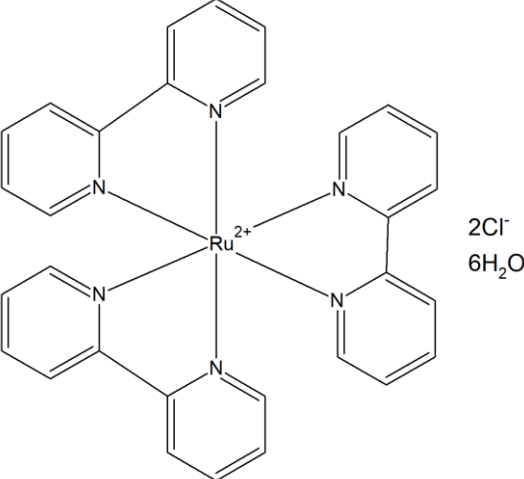
Ivocerin



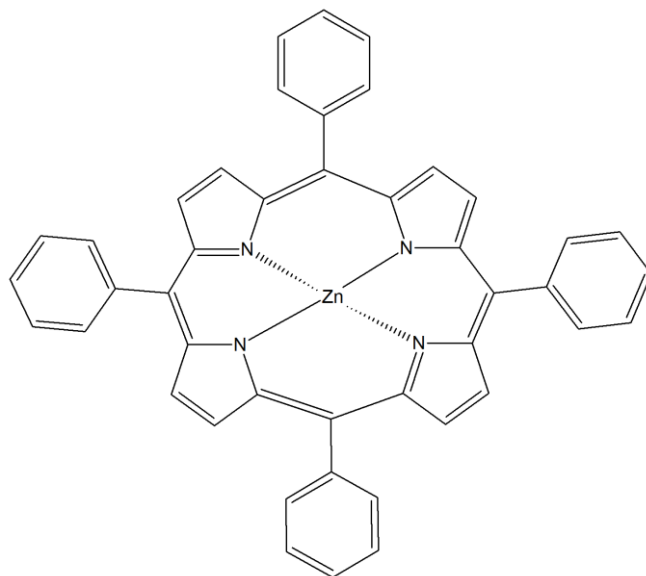
401

408

[82]

Naphthalimide derivative 2 (NDP2)		304.3	417	[100]
Tris(2,2- bipyridyl)dichlororuthenium(II) hexahydrate (Ru)		569.6	453	[101]

Zinc tetraphenylporphyrin
(ZnTPP)



678.1

477, 530

[102]

2.2.4 Irradiance and exposure influence on photopolymers properties

Apart from its chemical formulation (materials, photoinitiator, diluents, and others), the curing characteristics of a photosensitive resin depend on two factors: light properties and scanning speed. The first concern are parameters related to the laser power, dimension, and size, while the latter factor at the velocity at which the process is carried out. The combination of these two factors is known as irradiance. Moreover, by assuming that the absorption of radiation by the resin follows the Beer-Lambert Law, it is possible to calculate the amount of light per unit area absorbed using **Equation 14**.

$$H_{(x,y,z)} = H_{(x,y,0)} e^{-z/D_p} \quad (\text{Eq. 14})$$

Where D_p is the resin penetration of depth (mm). By setting D_p equal to z ($e^{-1} = 0.3678$), it is possible to observe that the irradiation at a depth D_p is about 37% of the irradiance at the resin surface.

The maximum irradiance (H_0) will occur at the center of the laser beam, where $x=0$, and it can be calculated by integrating the irradiance function over the area covered by the beam at any point in time (**Equations 15 to 16**).

$$P_L = \int_{r=0}^{r=\infty} H(r, 0) dA \quad (\text{Eq. 15})$$

$$H_0 = \frac{2P_L}{\pi W_0^2} \quad (\text{Eq. 16})$$

Where P_L is the laser power and W_0 is the $1/e^2$ Gaussian half-width of the beam spot. Furthermore, it is possible to calculate the irradiation at any point of the vat (x,y) by modifying **Equation 17**, as described below:

$$H(x, y) = \frac{2P_L}{\pi W_0^2} e^{-2x^2/W_0^2} e^{-2y^2/W_0^2} \quad (\text{Eq. 17})$$

Assuming a constant laser scan velocity and integrating **Equation 17** over the distance between two points (from x to b), it is possible to determine the minimum energy needed for the resin to start to cure, known as critical exposure (E_c):

$$E(y, 0) = \frac{2P_L}{\pi V_s W_0^2} e^{-2y^2/W_0^2} \int_{x=0}^{x=b} e^{-2x^2/W_0^2} dx \quad (\text{Eq. 18})$$

$$E(y, 0) = \sqrt{\frac{2P_L}{\pi W_0 V_s}} e^{-2y^2/W_0^2} e^{-z/D_p} \quad (\text{Eq. 18.1})$$

Where V_s is the scan speed of laser (mm/s). Finally, by combining **Equations 14 and 18.1**, a fundamental general exposure equation is formulated:

$$E(x, y, z) = \sqrt{\frac{2P_L}{\pi W_0 V_s}} e^{-2y^2/W_0^2} e^{-z/D_p} \quad (\text{Eq. 19})$$

2.3 BIO-BASED, (BIO)DEGRADABLE AND BIOCOMPATIBLE MATERIALS FOR VAT PHOTOPOLYMERIZATION

In the previous chapter it was discussed how most of the photosensitive resins used for vat polymerization belong to the type 1 photopolymer and are made of acrylate and epoxy monomers with a photoinitiator. Originally, the majority of these monomers were derived from petroleum. However, environmental concerns regarding the usage of fossil-derived materials and their inherited toxicity align with plastic pollution, calling for more research on the development of bio-based, biocompatible, and (bio)degradable resins.

2.3.1 Bio-based materials

Instead of using petroleum as raw material, bio-based polymers are fabricated using biomass. This biomass can be extracted from various sources, where the most common are plant and vegetable oils.^[103] Vegetable oils are a relatively cheap, renewable, reliable and worldwide available resource that has been used for centuries for food application but has become an attractive raw material for the plastics industry.^[104] They can have their chemical structure modified to create a variety of components, such as monomers, oligomers, thermoplastics, thermosetting resins and bio composites.^[105,106]

As shown by **Figures 18 and 19**, vegetable oils can have their structures modified by process of (meth)acrylation or epoxidation. In the first process, vegetable oils are reacted with (meth)acrylate acid and a catalyst to graft acrylate groups on their structure (**Figure 18**). Zhang et al. (2013) tested the efficacy of a one-step acrylation reaction using soybean oil and boron trifluoride etherate as a catalyst. Their objective was to evaluate the effects of reaction stoichiometry and time on the conversion. The results showed that the optimal reaction time was 6h, where conversion and yield reached 75.7% and 71.6%, respectively.^[107] Su Yupei, et al. (2020) performed acrylation reactions on several types of vegetables oils. The acrylation grafting rate varied according to the double bonds available in the vegetable oil structure. Moreover, continuing the reaction would decrease the acrylation rate. Nevertheless, all vegetable oils were successfully acrylated and displayed photopolymerization capabilities.^[108]

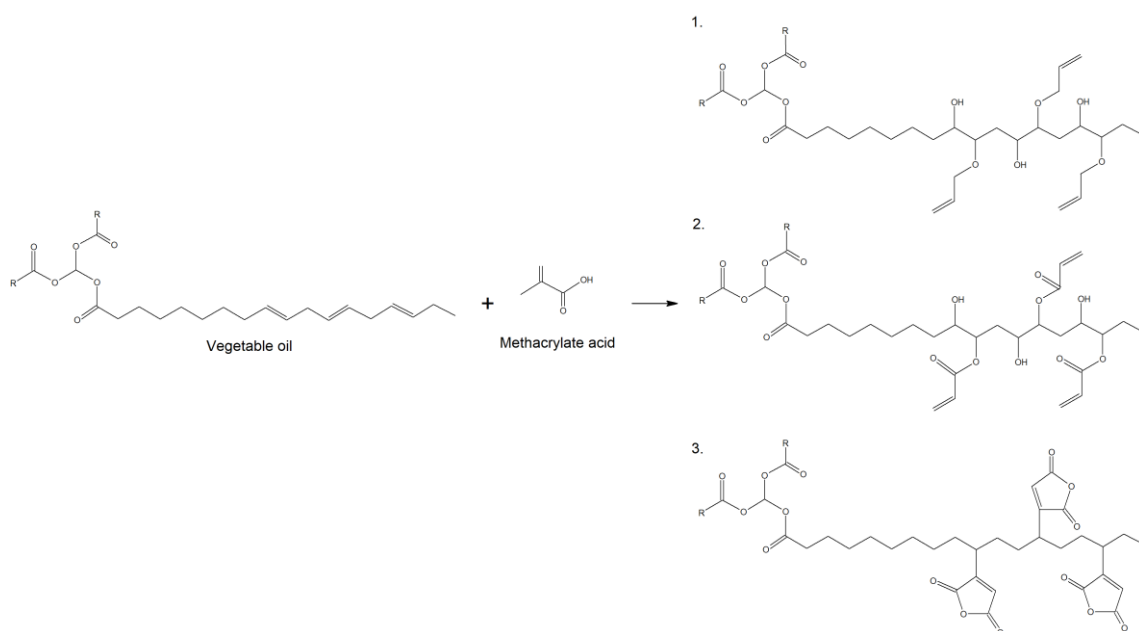


Figure 18: (Meth)acrylate modification of vegetable oil.

The second process, epoxidation, is normally carried out by reacting vegetable oils with peroxy acids (**Figure 19**). Saithai et al. (2020) investigated the effects of two epoxidation methods (peroxy acids and chemo-enzymatic) on soybean oil. Although both methods showed a similar degree of epoxidation, the enzymatic reaction produced a higher acid content, which was attributed to the presence of epoxidized free fatty acids.^[109] To create suitable resins for 3D-printing, Branciforti et al. (2019) modified soybean, corn, sunflower, linseed and tung oil using formic acid, hydrogen peroxide and sulfuric acid. Their results showed that the vegetable oils were able to achieve an internal epoxidation degree superior to 86% with the exception of tung oil, with only 33%. However, the reaction yield was low, with a maximum degree of 34%. Furthermore, compared to acrylated vegetable oils the resins required longer exposition times, but were successful in printing objects.^[110] Finally, **Table 3** presents some of the different types of vegetable resins used for vat photopolymerization.

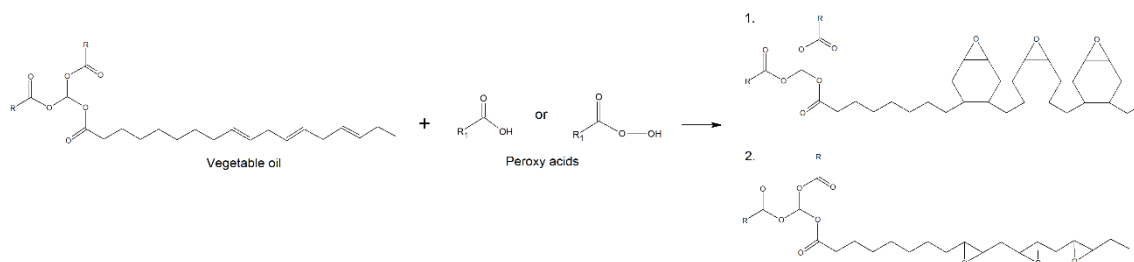


Figure 19: Epoxy modification of vegetable oil.

However, the problem of using vegetable oils to fabricate bio-based resins for vat polymerization is that they are being reallocated from food production. Therefore, other types of biomasses, such as algae, lignins, celluloses, and polysaccharides, were proposed as raw materials (**Table 3**). They are also affordable, available worldwide, and in some cases they are extracted from some industrial by-products and wastes (wood, wood pulp, starch, etc.).^[111]

Sutton et al. (2018) functionalized lignin with methacrylic anhydride and mixed different ratios of it (5, 10 and 15 %) with ethoxylated pentaerythritol tetraacrylate and aliphatic urethane acrylate. The mixtures were compared with a commercial resin named PR48, where the sample containing 10 wt% of modified lignin not only demonstrated similar curing properties and viscosity but higher tensile strength and elongation at break, 63.6% and 220.8%, respectively.^[112] Bassett et al. (2020) used a 1 Pot, 2 Steps (1P2S) system to first react vanillin with methacrylic anhydride, producing methacrylated vanillin (MV) and methacrylic acid, and then adding glycidyl methacrylate to generate glycerol dimethacrylate (GMD). The final bio-based resin was composed of MV and GMD in a 1:1 molar ratio. The MV-GDM resin showed a tensile strength 20.3 MPa and elongation at break of 0.8, respectively. Moreover, its T_g and Young's modulus were equal to 153 °C and 4.9 GPa, respectively, which was comparable to high performance petroleum-based resins.^[113]

2.3.2 (Bio)degradable materials

According to the International Union of Pure and Applied Chemistry (IUPAC), biodegradable polymers are defined as “polymers, susceptible to degradation by biological activity, with the degradation accompanied by a lowering of its mass”.^[114] Generally, the biodegradation of a polymer can be divided into four steps:

- i. Biodeterioration;
- ii. Depolymerization;
- iii. Bioassimilation;
- iv. Mineralization.

In the first step, microorganism accumulates on the polymer surface, creating a biofilm that breaks the material into smaller particles. Then, these microorganisms secrete extracellular enzymes that start the depolymerization, in which the polymer chain is broken into oligomers, dimers and/or monomers. Next, the small molecules formed are assimilated by the microorganism, and a process of primary and secondary metabolization begins. Finally, these small molecules are mineralized and end products such as CO₂, H₂O, CH₄ and N₂ are released into the environment.^[115]

Unfortunately, during the UV curing process of most vat photopolymerization resins the cross-linked structure formed is so entangled that it limits the biodeterioration step, making it difficult for microorganisms to break the polymer down into small molecules.^[116] To circumvent this limitation, polymers that are known for their biodegradability, such as poly(propylene) fumarate (PPF)^[117,118], poly(lactide) (PLA)^[119,120], poly(ϵ -caprolactone) (PCL)^[121–123], and poly(trimethylene carbonate) (PTMC)^[124–126], have been introduced to resin structure using techniques like grafting or addition (**Figure 20**).^[125,127]

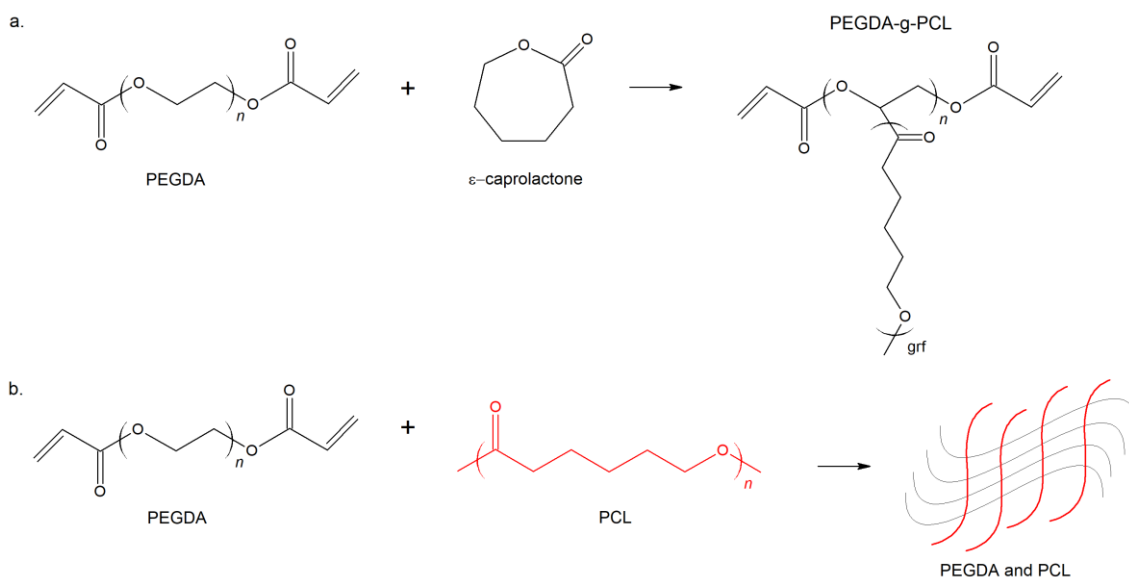


Figure 20: PEGDA polymeric structure modification by grafting or addition techniques.

The first biodegradable resin reported for SLA was proposed in 2000 by Matsuda et al, where they copolymerized ϵ -caprolactone (CL) and trimethylene carbonate (TMC). The final copolymer had a molecular weight varying from 2500 to 12 000 g mol⁻¹ and after 3 days submerged in an alkaline solution, the PTMC-PCL copolymer started to show signs of degradation on its surface.^[128] Kuhnt et al. (2019) fabricated different monomer ratios of PTMC-PCL using tri(ethylene glycol) (TEG) as an initiator. The resulting copolymers were combined with urethane acrylates and applied in DLP to fabricate films. These films were then subjected to 30 days of accelerated degradation tests (under alkaline conditions), where depending on the copolymer molar ratios, they showed a weight loss variation of 4% to 13%.^[129] Using a modified approach of ^[107], Wu B. et al. (2019) directed converted waste cooking oil into a biodegradable resin. The resins had an acrylation degree of 60.9% and were able to print detailed features down to ~100-micron resolution. The team also performed soil burial tests, in which the samples were kept for 14 days at 25 °C and 30% of humidity and showed a weight loss of approximately 25%. Finally, **Table 3** presents more examples of biodegradable resins for vat photopolymerization.^[130]

2.3.3 Biocompatible materials

As the application of 3D printing in medicine continues to grow, in both volume and areas, there is a demand for new materials having different types of biocompatibility characteristics. Biocompatible materials must be suitable for entering into contact with living tissues without resulting in adverse effects. Additionally, they must be tested following a standard, like the ISO 10993, and certificated by a regulatory agency.^[131]

In vat photopolymerization, as reported by Guttridge et. al (2021), there are several types of biocompatible resins currently available on the market. These resins are separated into three groups, (i) dental, (ii) medical and (iii) general medical, and they can be produced from petroleum or biomass.^[131] However, as previous discussed, there has been a push for using materials that are more environmental friendly.

Some biodegradable materials, like PLA, PCL, PPF can be also used for medical applications. For instance, Elomaa et al. (2020) functionalized PCL with methacrylic anhydride (MA) creating PCL-MA that was latter combined with gelatin methacryloyl (GelMA). The addition of GelMA into the hybrid resin resulted in an improvement of cell proliferation when compared to the neat PCL-MA. Moreover, the 70/30 wt.% mixture ratio of PCL-MA/GelMA at 32 °C had suitable properties to be able to print intestinal tissue scaffolds.^[132]

Table 3: Biobased, biocompatible, and biodegradable photosensitive materials for stereolithography 3D-printing.

Category	3D printing technology	Material source	Bio content (%)	Tensile strength (MPa)	Elongation at break (%)	Max degradation (%)	Refs
Biobased	SLA	Vanillin	50	20.27 ± 2.24	0.83 ± 0.1	-	[113]
	SLA	Lignin	15	15 ± 8	6 ± 1	-	[112]
	Custom	Palm oil	-	5.2 ± 1.2	12.5 ± 0.19	-	[133]
	DLP	Soybean oil	79.8	36.4 ± 0.4	18 ± 3	-	[134]
	SLA	Soybean oil	40.5	~23	~25.5	-	[135]
	TPP	Linseed oil	93	31.54 ± 2.72	1.92 ± 0.06	-	[81]
	DLP	Soybean oil	75.3	37.2 ± 3.4	16.1 ± 1.8	-	[81]
	SLA	Guaiacol + Eugenol	-	61.7 ± 5.1	8.9 ± 1.6	-	[136]
	DLP	Fumaric acid	-	~20	~17	-	[117]
(Bio)degradable	Custom	Alginate	-	~22	~9.5	98.5	[137]
	SLA	PDLLA-PEG-PDLLA	-	~0.9	~50	100 ^a	[78]
	SLA	PCLMA	-	~0.8	~1.2	50	[138]

Biocompatible	DLP	PCL	-	2.87 ± 0.12	78.5 ± 6.7	-	[121]
	Custom	PLGA-diacrylates	-	~1.6	~42	-	[139]
	DLP	Gel-g-PTMC	-	1.19 ± 0.04	59.6 ± 0.46	-	[125]

^aThe degradation test was performed on a 1 M NaOH solution (14 pH)

2.4 EPOXY-ACRYLATE SOYBEAN OIL (AESO)

Soybean oil (SBO), is the second most produced vegetable oil in the world, staying only behind of palm oil.^[140] It is derived from soybean, where typically the seeds have between 12-25% of oil in it.^[141] In 2022, 62.25 million tons of SBO were produced, where the majority of it went to food applications.^[142]

The process of producing soybean oil can be divided by three major steps: preprocessing, extraction and separation, and postprocessing. In the first step, the beans are cleaned, cracked, dehulled, and conditioned. This step is basically used to clean the crops and reduce their particle size to increase the oil recovery.^[143] In the second step, heat and pressure are applied to the beans to denature the oleosins and break the structure of seed (releasing some of the oil). It is during this step that hexane is added into the soybean pulp to extract the oil from it, where at the end of the process the hexane/oil mixture is transferred to a separation tank to have the hexane recovered. Most of the soybean oil produced nowadays is done by solvent extraction, except in some small-scale plants, where mechanical extraction is still used.^[144] The final step, postprocessing, is required to remove any material from the oil that is not suitable for human consumption. These materials include free fatty acids, non-hydratable and hydratable phospholipids, and colors and flavor components.^[144]

Different from other seeds, soybean oil has a unique fatty acid composition, which is partially resistant to environmental factors.^[141] According to Wu et al. 2018, almost 80% of fatty acids in SBO triglycerides are unsaturated, where they are usually composed of oleic acids, linoleic acids, and linolenic acids. Therefore, SBO can easily have the double bonds in its structure modified through acrylation and epoxidation to be used for 3D-printing.^[145]

Indeed, recently, some authors have reported modifying SBO to be used for developing highly complex structures,^[146] stimuli-responsive scaffolds,^[147] biocompatible materials,^[148] where it demonstrated good biocompatibility, thermal, optical and mechanical properties. For instance, Voet et al. (2020) tested various ratios of isobornyl methacrylate (IBOMA), a diluent,

with trifunctional epoxidized soybean oil acrylate (ESOA₃) and difunctional/trifunctional epoxidized soybean oil methacrylate (ESOMA₂ and ESOMA₃, respectively) to create a bio-based resins that have mechanical properties like commercial petroleum-based resins. The combination of IBOMA:ESOA₃ had the highest tensile strength (43.7 MPa) of all resin, while the IBOMA:ESOMA₂ the highest elongation at break (24%). Moreover, all resins had bio-renewable carbon content greater than 75%.^[134] Cui et al. (2020) mixed a modified SBO with urethane groups in it (SBO-URE) with isobornyl acrylate and difunctional epoxy acrylate to create a dual-curing hybrid resin. According to their results, the addition of 10 wt.% SBO-URE increased the tensile strength by approximately 30% from 16.8 to 23.9 MPa, while decreasing the elongation at break by only 12.5% from 23.2 to 20.3%. Moreover, the addition of 10 and 20 wt.% of SBO-URE also improved the printed parts flexural strength and modulus and reduced the effects of shrinkage.^[135]

Among the many SBO modifications, AESO (**Figure 21**), has been demonstrating to be a promising material in various fields, such as coating, adhesives, composites and resins. AESO is known to approximately have a tensile strength and elongation at break of 5 MPa and 8%, respectively, a bio renewable carbon content of 80.3%, water contact angle of 105°, and a complex viscosity (at 25 °C) of 12 Pa s.^[149,150] Furthermore, AESO can also be used as starting material for further synthesis or in combination with other materials. Lebedevaite et al. (2020) performed a similar investigation, however instead of testing different types of modified soybean oil, it combined acrylated epoxidized soybean oil (AESO) with several reactive diluents: isobornyl methacrylate (IBOMA), methacrylic ester (ME), tetrahydrofurfuryl acrylate (THFA), and tetrahydrofurfuryl methacrylate (THFMA). Their bio-renewable carbon content were estimated to be between 75-82%. Furthermore, the AESO:THFMA combination demonstrated mechanical properties similar to some petroleum-based commercial resins, with a tensile strength of 37.2 MPa and an elongation at break of 16.1%.^[81] Grauzeliene et al. (2021) combined AESO with a thiol-ene monomer (SQ6SH) to fabricate thermoset parts with higher rigidity. The printed parts

showed a storage modulus between 1.78 to 2.67 MPa, glass transition temperature of -2 to 0 °C, a shore A hardness value of 70 to 77 and lower swelling value (less than 4.5%).^[151]

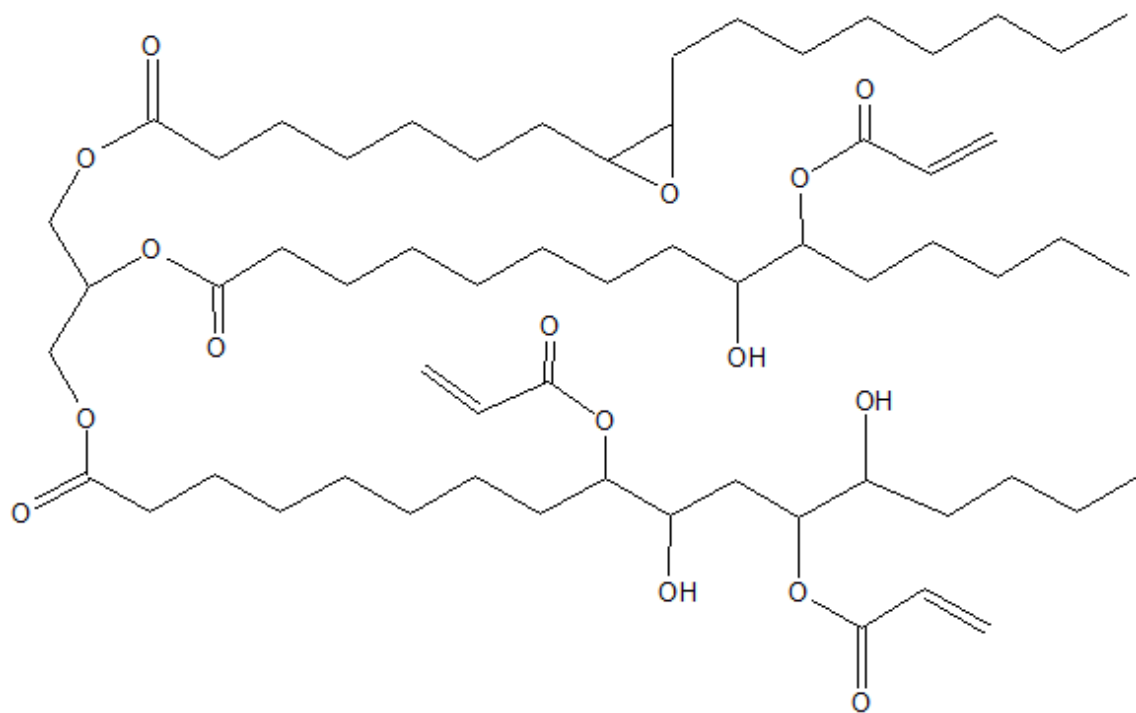


Figure 21: Acrylated epoxidized soybean oil structure.

CHAPTER 3

MATERIALS, METHODS, AND CHARACTERIZATIONS

In this chapter it is presented the materials, methods, and instrumentations employed for the physical and chemical characterizations of the photosensitive resins and parts fabricated with them. Epoxy-acrylate soybean oil was used in all experiments, as base or additive, where its performance was compared to other research or commercial resins.

The section 3.1. was divided in subparagraphs, each one presenting a list of the materials used for the studies developed during the Ph.D. research. Furthermore, the methods and characterization techniques applied for all research are described in detail at section 3.2.

3.1 MATERIALS

In the following subparagraphs a list of all materials used in this thesis is reported. These materials were divided according to the study they were employed. All chemicals reported here were used as received, without further purifications.

3.1.1 Photosensitive acrylates containing bio-based epoxy-acrylate soybean oil.

Epoxy-acrylate soybean oil (containing 4000 ppm monomethyl ether hydroquinone as inhibitor), and diphenyl(2,4,6-trimethylbenzoyl) phosphine oxide (TPO) were purchased from Merck KGaA (Darmstadt, Germany). Isopropanol ($\geq 99\%$) was received from Carlo Erba. Peopoly Moai standard clear resin (PY) was purchased from 3Dpartnershop company: it is an acrylic-based photopolymer designed for the Moai printer, containing urethane acrylate (30%–50%), bisphenol A ethoxylate diacrylate (30%–50%) and benzophenone as the photoinitiator (5 wt%).

3.1.2 Synthesis of a biobased resin for multipurpose applications

Epoxy-acrylate soybean oil (containing 4,000 ppm monomethyl ether hydroquinone as inhibitor) (AESO), isobornyl methacrylate (IBOMA), and diphenyl(2,4,6-trimethylbenzoyl)phosphine oxide (TPO) were purchased from Merck KGaA (Darmstadt, Germany). Isopropanol 99% was purchased from Carlo Erba.

3.1.3 Synthesis of a biobased and biocompatible resin for medical applications.

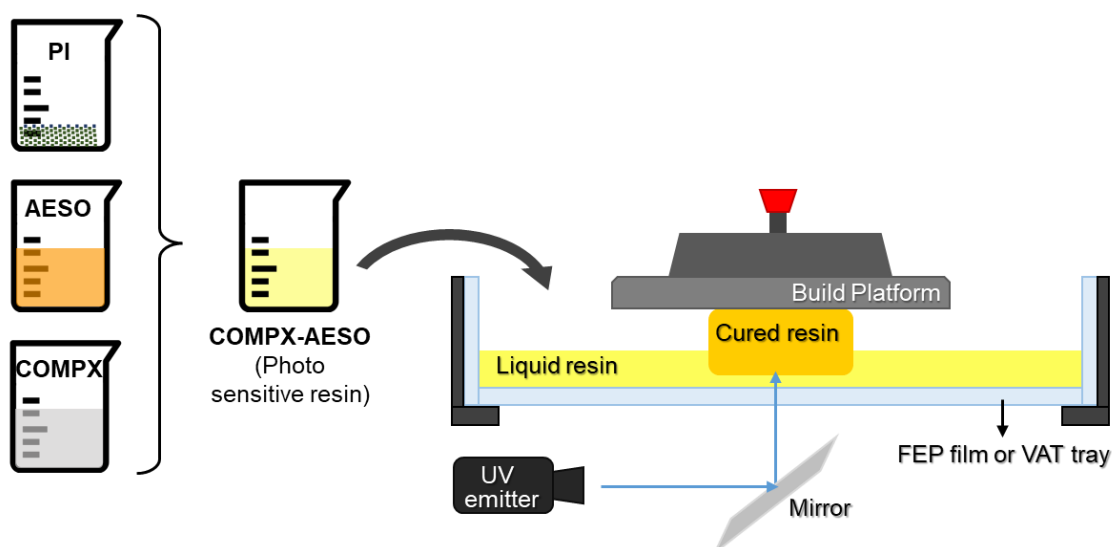
Poly(ethylene glycol) diacrylate (number average molecular weight: 575), epoxy-acrylate soybean oil (containing 4000 ppm of monomethyl ether hydroquinone as inhibitor), diphenyl(2,4,6-trimethylbenzoyl)phosphine oxide (TPO). Isopropanol (purity: 99%) was purchased from Carlo Erba (Cornaredo, Italy).

3.1.4 Reinforcement and characterization of biobased resins with micro- or nanocrystalline cellulose

Poly(ethylene glycol) diacrylate (number average molecular weight: 575), epoxy-acrylate soybean oil (containing 4000 ppm of monomethyl ether hydroquinone as inhibitor), diphenyl(2,4,6-trimethylbenzoyl)phosphine oxide (TPO), and cellulose micro-crystalline powder (20 μm) were purchased from Merck KGaA (Darmstadt, Germany). Cellulose nanocrystals were purchased from Sappi limited (Maastricht, the Netherlands). Isopropanol (purity: 99%) was purchased from Carlo Erba (Cornaredo, Italy).

3.2 PREPARATION OF SAMPLES AND CHARACTERIZATIONS

The samples discussed in the following chapters were prepared following a similar approach as described by **Scheme 6**. Using a lightproof beaker, different amounts of AESO were combined with COMPX (which can refer to PY, IBOMA, and PEGDA). The substances were mixed using a magnetic stirrer until they had become completely homogeneous. Then, an Y wt.% of photoinitiator (depending on the COMPX used) was grinded using a mortar to a fine dust and added to the mixture that was agitated again. After the photopolymer was completely dissolved, the mixture was left to rest to remove any bubbles and added to the 3D printer. A more detailed description of the ratio between each substance, as well as the fillers are presented in the experimental section of each discussion chapter.



Scheme 5: Simplified description of the preparation and 3D printing process of photocurable systems. The term COMPX refers to PY, IBOMA, and PEGDA.

3.2.1 3D printing process

The samples were printed using a Peopoly moai 130 SLA 3D printer with an easy-to-level build plate. The machine is equipped with a 150-mW solid-state laser emitting light at a wavelength of 405 nm. The power level for printing all samples was set as 58, which corresponds to 99.37-mW of power, and the initial exposure time was in the range between 40s and 60s. The printed process was carried out maintaining the temperature inside the printer constant at 25 °C. After the printing process was finished, the excess of resin was drained and washed off using isopropanol; then, the samples were gently dipped into distilled water for 5 min. Finally, the samples were dried using paper towels and transferred to a UV chamber equipped with a 60W UV Mercury Lamp (with a wavelength of 405 nm). All samples were set at a 30 cm distance from the lamp where its front and back sides were each post-cured for 20 min (the total post-curing time was 40 min). The post-curing time was the same for all samples to ensure a complete photopolymerization, as assessed by FTIR spectroscopy.

The 3D models were created using FreeCAD software (version 0.18), and the slicing were done using Ultimaker Cura (version 3.5.1) and Asura3D (version 2.25). The layer height of the samples was set as 0.1 mm and they were all printed horizontally.

3.2.2 FTIR Spectroscopy

Fourier-transform infrared spectroscopy (FTIR) was used to investigate the photopolymerization reaction by monitoring the conversion of the acrylic double bonds. The infrared analysis was performed using a Thermo Avatar 370 spectrophotometer equipped with an attenuated total reflectance (ATR) device with a diamond crystal for solid analysis. Using Omnic 7.3 software, the spectra were collected in absorbance mode with a resolution of 4 cm^{-1} and 32 scans per measurement, within the range of 4000 to 650 cm^{-1} . Furthermore, all the spectra were normalized using the C=O peak as reference. Finally, the conversion of vinyl groups, acrylic consumption and epoxy double bonds were calculated from the decrease in the area of the double-bond absorption peak at 1620 - 1640 cm^{-1} , 810 cm^{-1} , 910 cm^{-1} , respectively, as shown by **Equation 20-23**.^[135]

$$\text{Acrylic double bonds conversion (\%)} = \left(1 - \frac{A_{t(1630)}}{A_{0(1630)}}\right) \times 100\% \quad (\text{Eq. 20})$$

$$\text{Vynil groups conversion (\%)} = \left(1 - \frac{A_{t(810)}}{A_{0(810)}}\right) \times 100\% \quad (\text{Eq. 21})$$

$$\text{Epoxy groups conversion (\%)} = \left(1 - \frac{A_{t(910)}}{A_{0(910)}}\right) \times 100\% \quad (\text{Eq. 22})$$

where $A_{0(1630)}$, $A_{0(810)}$, $A_{0(910)}$, and $A_{t(1630)}$, $A_{t(810)}$, $A_{t(910)}$ are the areas of the peak at 1630 cm^{-1} , 810 cm^{-1} , 910 cm^{-1} before and after exposure to UV irradiation, respectively.

3.2.3 Rheological analysis

Rheological measurements were performed to evaluate the viscosity of resins and composites before the printing process. Knowing and controlling the viscosity is fundamental when developing a resin for 3D printing applications, where it must be fluid enough to fill the gaps each time the build platform raises. Failing to do so can lead to miss prints and broken parts. The viscosity of commercial resins, such as Formlabs or Anycubic, is usually between 0.1 Pa·s and 1.5 Pa·s.^[152] However, depending on the machine and its configurations it is possible to print resins with 5 Pa s.^[153]

An ARES (TA Instrument, Waters LLC, New Castle, USA) strain-controlled rheometer in parallel plate geometry (plate diameter: 50 mm; gap between the plates: 0.7 mm) was used for the analyses. The complex viscosity of the samples was measured through strain sweep measurements in a range of strain amplitude from 1% to 400%. In all tests, the frequency was fixed at 1 rad·s⁻¹. All measurements were performed at room temperature.

3.2.4 Tensile measurements

All tensile tests were performed following the ASTM D638 standard. For each experiment, five dog-bone shape samples were printed with the dimensions of 63.5 × 9.53 × 3.2 mm (L × W × T) and with 3.2 mm width in the narrow section. The tests were performed at room temperature with an Instron 5966 dynamometer (Norwood, MA, USA), equipped with 5 kN load cell. Each test was performed at a crosshead speed of 10 mm/min. Tensile strength (MPa) and elongation at break (%) were determined using the average of the five tests. Then, others mechanical properties were calculated using the data from the tensile curves, such as Young's modulus (MPa) and fracture energy (mJ).

3.2.5 Scanning electron microscopy

The morphology of the obtained 3D-printed parts was studied using an EVO 15 scanning electron microscope (SEM) from Zeiss (Oberkochen, Germany), coupled with an Ultim Max 40 energy dispersive X-ray (EDX) microanalyzer by Oxford Instruments (High Wycombe, UK); the samples were fractured in liquid nitrogen, fastened to a conductive adhesive tape, and finally gold-metallized. The samples were analyzed using a secondary electron detector, with energy set at 20.00 kV, at two magnifications (1000 \times and 2500 \times).

3.2.6 Thermogravimetric analysis

The thermal and thermo-oxidative stability of all prepared systems was assessed by thermogravimetric (TG) analyses carried out on a Discovery apparatus (TA Instruments), from 50 to 700 °C, using a heating rate of 10 °C \cdot min⁻¹, under both nitrogen and air flow (35 and 25 mL \cdot min⁻¹, respectively). The experimental error was $\pm 0.5\%$ for the weight and ± 1 °C for the temperature.

3.2.7 Swelling analysis

Swelling analysis was performed following the procedure described by Wu et al, 2018.^[145] For each experiment five rectangular samples with dimensions of 30 \times 10 \times 5 mm (L \times W \times H) were fabricated and then weighed (M_1). The samples were then dipped into deionized water for a total period of 30 days. Every 5 days, the samples were taken from the water, dried using a dry cloth, and weighed again (M_2). The swelling percentage variation, S_w , was calculated using **Equation 23**.

$$S_w = \frac{(M_2 - M_1)}{M_1} \times 100\% \quad (\text{Eq. 23})$$

3.2.8 Contact angle measurement

Static contact angle values of the experiments were measured using a custom-made instrument equipped with a high-speed CCD camera. The used equipment allows the determination of contact angle, with a precision of $\pm 1^\circ$, by taking images at frequencies as high as 200 Hz, starting within a few tens of milliseconds after the deposition of the drop. All measurements were performed at room temperature and relative humidity $\text{RH} = 40\% \pm 5\%$. Five rectangular-shaped parts (size: $50 \times 25 \times 1 \text{ mm}^3$) were 3D-printed for each formulation/experiment. A small drop of high purity distilled water was slowly placed on the surface of the samples, and various photos of the droplet were recorded after 5s. The volume of the water drop was $4 \pm 0.5 \text{ }\mu\text{L}$. The contact angle (CA) values were determined using ImageJ and the drop analysis package.

3.2.9 Working curve

During the development of an UV sensitive resin, it is fundamental to know two key constants: the penetration depth at which the intensity of the beam is reduced to $1/e^2$ (13.5%) of its value at the surface known as D_p and E_c , which is the exposure per unit of area needed for the resin to reach its gel point.

In order to calculate these two constants, the first step is to rearrange the general exposure equation (**Equation 19**) by setting the locus of points in the resin that are at their gel point ($E = E_c$), as y^* and z^* , as shown by **Equation 24**.

$$e^{-2y^{*2}/W_0^2} + e^{-z^*/D_p} = \sqrt{\frac{2P_L}{\pi W_0 V_s E_c}} \quad (\text{Eq. 24})$$

The second step is to take the natural logarithms of both sides of Equation 24, as shown below (**Equation 25**).

$$2\frac{y^{*2}}{W_0^2} + \frac{z^*}{D_p} = \ln \left[\sqrt{\frac{2P_L}{\pi W_0 V_s E_c}} \right] \quad (\text{Eq. 25})$$

Next, Equation 25 is solved for z^* and setting $y = 0$, the cure depth of the resin can be described as following:

$$C_d = D_p \ln \left[\sqrt{\frac{2P_L}{\pi W_0 V_s E_c}} \right] \quad (\text{Eq. 26})$$

Where the maximum laser exposure on the resin surface, known as E_{max} , is described as:

$$E(0,0) \equiv E_{max} = \sqrt{\frac{2P_L}{\pi W_0 V_s}} \quad (\text{Eq. 27})$$

where n is the number of times the laser passed over the tile, P_L is the laser power, W_0 is the beam width, and V_s is the scanning speed. Finally, by substituting **Equation 26** in **Equation 27**, the working curve equation is obtained:

$$C_d = D_p \ln \left(\frac{E_{max}}{E_c} \right) \quad (\text{Eq. 28})$$

Where C_d is the cure depth of a single layer. D_p and E_c can be estimated by varying the resin exposure time and measuring the cured layer depth. To this aim, a square part composed of 25 equal-area square tiles (1 mm^2), based on the model described by Bassett et al. 2020,^[113] as shown in **Figure 22**, was printed using the Peopoly moai 130 SLA printer.

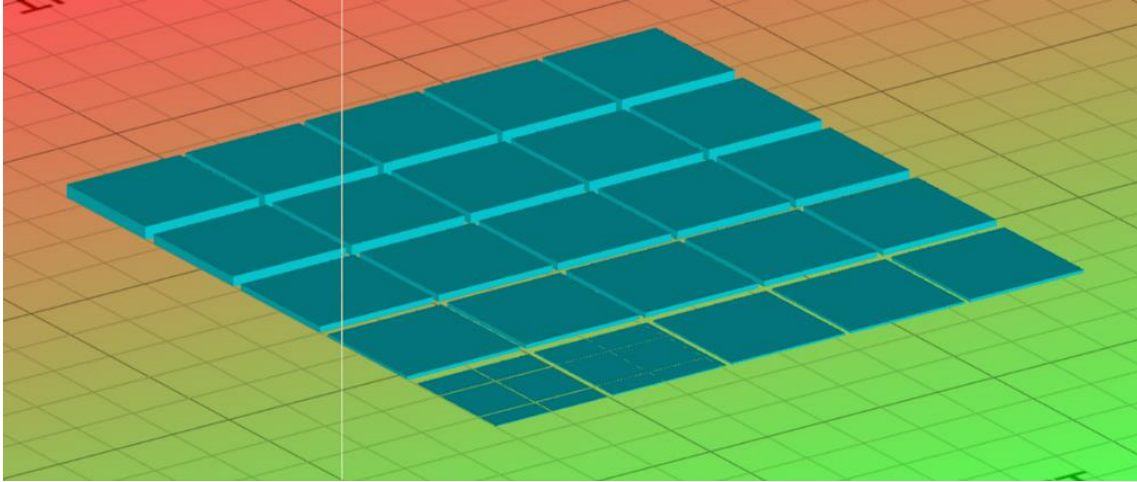


Figure 22: The 3D model used to determine the resin curing characteristics.

The part had 25 layers in total, with the height of each layer being 0.05 mm. Each square was exposed to light in an arithmetic progression increasing from 1 to 25. Furthermore, to avoid the effect of light scattering, the squares were separated by a gap of 1 mm. The height of each tile was measured three times using a digital caliper with 0.01 mm of resolution (Preciva Digital Caliper) and a $\pm 10\%$ deviation was assumed.^[154] Finally, with the height of each tile, the maximum exposure of a tile was calculated using **Equation 28**.

P_L and W_0 values are specific to the 3D printer; in this case, they were 150 mW and 0.07 mm, respectively. Three parts were printed with scanning speeds of $80 \text{ mm}\cdot\text{s}^{-1}$ and $200 \text{ mm}\cdot\text{s}^{-1}$.

When the fillers are added to the mixture, the light scattering effect exerted by these particles needed to be taken into account.^[155] Thus, D_p was adjusted to consider the scattering effect, as shown by **Equation 29**.

$$D_p = \frac{2}{3} \frac{d}{Q\phi} \quad (\text{Eq. 29})$$

where d is the filler mean size, ϕ is the filler volume fraction, and Q is the scattering efficiency. Q was calculated according to **Equation 30**, in which λ is the irradiation wavelength, h is the interparticle distance, and Δn is the difference in refractive index between the filler (n_f) and the photosensitive material (n_0).

$$Q = \frac{h}{\lambda} \Delta n^2 \quad (\text{Eq. 30})$$

CHAPTER 4

PHOTSENSITIVE ACRYLATES CONTAINING BIOBASED EPOXY-ACRYLATE SOYBEAN OIL

In this chapter, a standard petroleum-based resin containing urethane acrylate and acrylic monomers was combined with epoxy-acrylate soybean oil (AESO), aiming to reduce its impact on the environment. Before the description of the experimental part and discussion of the main results, a short introduction about the current state of the UV resins for 3D-printing, their applications, composition, mechanical properties and environmental impact was presented. Materials, general methods, and instrumentation for characterization were reported in the previous chapter.

4.1 INTRODUCTION

Vat photopolymerization (VP), one of the seven methods of additive manufacturing, has proved to be an efficient technique to fabricate high precision components for several

applications, from simple toys and jewelries to medical devices and aerospace components.^[18,156] Compared to traditional manufacturing techniques, VP has the advantage of generating less waste, freedom of design, market adaptability and the production of complex structures.^[9,11] Usually, photopolymer materials are divided into six categories: standard, structural, flexible (elastic), tough (or durable), ceramic and castable wax, each one for a specific application.

Standard resins are the commonest among all the photopolymer materials, being used especially for quick prototyping. They are available in different colors, prices, and can be used in most 3D printers. The second type, structural resins, are known to withstand higher temperatures (in some cases up to 289 °C), have higher rigidity and finishing details. They are used for printing turbine blades, fans, connections, tooling, electronic covers, and cabinets. Tough resins (third type) are made from polyethylene (PE), acrylonitrile butadiene styrene (ABS-like) or polypropylene (PP) which leads to parts with high ductility, impact resistance and deformation. This resin is usually used for fabricating jigs and clamps, or parts that undergo significant impact. The fourth type of resins are used to produce flexible components. These resins are made of elastomeric polyurethane (EPU) or polymers with similar characteristics. Due to their high elasticity, low stiffness, and ductility, they are widely used in orthotic and prosthetic devices. Ceramic resins are a combination of photopolymers and silica particles. These resins normally require special configurations or printers to be used in. Moreover, after the part is printed, they need to be post processed in high temperatures to remove the polymer matrix leaving only the ceramic structure. Lastly, castable wax resins have been used to create parts with smooth surfaces and high details. They are employed to create master patterns often for jewelry and orthodontics. The mechanical properties of well-known commercial resins are summarized in **Table 4**.

Even though the variety of resins available nowadays are increasing, most of them are derived from petroleum, which raises many environmental concerns, such as CO₂ emission, materials toxicity, and plastic waste.^[135] The latter is already destroying many ecosystems around the planet. According to Lebreton et al.^[157] projections, if humanity maintains the current rate of plastic waste production, it will generate 380 million metric tons (Mt) in 2060, a 90% increase

from what was produced in 2020 (200 Mt).^[157] Part of the plastic waste will inevitably come from AM as the 3D printing market is growing, with many industries transiting to it.^[5]

To address the growing amount of plastic waste, from the past decades, a lot of research and investment was allocated in plastic recycling, with many governments and companies incentivizing using it. However, new studies and reports on the effectiveness of recycling suggests that approximately only 9% of total plastic produced is recycled, 19% is incinerated, 50% ends up in landfill and 22% completely evades the waste management system.^[158] Furthermore, the 2022 Greenpeace report suggests that plastic recycling has been declining in the last years, going from 8.7% in 2018 down to 5% in 2021.^[159] Therefore there is a need on developing new strategies to deal with plastic waste.

One alternative that is gaining traction is the development of biobased and biodegradable materials or composites. These materials not only are produced from natural sources, but also promotes green growth and circular economy.^[160] Vegetable, one of the many types of biobased material, have proved to be a good alternative for developing plastics. They can have their chemical structure modified to produce different types of polymers.^[161]

In this study, a vegetable-based resin was used to improve the biocontent of a standard commercial resin and its effect on various properties (namely, thermal, mechanical, and structural) was investigated. The bio-resin used was acrylated epoxidized soybean oil (AESO), derived from soybean oil. The reduction in fossil-derived compounds and the simple procedure here developed (not requiring complicated purification steps) suggest the proposed protocol could be a promising solution for industrial-scale exploitation, reducing the environmental impact and fulfilling the circular economy concept.

Table 4: Mechanical properties of various popular commercial resins.

Type	Company	Product name / ID	Ultimate strength (MPa)	Elongation at break (%)	Flexural modulus (GPa)	Hardness shore	Notched Izod (J/m)
Standard	Formlabs	FLDRGR02 ²	36	5	1.8	-	29
	Formlabs	FLGPCL04	65	6.2	2.2	-	25
	Anycubic	Standard	36 - 52	15 - 22	1.2 – 1.8	84 D	-
	Elegoo	Standard	36 - 53	14.2	-	84 D	-
	eSUN	Standard	46 – 67	28 – 36	-	78 – 82 D	14 – 42
	Peopoly	Standard	33	4.3	-	85 D	-
Structural	Formlabs	FLPRGR01	61	13	2.2	-	18.7
	Anycubic	Craftsman	35 – 50	8 – 12	1.2 – 1.6	82 D	-
	eSUN	Precision model	36 – 62	25 – 40	-	81 – 86 D	30 – 40
	Siraya Tech	Engineering	39	25	-	85 D	-
Flexible	Formlabs	FLFLGR02	7.7 – 8.5	75 - 85	-	80 – 85 A	-
	Formlabs	FLELCL01	3.23	160	-	50 A	-
	Anycubic	Flexible/Tough	35 - 45	30 - 50	0.9 – 1.2	76 D	50 - 60
	Siraya Tech	Flexible	30	70	-	65 D	-

	Formlabs	FLTO1501	33	51	1.4	-	67
	Formlabs	FLTO2001	46	48	1.9	-	40
	Formlabs	FLDUCL02	28	55	0.66	-	114
Tough	Anycubic	ABS-like	35 – 55	20 – 30	1.4 – 1.6	84 HS	-
	Elegoo	ABS-like	30 – 52	-	1.8 – 2.4	75 D	41 - 48
	eSUN	Hard-Tough	30 – 60	35 – 52	-	75 – 81 D	40 – 110
	Peopoly	Nylon-like	62	44	-	82 D	-
	Siraya Tech	Tough	50	32	-	85 D	-
Ceramic	Formlabs	FLCEWH01	5.1	1.4	-	-	18.4
	Formlabs	FLCWPU01 ¹	12	13	-	-	-
Castable Wax	eSUN	Castable jewelry	42 – 62	11 – 20	-	60 D	44 – 49
	Siraya Tech	Castable	20	5	-	70 D	-

4.2 EXPERIMENTAL PART

4.2.1 Photocurable resin formulation

The photocurable formulations for 3D printing were prepared by mixing different weight ratios of AESO (namely 10, 20, 30, 40, and 50 wt%) with Peopoly Moai standard resin (PY) without the addition of photoinitiator, as it is already present in the formulation of the commercial resin. However, by increasing the amount of soybean oil, the photoinitiator already added to the PY resin may not be enough to drive the polymer network formation. To investigate the influence of the photoinitiator on the photocuring process of the formulation with the highest concentration of soybean oil (i.e., 50 wt%), 1 wt% of TPO was added. This formulation was then ultrasonicated for 60 min at 30 °C to thoroughly dissolve the photoinitiator. The resulting solutions were vigorously stirred for 30 min at 40 °C, and then, allowed to rest in the dark until bubbles were no longer present. Each composition was prepared in a room with minimal ambient light and stored in a dark place.

4.3 RESULTS AND DISCUSSION

In this paragraph, results and discussion of characterization analyses are provided and divided depending on the chemical-physical technique employed

4.3.1 FT-IR analysis

The addition of AESO in the PY_{uncured} resin could reduce the benzophenone (photoinitiator) efficiency, demanding longer curing times or resulting in failures. To check whether or not the concentration of benzophenone was sufficient to perform the photopolymerization, FTIR analysis was carried out in the mixture with the highest concentration of AESO (i.e. PY_{AESO50}). Moreover, FTIR analysis was also performed in samples with extra photoinitiator added, sample $PY_{\text{TPO1\%}}$ (**Figure 23**). The photopolymerization reaction was evaluated by monitoring the decrease of double bond peaks at 810 cm^{-1} and by calculating the conversion degree (Equation 20). Indeed, after UV irradiation, the decrease in the peak area at around 810 cm^{-1} , assigned to $\text{CH}_2=\text{CH}$ - twisting, indicated that $\text{C}=\text{C}$ bonds in the reactive monomers took part in the cross-linking reaction.

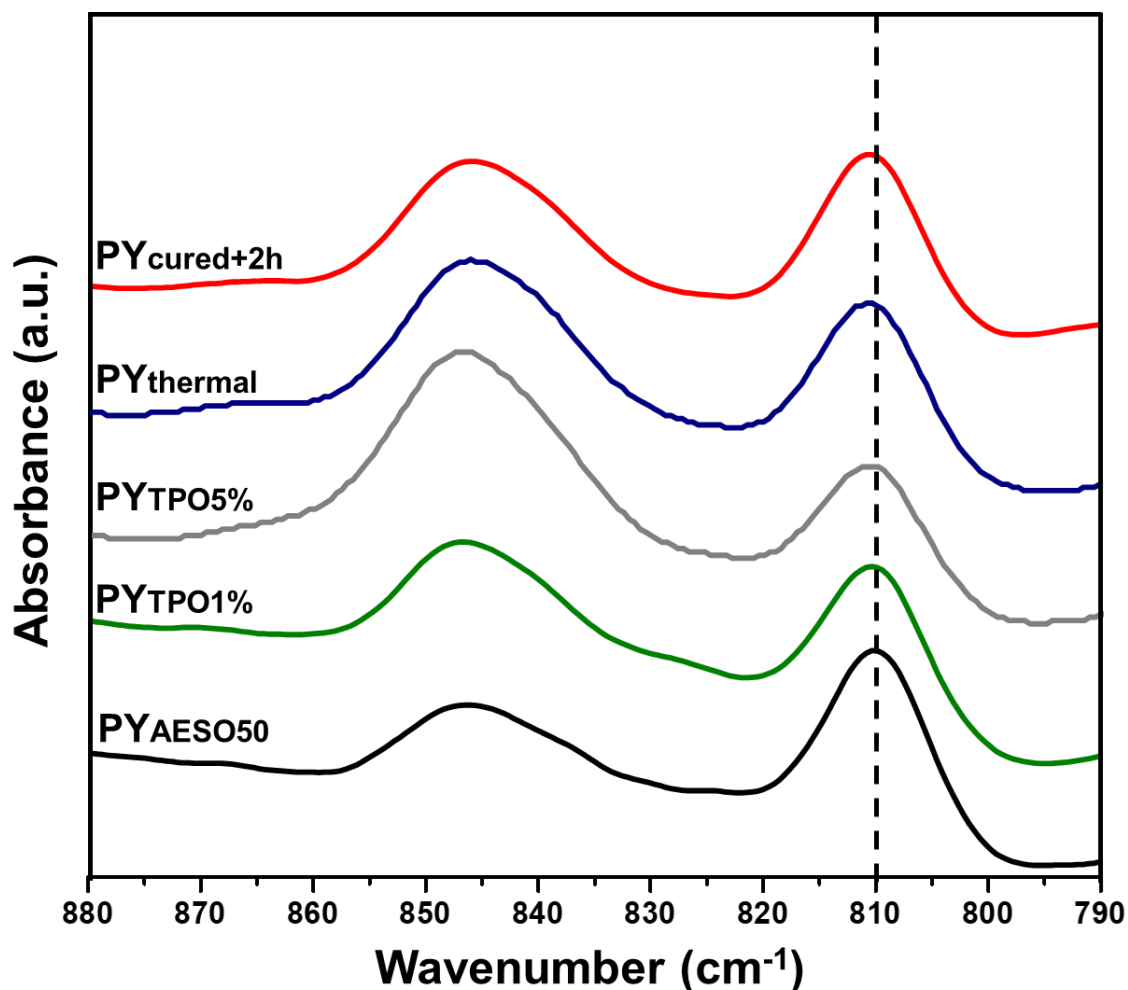


Figure 23: ATR-FTIR analysis of $\text{PY}_{\text{AESO50}}$ with and without TPO and PY_{AESO} at different types of post treatment process in the range of $840 - 800 \text{ cm}^{-1}$. The tested samples were post-cured for 40 min (20 min each side) under UV light.

However, since a certain intensity of the band at 810 cm^{-1} was still visible after UV irradiation, three experiments were carried out to investigate the C=C conversion by extending the UV exposure time to 2h ($\text{PY}_{\text{cured+2h}}$), applying a post-heat treatment ($\text{PY}_{\text{thermal}}$) and adding a further 5 wt.% photoinitiator ($\text{PY}_{\text{TPO5\%}}$). As shown in **Figure 23**, the absorption band at 810 cm^{-1} shows no significant difference. However, when calculating the double bond conversion, it become evident that performing thermal treatment before UV ($\text{PY}_{\text{thermal}}$) or leaving the samples to cure for longer periods of time ($\text{PY}_{\text{cured+2h}}$) had negative impact on conversion. This could be happening due resin degradation. Nevertheless, $\text{PY}_{\text{AESO50}}$ showed similar conversion than the mixture with extra 5% of photoinitiator. This finding supports the hypothesis that the

benzophenone in the fixed amount was enough to perform the UV-curing of 3D-printed specimens.

After having confirmed that the photoinitiator present in the PY resin was enough to perform the UV-curing reaction, infrared spectra of 3D-printed specimens with increasing concentrations of AESO were performed. The spectrum of uncured PY resin (PY_{uncured}) reveals the presence of C–NH stretching in the urethane unit at 1528 cm⁻¹, while the urethane carbonyl and N-H stretching vibrations appear at around 1700 and 3300–3400 cm⁻¹, respectively.^[162] In particular, the presence of two different absorbance bands at 1720 and 1694.3 cm⁻¹, assigned to C=O, is consistent with a different chemical environment for carbonyl groups on monomers. The absorption bands in the range 2860–2950 cm⁻¹ are associated with the C-H stretching vibration, while peaks at 1646.9 cm⁻¹ and 1615.2 cm⁻¹ are assigned to C=C stretching of allylic bond and double-bond present in the alkyl chain, respectively.^[163] Both absorption bands at 1235 and 1115 cm⁻¹ are ascribed to the -C-O-C- stretching vibration.^[164] Finally, an absorption peak can be observed at 910 and 810 cm⁻¹, indicating the existence of double bonds of epoxy and acrylate groups, respectively.^[165] During the curing process, under UV irradiation, the photoinitiator produces active radicals, opens the double bond groups in the PY monomers, and generates crosslinking, which permits the 3D print specimens to cure. The occurrence of photopolymerization was verified by monitoring the double bond peaks at 1646, 1615, 910 and 810 cm⁻¹ through FTIR spectra.^[166] At the end of the UV curing step, the peaks of the double bonds are strongly reduced. Furthermore, a small peak change from 1186.1 to 1159.9 cm⁻¹ corresponding to the shift of C-O-C groups, provoked by the C=C consumption, is observed. Thus, the reduction of both vinyl functionality of the acrylate polymer absorbance assigned at 985 cm⁻¹ and the decrease of the signals at 1410 cm⁻¹, related to the consumption of unsaturated double bonds (CH₂=CH-R) are observed.^[133,167] Accordingly, the peak at around 982 cm⁻¹, assigned to the out-of-plane bending vibration and stretching vibration of unsaturated hydrocarbon, also decreased significantly. New absorption bands at around 3369 and 1635 cm⁻¹ were assigned to

new amide groups obtained by the UV-induced reaction between urethane acrylate and acrylic monomers.

All the FTIR spectra registered from the 3D printed systems containing AESO confirmed the occurrence of the UV-induced polymerization observed for the pure resin (PY_{uncured}). As shown by **Table 5**, the absorption attributed to the stretching of the C=C group is strongly reduced in intensity, suggesting the effective formation of a network of saturated C–C bonds at the expense of soybean oil, epoxy, and vinyl groups. Furthermore, **Table 5** also shows that during the photopolymerization the epoxy groups were activate, without the need of adding a cationic initiator. However, low conversion of acrylic groups was also observed, where the highest value of 35% was when 50 wt% of AESO was added. This apparent low conversion could be due some type of diluent presented in the Peopoly Clear formulation that is overshadowing the peak area.

Table 5: Photopolymerization conversion degree of PY/AESO mixtures.

Sample code	Peak at 810 cm ⁻¹			Peak at 910 cm ⁻¹			Peaks at 1620-1640 cm ⁻¹		
	Initial area (cm ²)	Final area (cm ²)	Conversion (%)	Initial area (cm ²)	Final area (cm ²)	Conversion (%)	Initial area (cm ²)	Final area (cm ²)	Conversion (%)
PY _{AESO10}	0.2474	0.0880	64.43	0.0745	0.0264	64.56	0.2128	0.1920	9.77
PY _{AESO20}	0.2171	0.0496	77.15	0.0548	0.0218	60.22	0.1742	0.1900	9.07
PY _{AESO30}	0.2390	0.0625	73.85	0.0657	0.0200	69.56	0.1899	0.1946	2.47
PY _{AESO40}	0.2243	0.0536	76.10	0.0603	0.0241	60.03	0.1849	0.1809	2.16
PY _{AESO50}	0.2474	0.0745	69.89	0.0745	0.0363	51.28	0.2118	0.1356	35.98

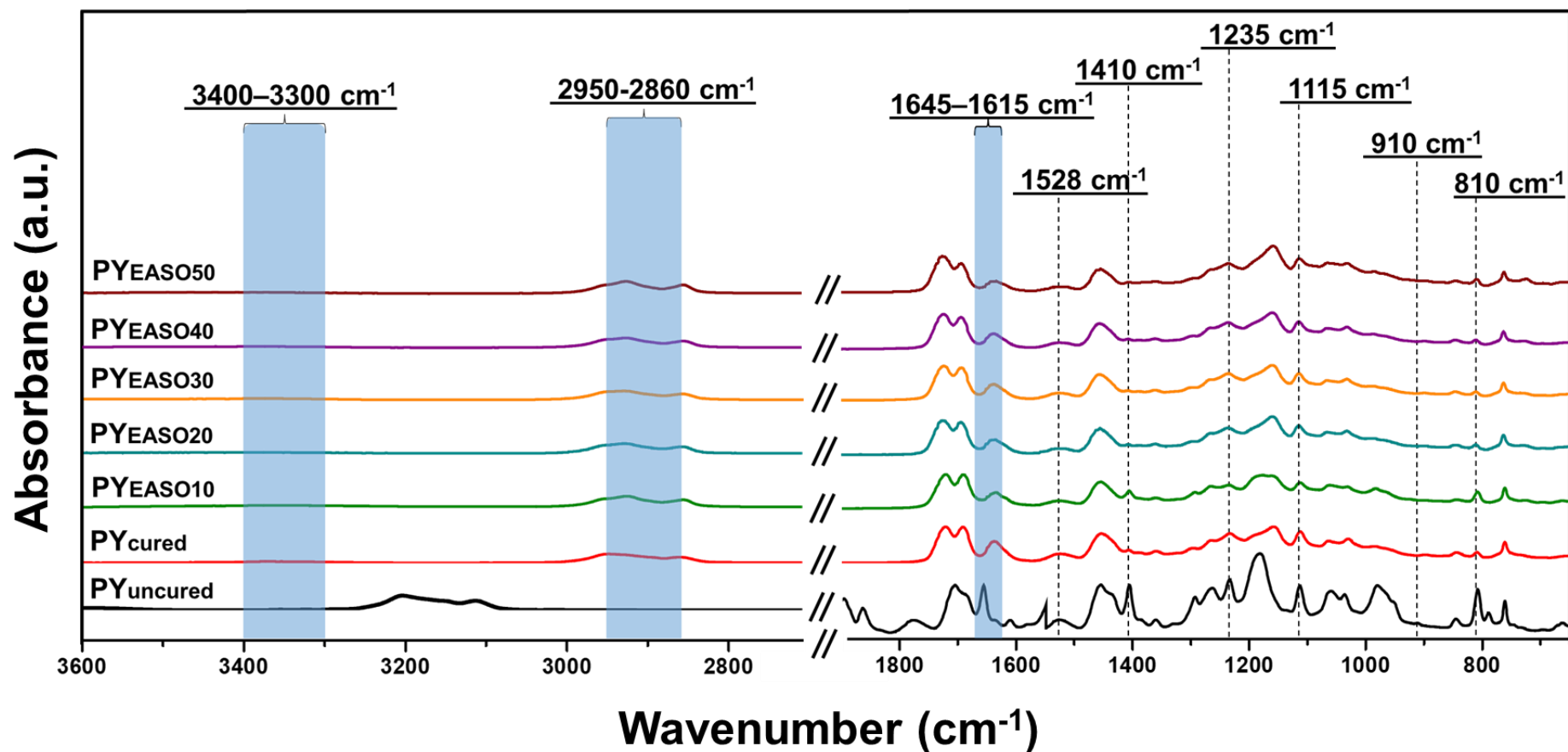


Figure 24: Infrared spectra under attenuated total reflectance of PY resin with different AESO concentrations (increasing from 10 to 50 wt.%). Only the sample PY_{uncured} was analyzed before being photopolymerized, the rest was after being 3D-printed and post-cured.

4.3.2 Rheology

The viscosity is a crucial factor that must be taken into consideration when developing a resin for VP application. The resin has a few seconds to fill the gap formed between the model and the building tray each time a new layer is printed.^[168] The viscosity commercial resins such as Formlabs or Anycubic, is usually between 0.1 and 1.5 Pa s,^[113] where the Peopoly moai clear resin exhibits a viscosity of 0.18 Pa s. As reported in **Figure 25**, pure AESO has a viscosity of approximately 15 Pa s at 30 °C, which is too high for most VP printers. When AESO was combined with the Peopoly resin, the PY viscosity increased according to the AESO load, from 0.27 to 1.06 Pa s for the formulations containing 10 and 50 wt.% of AESO, respectively. Nevertheless, the introduction of increased AESO loadings did not affect the range of linear viscoelastic behavior of the mixtures and all the samples met the viscosity standards for stereolithography applications.

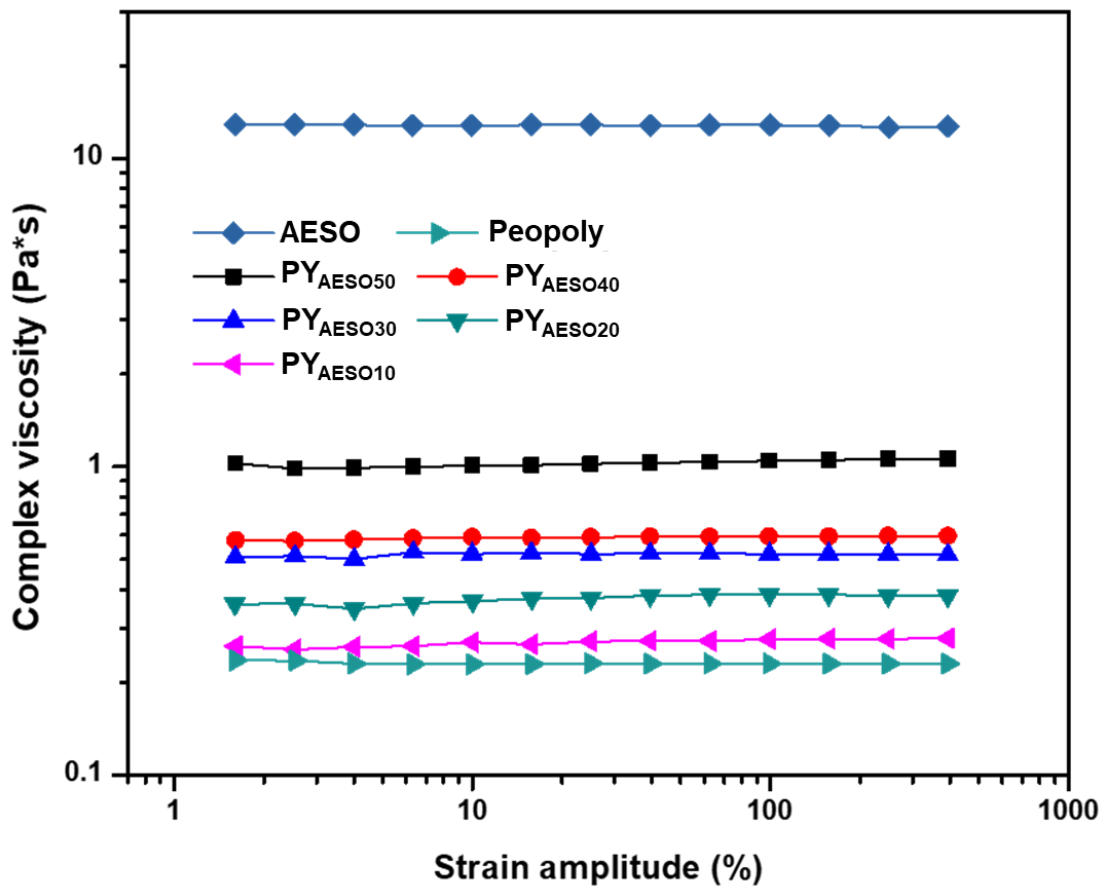


Figure 25: PY resin viscosity variation with increasing AESO loads (viscosity curves of pure PY and AESO are also included).

4.3.3 Mechanical properties

Having good mechanical behavior is essential for biobased resins to compete with standard petroleum-based commercial resins.^[169] The molecular characteristics of the biomaterial have a strong influence on its mechanical behavior.^[134,170] According to **Figure 26**, the average tensile strength of commercial resins is around 44 MPa (unlike the Peopoly resin standard, where the average tensile strength is about 50.3 MPa). The presence of 10 wt.% of AESO decreased the tensile strength by approximately 50%, becoming 25 MPa (**Figure 27**). The tensile strength continued to drop as the AESO content in the mixture increased, resulting in a 70.8% decrease with 50 wt.% of AESO. This decrease in the tensile strength can be caused by the network

loosening of plant-based resins.^[135,171] Nevertheless, the PY systems containing 10, 20 and 30 wt.% of AESO showed mechanical performances similar to other petroleum-based resins, such as the Anycubic Standard.

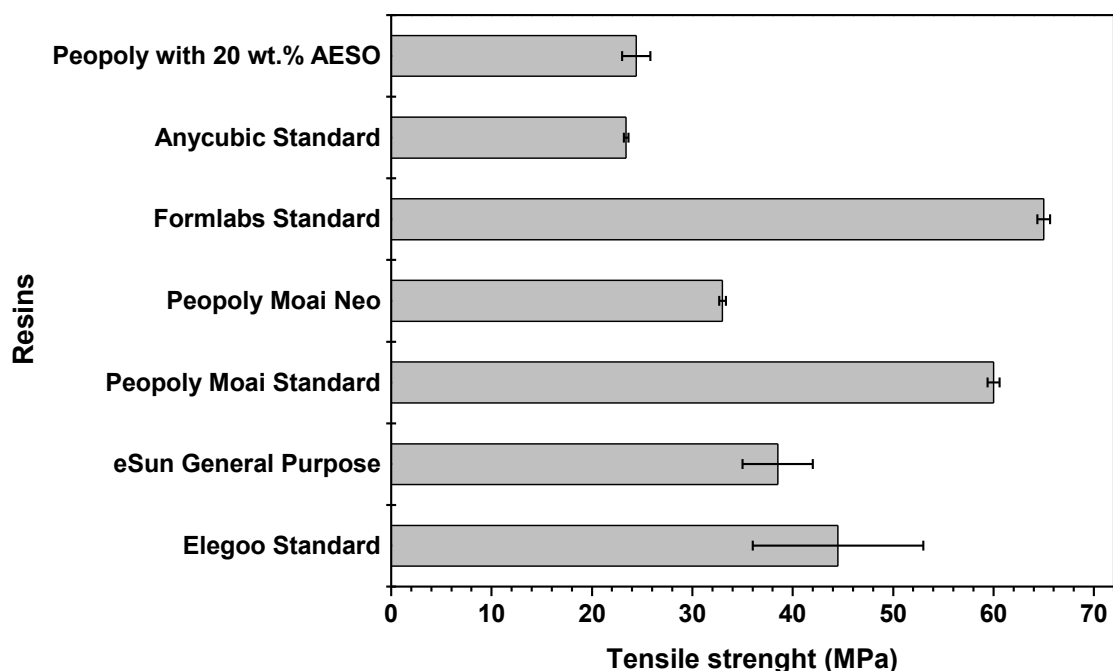


Figure 26: Tensile strength comparison between Peopoly moai standard with 20 wt.% AESO and different types of commercial resins.

The elongation at break is directly related to the material ductility. High ductility allows the structures to bend and deform to some extent without cracking.^[172] The elongation at the break of the PY increased as the AESO load increased, as shown in **Figure 27**. The maximum elongation at break of neat Peopoly resin is 2.3%. It increased to 2.9 and 4.8% (108% higher than pure PY) when 10 and 50 wt.% of AESO was mixed, respectively. Cui et al.^[135] observed similar behavior when 20 wt.% of urethane epoxidized soybean oil was incorporated into the resin system, which increased the elongation by approximately 13%.^[135] The improvement of flexibility and elongation at break with the addition of AESO is in accordance with the findings by Zhang et al.^[173], where it was assigned to the presence of the free fatty acid chains from the soybean oil, which act as plasticizers.^[173]

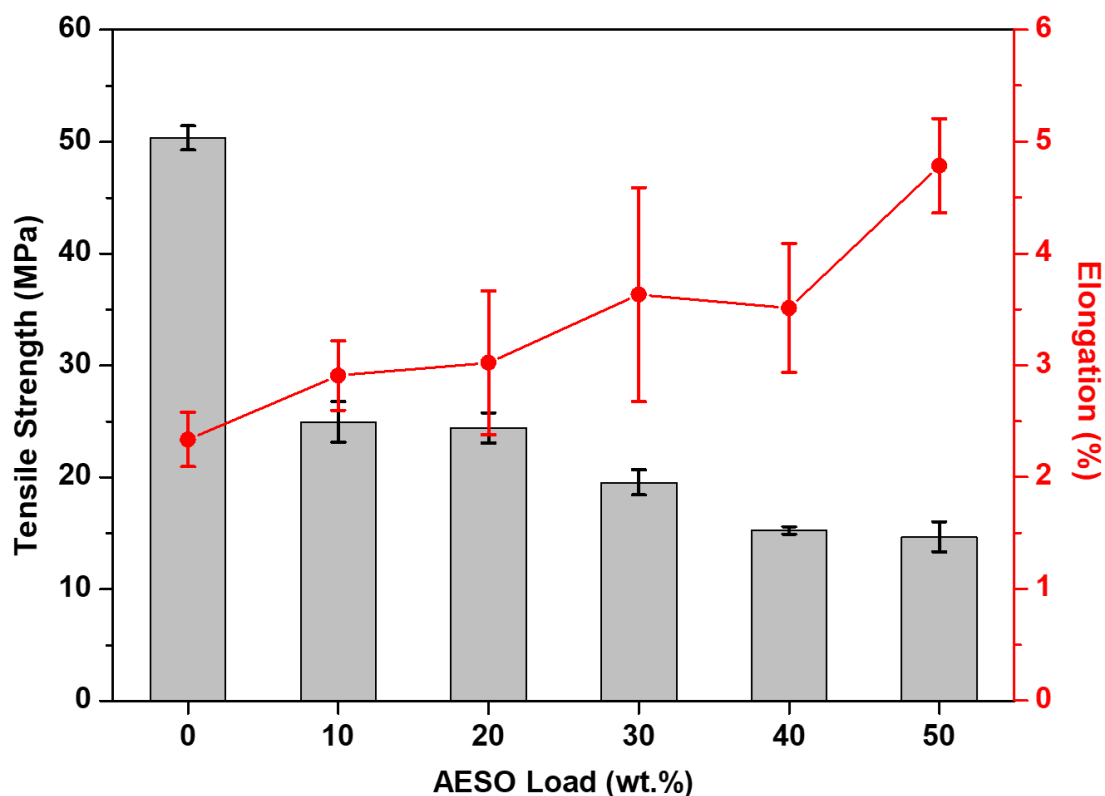


Figure 27: Variation of the tensile strength (gray bars) and elongation (red squares) as a function of AESO loadings. Statistical analysis for the elongation at break was done using a one-way analysis of variance (ANOVA) with the level of significance set at $p < 0.05$.

The fracture energy, which is the area under a stress-strain curve, is known to have a direct relationship with the material toughness.^[174] In materials with high crosslinking density, toughness tends to decrease.^[85] PY toughness decreased by 19.4% with the incorporation of 10 wt.% of AESO (**Figure 28**). However, further increasing the AESO content did not affect this parameter.

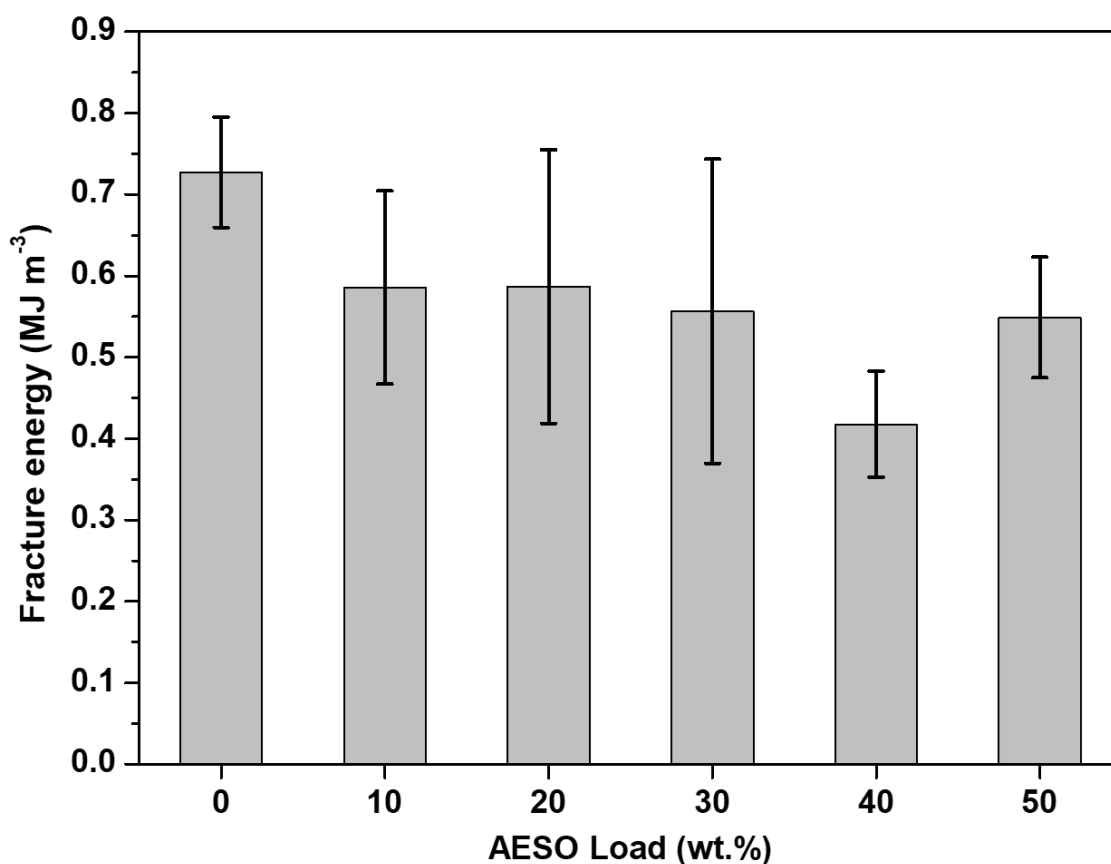


Figure 28: Fracture energy for 3D-printed samples with different AESO loadings.

On the other hand, Young's modulus, as shown in **Figure 29**, was negatively impacted by the incorporation of AESO dropping down from 2.15 to 0.55 GPa (74.4% decrease) when 50 wt.% of AESO was incorporated. The cause for its decrease is similar to the tensile strength, with is due to the network loosening of the polymer structure.

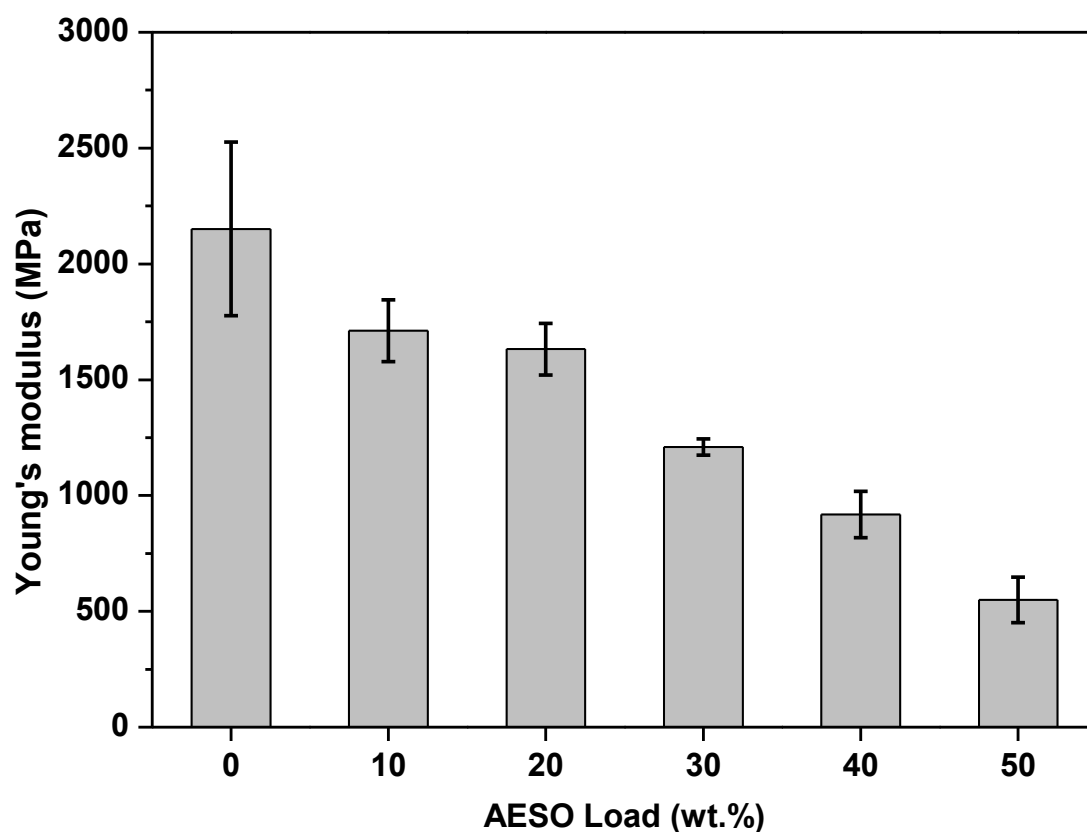


Figure 29: Variation of the Young's modulus with increasing concentrations of AESO.

4.3.4 Thermogravimetric analyses

Thermogravimetric analyses were performed in order to assess the thermal and thermo-oxidative stability of the different UV-cured systems. **Table 6** collects the obtained data.

Table 6: Thermogravimetric data for the different UV-cured systems.

Sample code	Atmosphere	T _{5%} [°C]	T _{max1} ^a [°C]	Residue at T _{max1} [%]	T _{max2} ^a [°C]	Residue at T _{max2} [%]	Residue at 700 °C [%]
PY	nitrogen	316	429	41	-	-	5.1
PY _{AESO10}		318	432	39	-	-	4.7
PY _{AESO20}		300	433	37	-	-	3.8

CHAPTER 4 – PHOTSENSITIVE ACRYLATES CONTAINING BIOBASED EPOXY-ACRYLATE
SOYBEAN OIL

PY _{AESO30}		308	429	40	-	-	3.3
PY _{AESO40}		311	432	38	-	-	3.0
PY _{AESO50}		280	426	40	-	-	1.3
AESO		308	390	59	-	-	2.7
PY		311	421	51	555	8.8	0
PY _{AESO10}		320	428	45	554	8.1	0
PY _{AESO20}		305	428	47	551	7.8	0
PY _{AESO30}		307	427	48	543	7.4	0
PY _{AESO40}	air	303	425	49	555	7.2	0
PY _{AESO50}		291	423	49	551	6.8	0
AESO		293	397	54	552	5.7	0

^aFrom derivative curves.

The obtained data seem to indicate a very limited effect provided by the introduction of increasing amounts of the bio-based resin in PY: in fact, regardless of the composition of the UV-cured products, the changes of $T_{5\%}$, $T_{\max1}$ and $T_{\max2}$ values are very limited. Besides, it is worth noticing a slightly higher charring effect provided by PY with respect to AESO, with a monotonic decrease of the residues in nitrogen at the end of the TGA tests, increasing the AESO content.

4.3.5 Effect of AESO on PY wettability

Hydrophilicity is known to be directly correlated with the ability to promote cell adhesion and proliferation, which are important factors for biocompatible materials.^[175,176] In order to verify the influence of AESO addition on the wettability of printed samples, static contact angle (CA) measurements were performed. As shown in **Figure 30**, neat PY and AESO printed resins have a contact angle of $72.2^\circ \pm 3.8^\circ$ and $92^\circ \pm 1.6^\circ$, respectively. The higher AESO hydrophobicity

could be attributed to its long non-polar fatty acid chains. Furthermore, the PY_{AESO} samples contact angle increased as more AESO was added in the mixture.

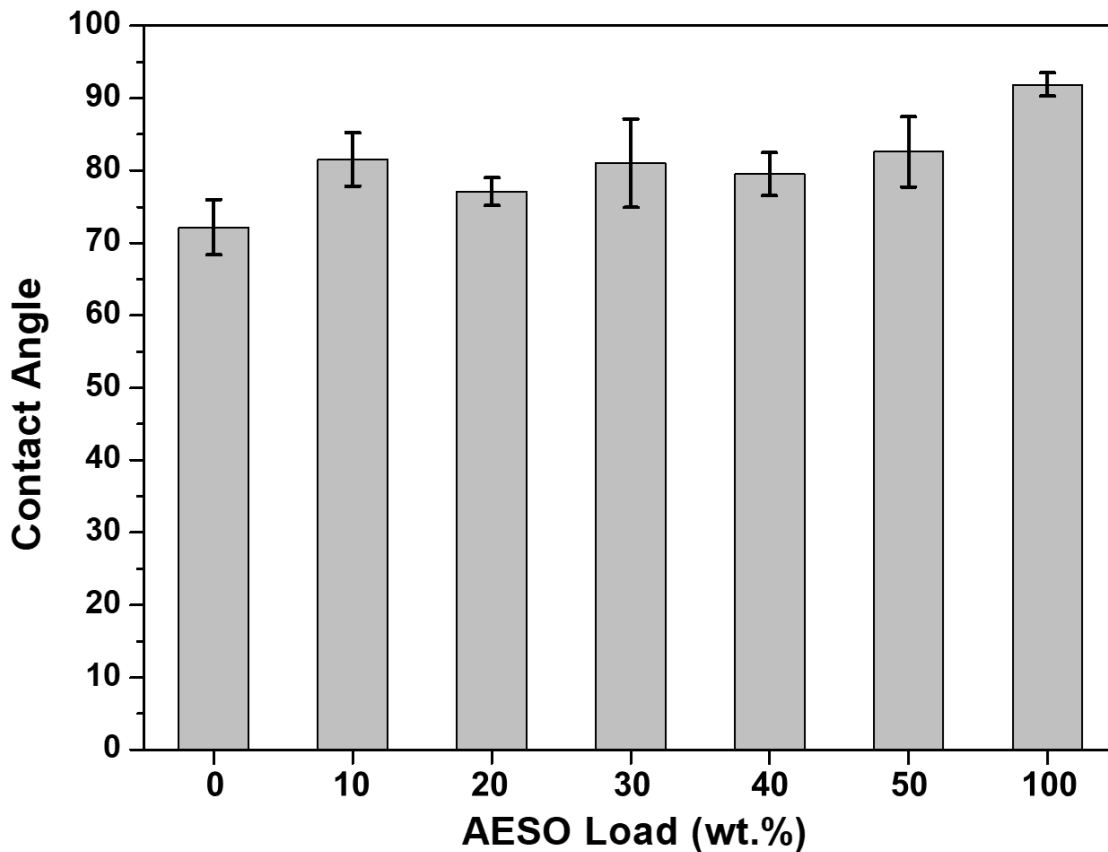


Figure 30: Water contact angle measurements of 3D-printed samples with different AESO loadings. Statistical analysis for the contact angle was carried out using a one-way analysis of variance (ANOVA) with the level of significance set at probabilities of $p < 0.05$.

4.3.6 Swelling properties

Swelling is defined as an increment in the volume of a solid or gel when in contact with a gas or liquid.^[177] The change in volume can lead to various deformation on the swollen material, such as wrinkles and surface breaks, which is crucial to avoid when structural applications are considered.^[178]

Two factors are known to influence the swelling properties of polymers, the crosslinking density and hydrophilicity.^[179] Polymers with high crosslinking density have shown to absorb less water, due to a highly entangled chain structure, which prevents water to enter.^[151] On the other hand, material with high hydrophilicity are known to absorb water more easily.^[179] The AESO and PY mixture is a good example of how these two properties can influence the swelling behavior of the parts.

As shown in **Figure 31**, the addition of AESO in the PY resin promoted an overall increase of the water intake of obtained PY_{AESO} UV-cured mixtures. The incorporation of 10 wt.% of AESO into the PY resin increased the swelling from 0.13% to 1.4% and 2.2% after 5 and 30 days, respectively. When 50 wt.% of AESO was added, the swelling increased only by 1.0% and 1.2%, respectively, during the same period of time. Nevertheless, all PY_{AESO} mixtures showed higher swelling than pure PY.

There are different possibilities to explain this behavior. (1) although AESO is considered hydrophobic, due to its long carboxylic chains, according to Liu et al.^[180] it also contains polar groups in its structure from the triglyceride part of the molecule (hydroxy and epoxy groups), which are responsible for the inherent water absorption capability.^[180] (2) at lower AESO% the photopolymerization reaction between AESO and PY could have occurred at different rates, where there was the formation of two separate polymeric structures. Thus, gaps could have been formed in between these structures, creating spaces in which water could enter. As the concentration of AESO increased, the PY-AESO polymeric structure could have become more organized, reducing the gaps with in it. (3) The higher swelling of the PY_{AESO} mixtures could be due to the network loosening of its polymer structure.

Figure 31 also demonstrated that all PY_{AESO} UV-cured mixtures showed swelling stability after 20 days in water; besides, pure UV-cured PY and AESO had the higher swelling rates (about 686% and 81%, respectively, during the 30 days period). Finally, all the tested samples showed mechanical integrity during 21 days of immersion in water. However, after 30 days, the mixtures containing 40 and 50 wt.% of AESO started to degrade inside the water. The

degradation is attributed to the natural biodegradability of AESO and is in agreement to the results reported by Yu et al. [130]

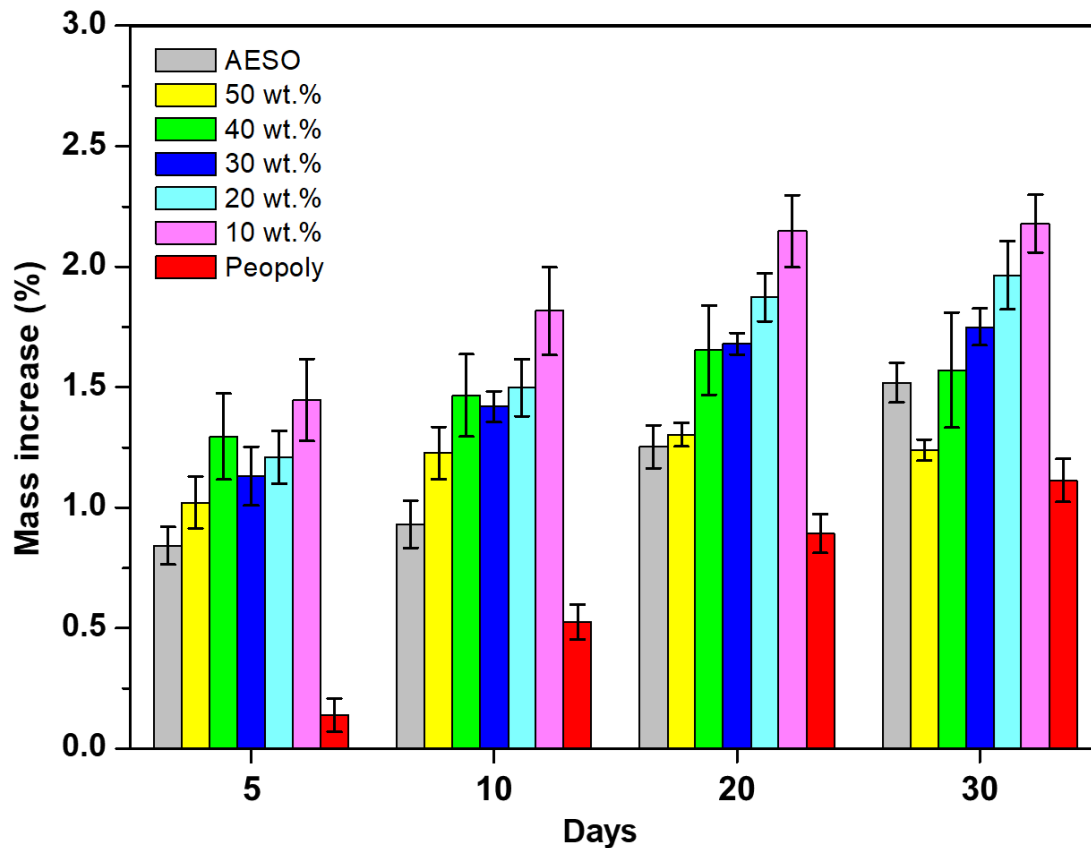


Figure 31: Swelling behavior of 3D-printed parts with different AESO loadings, after 5, 10, 20 and 30 days of immersion in water.

4.3.7 AESO load effect on working curve

During the development of a photosensitive resin, it is important to know the correct amount of light or time needed to perform the curing. Models containing many empty spaces in their structure, being overexposed during the printing process, can result in these spaces being cured as well. On the other hand, if the resin is underexposed, smaller structures could show deformations or fail to be printed.^[181] A good rule of thumb is that the SLA resin should exhibit low values of E_c and high values of D_p , as it will need lower energy doses and the radiation will

penetrate deeper in the resin.^[182] The working curve parameters (D_p and E_c) for the Peopoly standard and other commercial resins, are shown in **Table 7**.

Table 7: Depth penetration (D_p) and critical energy (E_c) for different commercial resins.

Resin name	Manufacturer	E_c (mJ mm ⁻²)	D_p (mm)
PR48*	Autodesk	0.63	0.053
VeroWhitePlus*	Stratasys	0.19	0.145
Formlabs Clear*	Formlabs	1.26	0.192
TangoBlackPlus*	Stratasys	0.41	0.151
VeroClear*	Stratasys	0.69	0.568
PY _{neat}	Peopoly	1.49	0.75

*Values from Joe Bennett, 2017 ^[154]

Both neat AESO and PY showed similar E_c and D_p , with AESO having a slighter higher D_p (**Table 8**). The addition of AESO did not result in any considerable variation of both properties, where the depth penetration increased according to its concentration (**Figure 32**).

Table 8: Depth penetration (D_p) and critical energy (E_c) calculated as a function of AESO loadings.

Sample code	Loading (wt.%)	E_c (mJ mm ⁻²)	D_p (mm)
AESO _{neat}	-	1.44	0.88
PY _{AESO10}	10	1.48	0.71
PY _{AESO20}	20	1.48	0.78
PY _{AESO30}	30	1.45	0.79
PY _{AESO40}	40	1.47	0.80
PY _{AESO50}	50	1.46	0.81

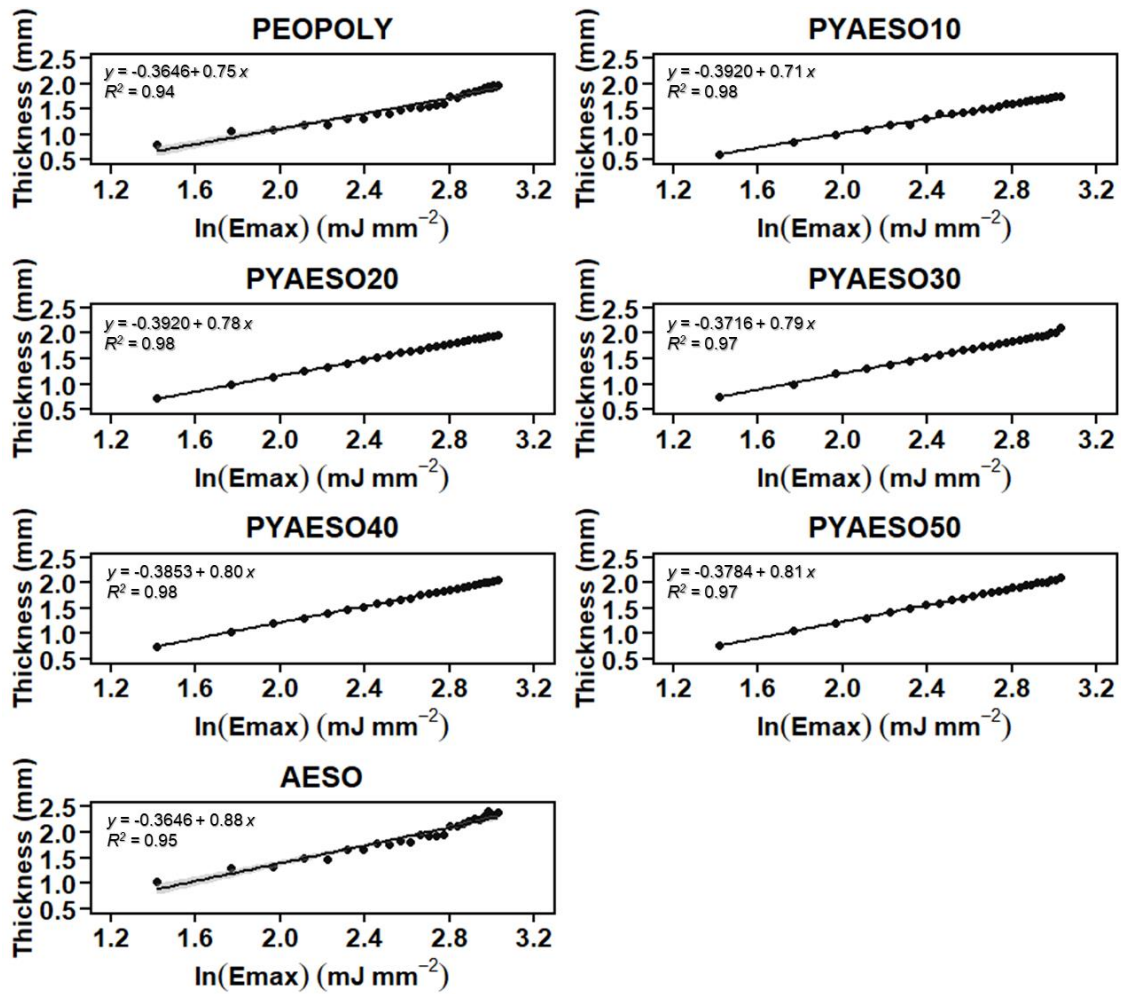


Figure 32: Working curve for Peopoly Clear, AESO and their mixtures.

4.3.8 Visual evaluation

Visual tests were carried out to compare the printing quality of mixtures containing AESO with Peopoly standard. The liquid resin did not show phase separation (or sedimentation) phenomena before being used to print the prototypes. As shown in **Figure 33**, three boat prototypes (3DBenchy) were printed with 0, 10, and 50 wt.% of AESO (samples A, B and C, respectively). The yellowish color observed for samples B and C is derived from the AESO, which naturally has a yellow color, as reported by Miao et al.^[147] and Kasetaitė et al.^[183] and it is not related to the post curing process.^[147,183] Moreover, close visual inspection of the printed samples

(Figures 33A*, 33B* and 33C*) demonstrated good printing quality and smooth surfaces, which are worthy indications for commercial suitability.

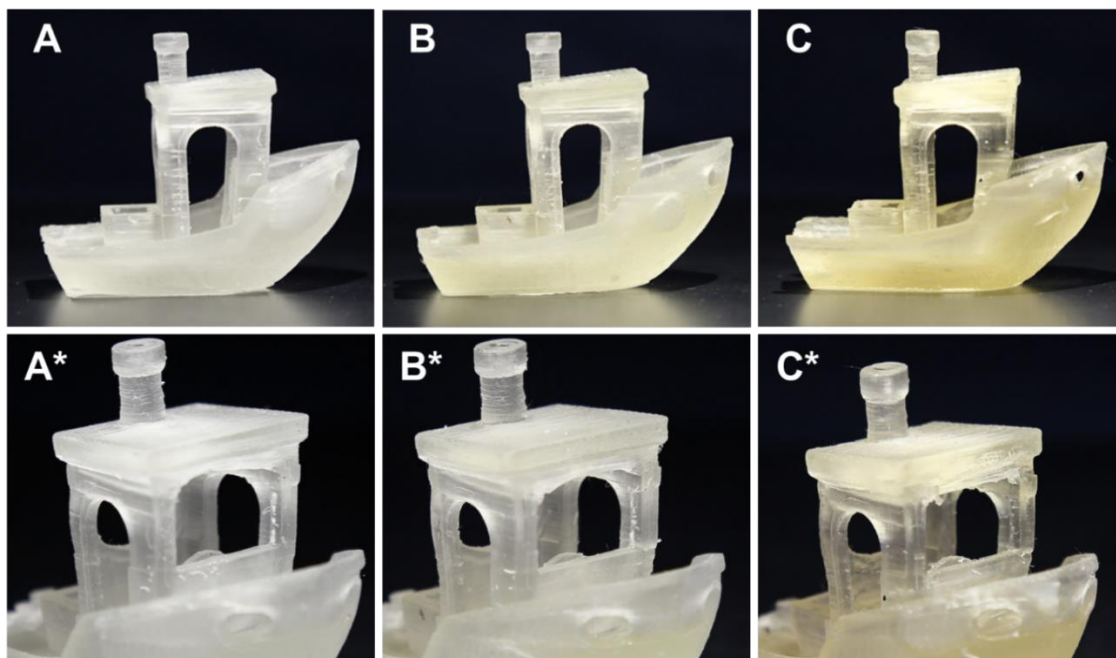


Figure 33: Digital images of the boat prototypes (48 x 24.8 x 38.4 mm) printed with different AESO concentrations. Boat A was printed with pure Peopoly resin and boats B and C with 10 and 50 wt.% of AESO mixed in it. The images A*, B* and C* are close-ups of their respective counterparts.

4.4 CONCLUSIONS

This study demonstrated the feasibility of combining epoxy-acrylate soybean oil with a standard resin used for 3D printing applications. The AESO content ranged from 10 to 50 wt.% and the FT-IR investigation demonstrated that the photoinitiator present in the resin was enough to drive the UV-curing process. Besides, as assessed by rheological analyses, the presence of up to 50 wt.% of AESO in the formulations allowed maintaining the viscosities in a range suitable for SLA 3D printing. The addition of 50 wt.% of AESO into the PY resin resulted in a decrease in both tensile strength and Young's modulus by 70.9 and 74.4%, respectively, due to network

loosening. Nevertheless, the tensile strength loss was compensated with an improvement of the elongation at break: this latter was increased by 108% when 50 wt.% AESO was added to PY. Additionally, the mixtures containing 10, 20 and 30 wt.% of AESO showed mechanical properties similar to other commercial resins (with clear improvements in flexibility).

Visual assessment of the samples highlighted that the PY-AESO formulations were suitable for 3D printing complex structures, hence indicating that the epoxy-acrylate soybean oil could partially replace petroleum-based resins without affecting the printability. The incorporation of AESO into the Peopoly resin did not show any remarkable effect on either the thermal or thermo-oxidative stability of the UV-cured products. Among all the investigated formulations, 30 wt.% AESO loading was found to be the most promising, as it exhibited mechanical properties similar to fossil-based commercial resins. Further analyses and experiments have to be performed to increase the “bio” content in the fossil-based formulation, to optimize the mechanical properties, as well as to deeply study the resin biodegradability and biocompatibility. However, the proposed approach seems to be an effective starting point toward the development of environmentally friendly materials.

CHAPTER 5

SYNTHESIS OF A BIOBASED RESIN FOR MULTIPURPOSE APPLICATIONS

In this chapter, the complete development of a biobased resin for vat polymerization is reported. The resin was produced using the results from the previous chapter (Chapter 4). Here epoxy-acrylate soybean oil (AESO) was combined with isobornyl methacrylate (IBOMA), a photosensitive diluent derived from tree saps, to produce a resin for multipurpose applications. Before the description of the experimental part and discussion of the main results, a short introduction about the materials used for biobased resins is presented. Materials, general methods, and instrumentation for characterization were reported in the Chapter 3.

5.1 INTRODUCTION

The advent of complete synthetic plastic was one of the most important 20th century discoveries. It revolutionized various industrial sectors, such as food packaging, clothing, biomedical devices, and electronics, since the material was cheap, durable, moldable, transparent, and lightweight. Its impact was so deep that nowadays it is impossible to imagine a world without it.^[184]

However, its durability and chemical stability has proven to be a double-edge sword: it is nearly impossible to microorganisms present in nature to degrade plastic. Because of that, plastic tends to accumulate on the environments, where it slowly breaks down into smaller particles (micro- or nano- scale). Indeed, the environmental pollution caused by plastic is so great that its management is one of the grand challenges of the 21st century.^[184]

The need of substituting plastic has led many sectors to invest in biobased and (bio)degradable polymers (**Figure 34**). According to the European Bioplastic report, in 2021 the global production of bioplastic was 2.42 million tons, where biobased polymers accounted to nearly 36% of it while (bio)degradable polymers the rest 64%. Furthermore, the same report discusses that as investments on production increases by 2026 the global production of bioplastic will increase by 214%, reaching 7.59 million tons.^[185]

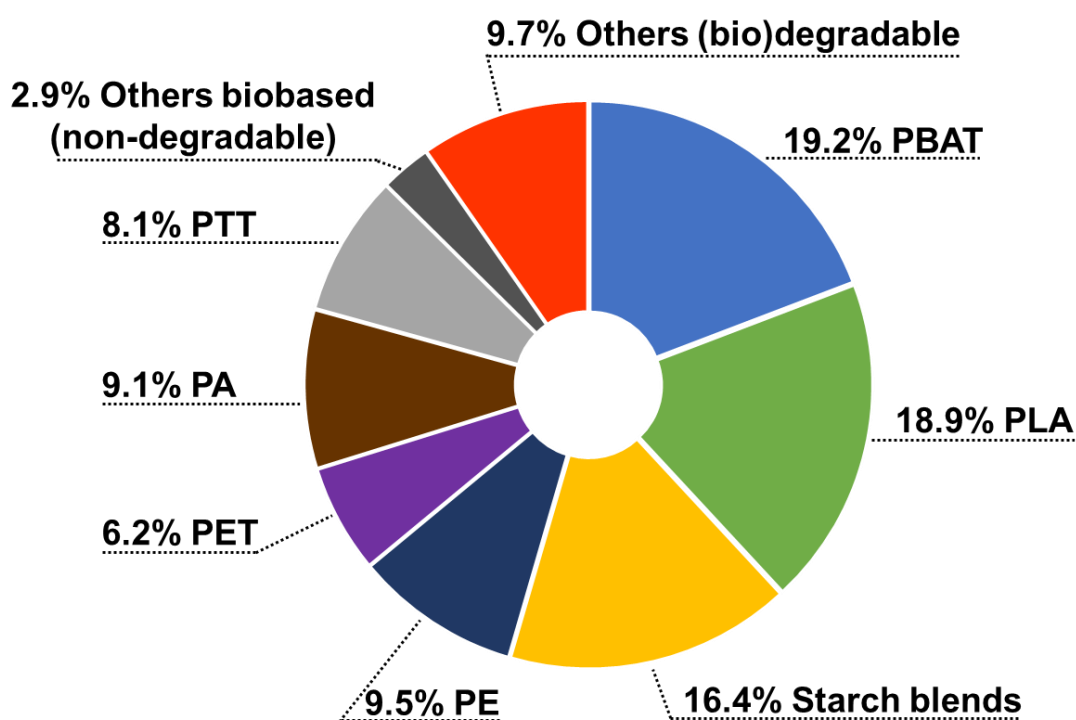


Figure 34: 2021 global production of bioplastics. Data retrieved from European Bioplastic.^[185]

In additive manufacturing, more specifically for vat photopolymerization, there has been a rise in the number of researches proposing new types of bio-based resins.^[116] These resins are synthesized from a wide range of materials, such as vanillin,^[113] epoxidized linseed oil,^[110]

methacrylic lignin,^[112] bio polyester,^[186] epoxidized acrylate soybean oil,^[134] and more. The latter, AESO, has shown to be a notable material. It is derived from soybean oil, which makes it cheap to fabricate, and is available worldwide. Lebedevaite et al. (2020) investigated the usage of AESO as a base component for the fabrication of an all-purpose 3D printing resin. For that they combined AESO with various biobased reactive diluents. The biorenewable carbon content of the resins were estimated to be between 75-82% and the printed parts showed good tensile strength and elongation at break.^[81]

Even though there has been a lot of investment and research on the development of biobased resins, only a few of them were able to demonstrate properties similar to petroleum-based resins.^[135] Therefore this work had the objective to explore new combinations of biobased and plant-based resins and to expand the limited number of high performance biobased resins by developing a resin with tunable mechanical and physical properties.

5.2 EXPERIMENTAL PART

5.2.1 Photocurable resin formulation

The photocurable resins were prepared following a similar process of previous discussed (Chapter 4). First, in a lightproof beaker, varying amounts of AESO (ranging from 50 to 90 wt.%) were mixed with IBOMA. Then, 2 wt.% TPO was added to the mixtures, that were ultrasonicated for 10 min at room temperature to dissolve the photo-initiator. Next, the mixtures were stirred for 30 min and let rest for 1h to allow the bubbles to disappear. During the entire synthesis procedure, the light was kept on minimum to avoid exposing the mixtures to light. It was observed that as the concentration of IBOMA increased the mixture became more transparent.

The bio content (*BC*) of each *AESO/IBOMA* mixture is shown in **Table 9** and was calculated according to **Equation 31**.

$$BC = w_i \times BRC_i + w_j \times BRC_j \quad (\text{Eq. 31})$$

where w is the mass fraction, i and j are the resin type, and bio-renewable carbon (BRC) is the ratio of bio-sourced carbon to the sum of bio- and fossil-based carbons.

Table 9: Sample code, composition, and bio-content (BC) of each *PEGDA/AESO* mixture.

Sample Code	IBOMA (%)	AESO (%)	BC (%)
IBOMA	100	-	71
I.A. 50:50	50	50	78.5
I.A. 40:60	40	60	80.0
I.A. 30:70	30	70	81.5
I.A. 20:80	20	80	83.0
I.A. 10:90	10	90	84.5
AESO	-	100	86

5.3 RESULTS AND DISCUSSION

5.3.1 FT-IR Analysis

To asset that the photopolymerization process of IBOMA, AESO and their mixtures were successful, FT-IR spectra of uncured resins and 3D printed specimens was performed. As shown by **Figure 35**, the photopolymerization reaction was verified by monitoring the peaks at 1636, 1618, 1410 and 810 cm^{-1} , assigned to the stretching vibrations of the C=C double bonds, and the peaks at 1270, 1190, and 985 cm^{-1} , assigned to IBOMA's ester groups (C-O bonds).^[133,163,167,187–189] After the UV curing process, it is possible to observe that the peaks related to the C=C double bonds had a considerable reduction. This indicates that the radical molecules, produced by the photoinitiator, opened the monomers double bounds, allowing to chain growth and crosslinking

reactions to take place. This becomes more evident in the case of AESO, where its branched structure, capable of producing various radical groups, resulted in an almost complete disappearance of the unsaturated C=C bonds during crosslinking. Furthermore, it is possible to observe a shift of the 1190 cm^{-1} peak, which is attributed to a positional change of IBOMA and AESO ester groups when C-C structures were formed.

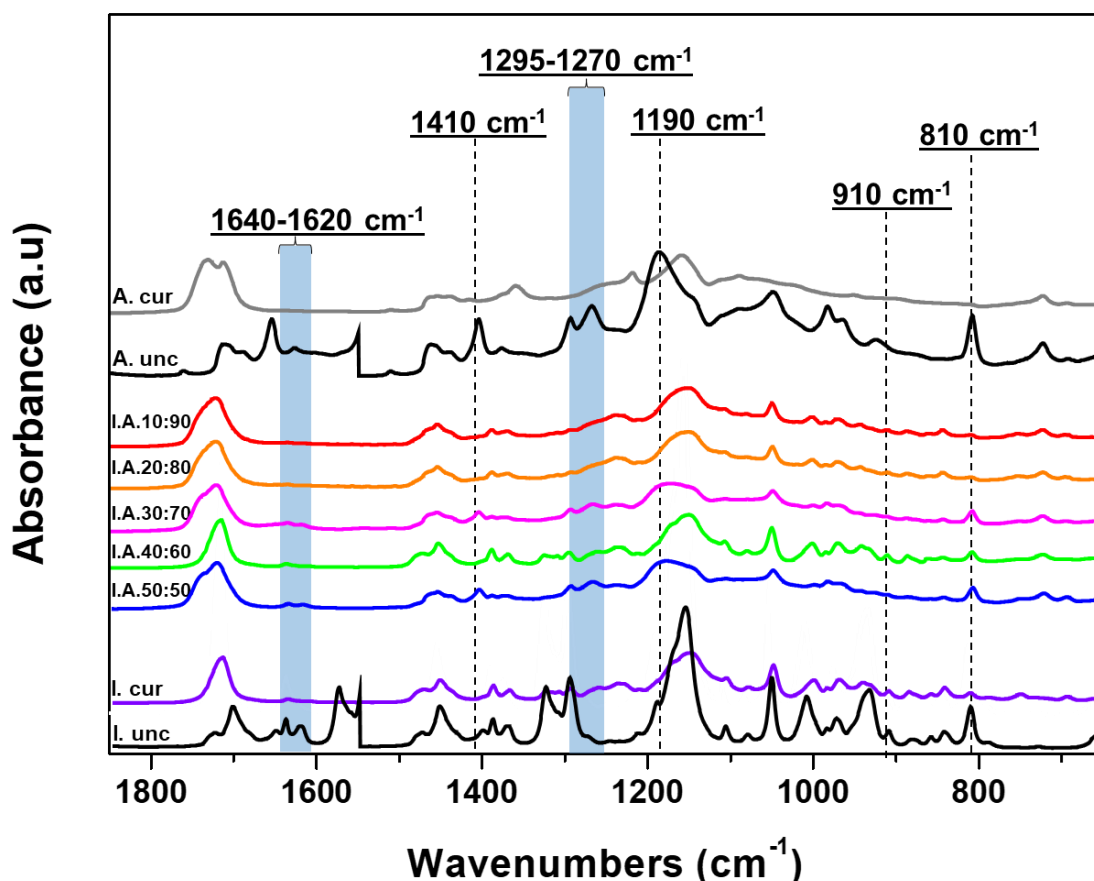


Figure 35: ATR-FTIR spectra of AESO, IBOMA and their combinations. Samples I_{unc} and A_{unc} are relative to the uncured IBOMA and AESO resin, respectively. The other samples were post-cured under UV-light for 40 min (20min each side).

Another method to verify the efficacy of the photopolymerization reaction, is by calculating the difference between the area under the curve of the uncured and cured samples, as demonstrated in **Table 10**. The IBOMA/AESO mixtures showed an acrylic and vinyl conversion superior to 80%, showing that the catalyst was efficient on initiating the reaction. On the other

hand, the addition of IBOMA decreased the AESO epoxy groups conversion, from 81.17% (pure AESO) to the lowest value of 62.22% (when 50 wt.% was added). In order to improve the epoxy conversion, a cationic catalyst, such as bisphenol A diglycidyl ether (DGEBA), should be added to the formulation.

Table 10: Double-bond conversion at 810, 910 and 1620-1640 cm^{-1} for IBOMA, AESO, and their mixtures.

Sample code	Peak at 810 cm^{-1}			Peak at 910 cm^{-1}			Peaks at 1620-1640 cm^{-1}		
	Initial area (cm^2)	Final area (cm^2)	Conversion (%)	Initial area (cm^2)	Final area (cm^2)	Conversion (%)	Initial area (cm^2)	Final area (cm^2)	Conversion (%)
IBOMA	0.3889	0.0444	88.58	-	-	-	0.4675	0.0200	95.72
I.A. 50:50	0.4289	0.0372	91.33	0.1882	0.0711	62.22	0.3603	0.0290	91.95
I.A. 40:60	0.4132	0.0602	85.43	0.1538	0.0430	72.04	0.3918	0.0200	94.90
I.A. 30:70	0.4107	0.0871	78.79	0.1848	0.0585	68.34	0.4161	0.0649	84.40
I.A. 20:80	0.3933	0.0675	82.84	0.1705	0.0400	76.54	0.4083	0.0200	95.10
I.A. 10:90	0.4550	0.0888	80.48	0.1779	0.0559	68.58	0.4304	0.0376	91.26
AESO	0.4613	0.0359	92.22	0.6468	0.1218	81.17	0.3284	0.0210	93.61

5.3.2 Rheology

The viscosity plays a fundamental role when a photosensitive resin is being developed for 3D-printing. Especially for commercial applications, where the resin needs to be compatible with as many different machines as possible. A good rule of thumb is that the viscosity cannot be superior to 3 Pa s, since higher values tends to result in failures or damages in the VAT. The viscosity of pure IBOMA is 0.004 Pa s, while pure AESO showed a viscosity of 12.9 Pa s (**Figure 36**). When IBOMA was added to AESO, the viscosity of the mixture decreased according to the IBOMA concentration. When 10 wt.% and 50% of IBOMA were added, the viscosity decreased by 58.9% (from 12.9 to 5.3) 98.4% (from 12.9 to 0.21), respectively. The mixture containing 90 wt.% of AESO was too viscous for the machine to print under room temperature. Therefore, the minimal concentration of IBOMA needed to perform the 3D-printing process was set as 20 wt.%.

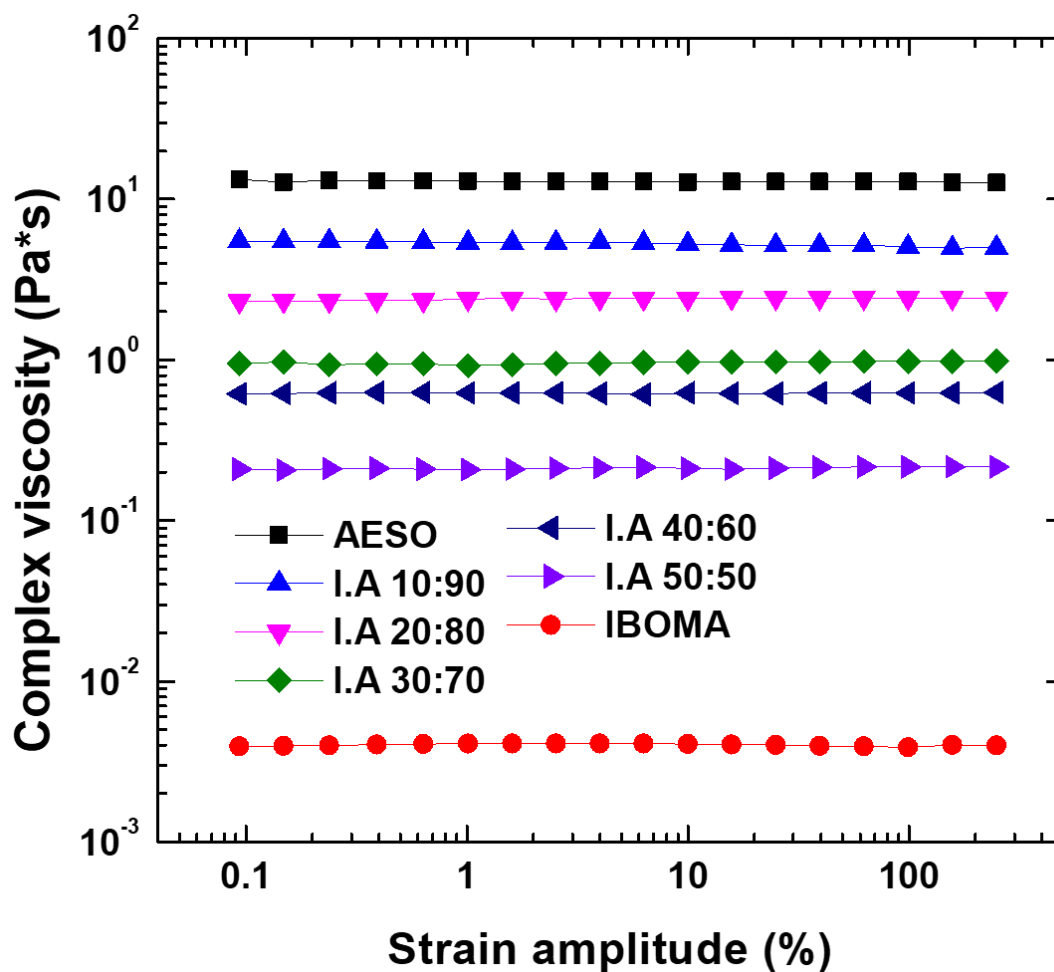


Figure 36: Viscosity variation with increasing AESO concentration.

5.3.3 Mechanical properties

As discussed on the previous chapter, nowadays there are a variety of commercial resins, each one having different mechanical properties. Usually, for domestic or multipurpose applications, the manufacture design a “standard” resin that needs to have a well-defined tensile strength and elongation at break. As previous reported, the tensile strength and elongation at break of neat AESO is approximately 4.8 MPa and 7.16%, respectively, which is very low comparable to commercial resins.^[149] When IBOMA was mixed with AESO, the tensile strength increased drastically, going from 4.8 to 10.5 (a 118.75% increase) with 10 wt.% and to 37.2 (a 675% increase) with 50% (Figure 37).

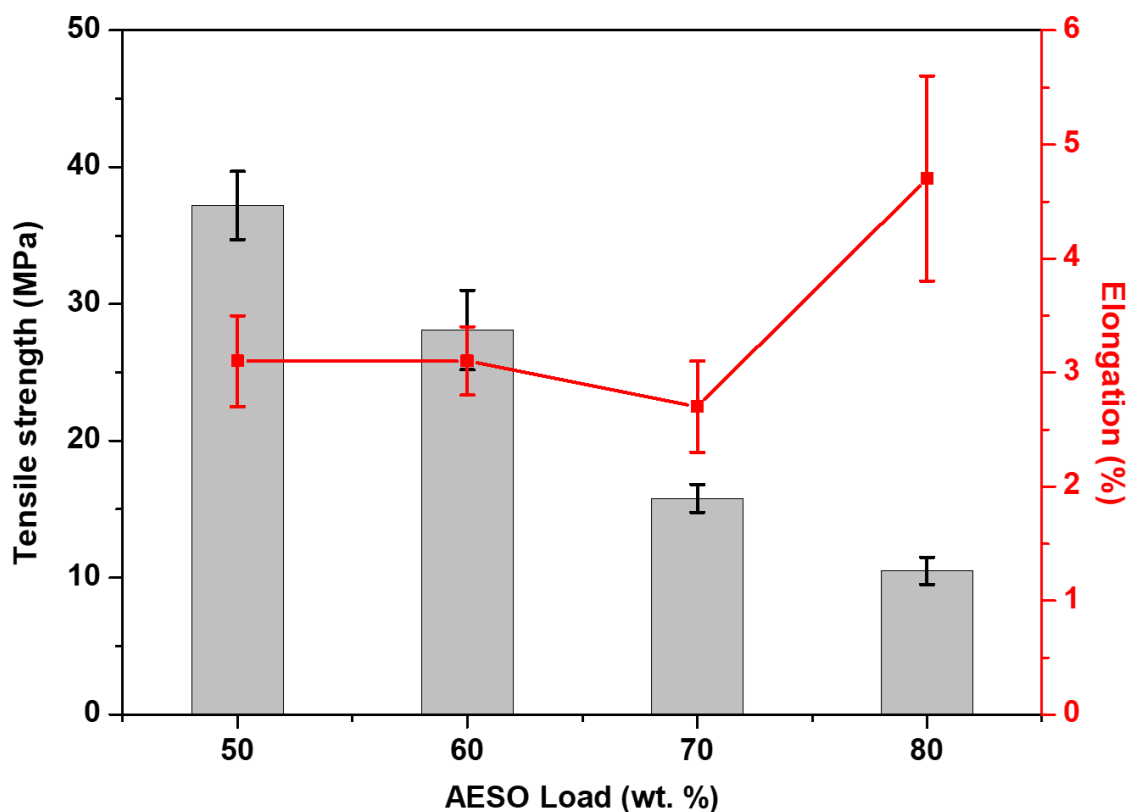


Figure 37: Samples tensile strength and elongation variation as a function of AESO loads.

However, as the concentration of IBOMA increased the mixtures elongation at break decreased, reaching 3.1 with 50 wt.%. Its reduction could be attributed to three factors: (1) the formation of shorter polymeric chains, (2) low crosslink density, or (3) the presence of uncured liquid resin trapped inside the samples, in which according to Cingesar et al. 2022, would lower the crosslinking density of the object, making it easier to break.^[190] However, since the samples were post cured for 40 min after the print was over, it is safe to say that no liquid resin remained trapped inside, thus the elongation reduction is related to possibilities (1) and (2).

The chemical structure of IBOMA is composed of short building blocks, which favors that the possibility (1) is the main cause. Indeed, Martins et al. 2021, had similar results when they tested the effect of adding different concentration of IBOMA in dental resins, where the samples with higher concentrations were also the ones with the lowest elongation.^[191]

Compared to some petroleum-based resins commonly used for 3D-printing, the AESO/IBOMA mixtures had similar values, especially the 50/50 wt.% combination. As shown in **Table 11**, the tensile strength and viscosity of the I.A.50:50 was in the range of most standard

resins. However, a significative difference was observed in the elongation at break and Young's modulus. The I.A.50:50 elongation at break was only 3.1%, being the lowest value of all, which restricts its use for manufacturing flexible parts. On the other hand, its Young's modulus was very high, close to the Formlabs grey. Nevertheless, the proposed formulation could be used to substitute some of the currently employed petroleum-based resins.

Table 11: Comparison of the mechanical behavior of I.A.50:50 with some common 3D-printing commercial resins.

Resin name	Tensile strength (MPa)	Elongation at break (%)	Young's modulus (GPa)	Viscosity (Pa s)
I.A.50:50	37.2	3.1	2.4	0.21
Anycubic standard	23.4	14.2	-	0.55
Formlabs draft	36	5	1.7	1.65
Formlabs grey	65	6	2.8	0.93
Peopoly neo	33	4.3	0.46	0.053
Peopoly deft	35	6	0.75	0.1
Elegoo standard	53	14.2	-	0.15
Siraya tech fast	33	6	0.8	0.1
Siraya tech simple	32	4	0.45	0.052

Other mechanical properties of AESO/IBOMA mixtures were also calculated from the stress-strain curve. The first one, fracture energy, is calculated from the area under a stress-strain curve and is related to a material toughness.^[174] Usually, toughness is inversely related to the polymer crosslinking density.^[85] In polymers with high density, such as AESO, toughness tends a decrease, where in low density polymers, it increases. As shown by **Figure 38**, the sample's fracture energy increased as the IBOMA concentration increased, where the highest value was when 50 wt.% of it was added. This can be ascribed to the rapid formation of linear structures by

IBOMA, trapping the radicals' groups and preventing the long AESO carboxylic chains to react and entangle one on another.

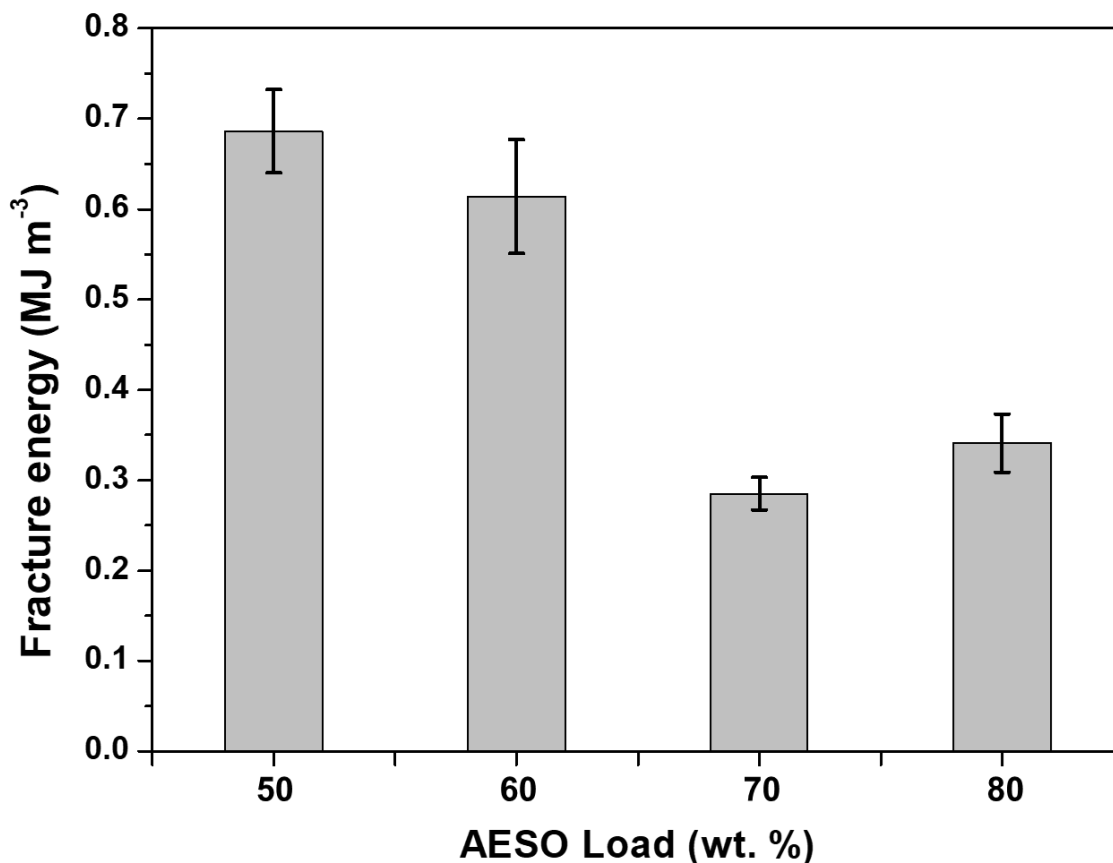


Figure 38: Fracture energy of the samples having different AESO concentration.

The second property that was calculated was the Young's modulus from the slope in the elastic region. This property measures the material ability to withstand changes in length when submitted to compression or lengthwise tension.^[192] As shown by **Figure 39**, the mixtures Young's modulus decreased as the AESO concentration increased. The reduction could be caused by network loosening, which is common when using vegetable-based resins.^[135,193]

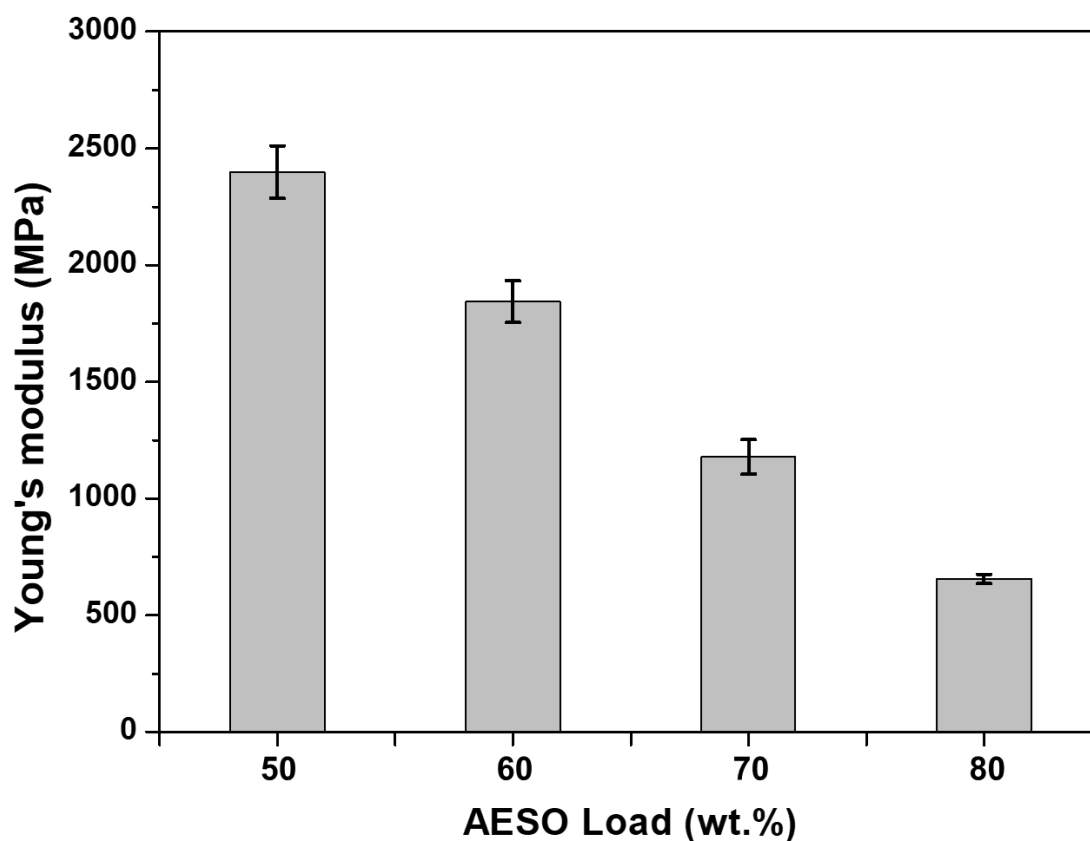


Figure 39: Young's modulus of the samples with varying loads of AESO.

5.3.4 Effects of the AESO concentration on contact angle

The most common method for determining a material's wettability is by measuring its contact angle. Neat AESO has a contact angle of $92^\circ \pm 1.6^\circ$, where its high hydrophobicity could be attributed to its long non-polar fatty acid chains.^[194] The addition of IBOMA did not demonstrate to have any significant impact on the mixtures wettability, only having a slight increase when 30 wt.% of it was added (**Figure 40**).

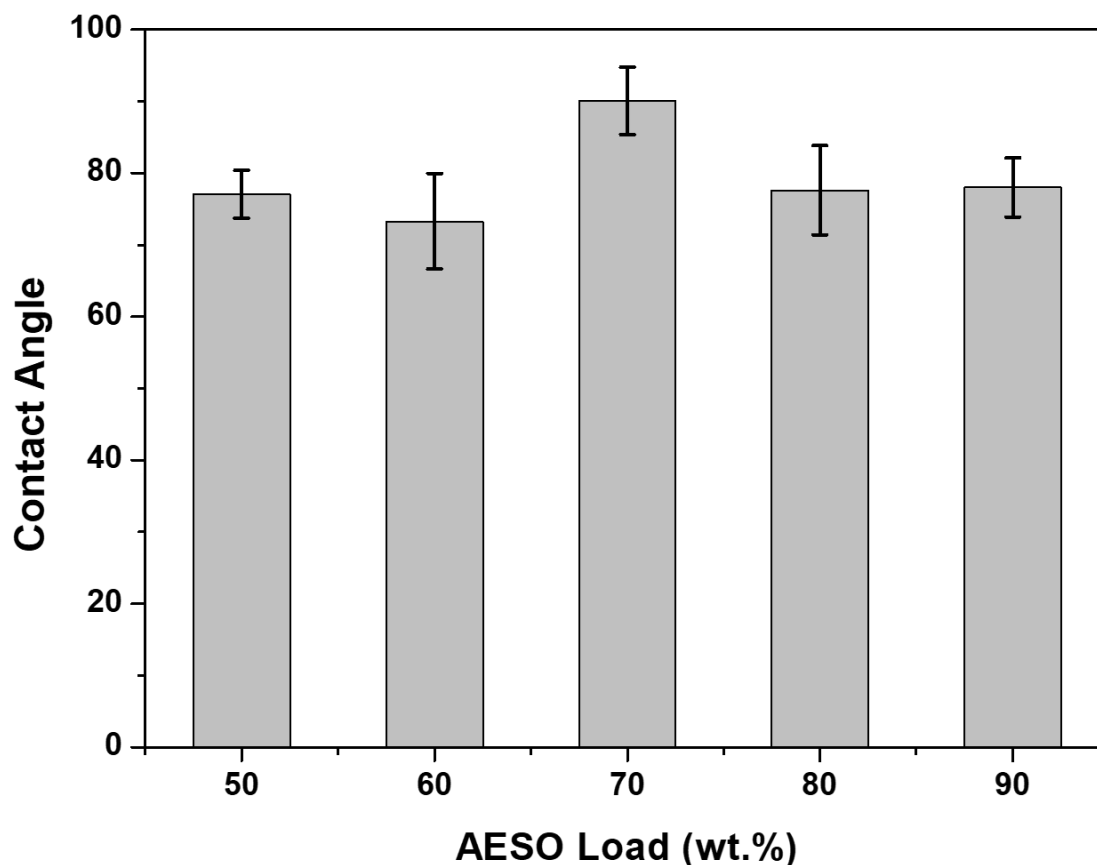


Figure 40: Change in the samples contact angle in relationship to the AESO weight percentage.

5.3.5 Thermogravimetric analyses

Thermogravimetric analyses were performed in order to assess the thermal and thermo-oxidative stability of the different UV-cured systems. **Table 12** presents the obtained data.

Table 12: Thermogravimetric data for the IBOMA and AESO mixtures.

Sample code	Atmosphere	T _{5%} [°C]	T _{max1} ^a [°C]	Residue at T _{max1} [%]	T _{max2} ^a [°C]	Residue at T _{max2} [%]	Residue at 700 °C [%]
IBOMA							
I.A. 50:50	nitrogen	272	394	34	-	-	0.7
I.A. 40:60		288	396	39	-	-	0.3
I.A. 30:70		278	395	41	-	-	1.0

I.A. 20:80	290	397	47	-	-	0.7
AESO	308	390	59	-	-	2.7
IBOMA						0
I.A. 50:50	259	408	28	543	2.9	0
I.A. 40:60	278	404	35	544	3.5	0
I.A. 30:70	^a 275	402	38	547	3.5	0
I.A. 20:80	278	400	45	542	4.8	0
AESO	293	397	54	552	5.7	0

^aFrom derivative curve.

The thermal and thermo-oxidative stability of the different systems does not seem to be affected by the composition, though the T_{onset} values, irrespective of the selected atmosphere, show a slight increase with increasing the AESO loading. In general, highly crosslinked polymer networks, typical in plant-based polymers, have a higher concentration of carboxylic double bonds (C=C), which, in turn, provides a higher thermal stability.^[169,195]

5.3.6 Working curve

When developing a photosensitive resin, it is important to know the correct amount of light or time needed to perform the curing. Models containing many empty spaces in their structure, being overexposed during the printing process, can result in these spaces being cured as well. On the other hand, if the resin is underexposed, smaller structures could show deformations or fail to be printed.^[181]

During the experiments, neat IBOMA did not print at higher scanning speeds, which had to be decreased from 80 mm/s and 200 mm/s to 30 mm/s and 60 mm/s, respectively in order the last squares to have variations in their heights. This is an indicative of low depth light penetration, which was indeed the case, since it had a value of 0.89 mm as shown in **Table 13**. On the other

hand, neat IBOMA demonstrated to have a very low E_c , meaning that it is very sensitive to light and requires less energy to photopolymerize.

One would expect by looking AESO E_c and D_p , (**Figure 41** and **Table 13**) that its addition would increase IBOMA's E_c and have no effect on its D_p . However, as the concentration of AESO increased, the mixture critical energy decreased and the depth penetration increased. The possible explanation for this behavior could be IBOMA's transparency, thus as its concentration increased more light entered the system. Moreover, its lower E_c decreased AESO required energy to start the photopolymerization reaction (behaving similar to a catalyst). Needing less energy to start the reaction means that more AESO's radical groups would be available to react with IBOMA, provoking a cascade reaction

Table 13: Depth penetration (D_p) and critical energy (E_c) calculated as a function of IBOMA and AESO ratios.

Sample code	Loading (wt. %)	E_c (mJ mm ⁻²)	D_p (mm)	R ²
IBOMA	-	0.17	0.89	0.93
I.A. 50:50	50	0.05	1.99	0.98
I.A. 40:60	60	0.13	1.32	0.97
I.A. 30:70	70	0.43	1.21	0.98
I.A. 20:80	80	1.15	1.10	0.96
I.A. 10:90	90	1.31	0.99	0.95
AESO	-	1.44	0.88	0.95

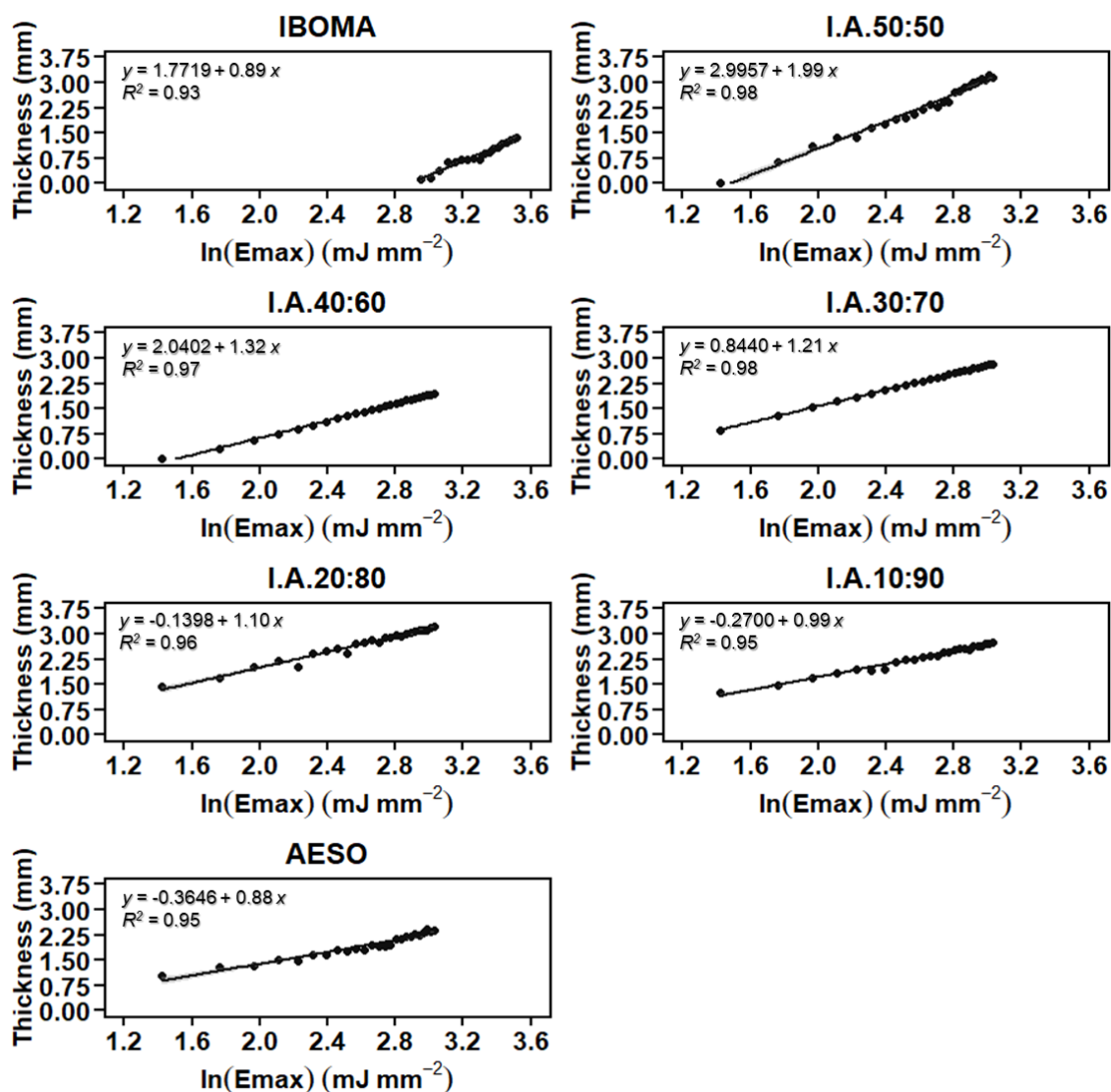


Figure 41: IBOMA, AESO and their respective combinations working curve.

5.4 CONCLUSIONS

This study had the objective of developing a bio-base resin with similar mechanical properties than common commercial petroleum-based resins. The resin was composed of IBOMA and AESO, where the latter was mixed at different concentrations (from 50 to 90%) to find its optimal amount. The resin containing 90% of AESO was too viscous to be 3D-printed, thus it was discarded. Regarding the mechanical properties, the addition of AESO had opposite effects on it. While increasing the concentration of AESO from 50% to 90% improved the parts elongations at break by 45%, it resulted in a decrease of 70% in the tensile strength. Nevertheless, the mixture

containing 50 wt.% of AESO showed mechanical properties similar to other commercial resins and a bio renewable carbon content of 78.5%.

The incorporation of AESO into the IBOMA resin did not show any remarkable effect on either the thermal or thermo-oxidative stability of the UV-cured products. On the other hand, the combination of AESO with IBOMA had a positive on its curing properties, as improvements in both critical energies required and light penetration were observed. In conclusion, the findings confirmed that the developed resin could be a promising alternative to the current petroleum-based counterparts.

CHAPTER 6

SYNTHESIS OF BIOBASED RESIN FOR BIOMEDICAL APPLICATIONS

In this chapter, a biocompatible and biobased resin, made by combining poly(ethylene glycol) diacrylate (PEGDA) and acrylated epoxidized soybean oil (AESO) was designed, developed and fully characterized (mechanical, optical and thermal properties). Before the description of the experimental part and discussion of the main results, a short introduction about the current state of biocompatible resins for 3D printing, their composition and application are presented. Finally, materials, general methods, and instrumentation for characterization were reported in Chapter 3.

6.1 INTRODUCTION

6.1.1 Vat polymerization used for medical applications

The application of 3D printing in medicine is not new, with reports of its usage going as far back as the 1990's.^[196] However, it was only after 2010, with the surge of affordable 3D-printers machines and the development of new biocompatible materials that its usage in medicine exploded. Furthermore, its ability to quickly create personally tailored devices makes it very interesting for applications such as prostheses, temporary dental crowns, epitheses, surgical guides, anatomical models, treatment templates and bone repairs.^[131]

Currently, it is possible to fabricate 3D-printed parts using a variety of materials (ex: thermoplastics, metals, ceramics, organic and photosensitive resins) and by different technologies (like selective laser sintering, fused deposition modeling, vat photopolymerization, and others), where each technology has its own advantages and disadvantages.^[19] Among other different technologies, vat photopolymerization is particularly interesting for medical applications. It has the highest precision of all AM techniques (down to 5 microns of resolution), and the parts fabricated by VP have also demonstrated good thermal and mechanical properties and are chemically stable.^[85,197,198] Moreover, by combining VP with medical imaging techniques (CT scan, MRI and X-rays) it is possible to design and fabricate precise patient-specific models and implants.^[199,200] For example, Patel show several examples of how stereolithography can be combined with computerized tomography to create guide plates, surgical plates and implants for helping rehabilitate oral cancer patients.^[201] Furthermore, Baino et al. developed porous bone scaffolds based on micro-computed tomography (micro-CT) imaging. The scaffold was made of hydroxyapatite and showed 3D trabecular architecture, elastic modulus, intrinsic permeability, pore size, and compressive strength similar to human cancellous bone.^[202]

Another biomedical field in which VP is proving to be exceptional is tissue engineering, for developing scaffolds. A scaffold is a porous implant, designed to be a temporary support

structure that induces the (re)generation of tissues (*in vivo* or *in vitro*) by having seeded cells or nutrients on its surface.^[203] Moreover, after being implanted, it must not provoke severe inflammatory responses and it should biodegrade in the organism, without releasing any toxic substance, as the new tissue is being formed.^[204] Using DLP, Schoonraad et al. 2021 designed scaffolds for cartilage and osteochondral tissue engineering. According to their results, the DLP allowed printing structures with porosity ranging from 94%–75% (higher than other AM techniques). Moreover, they could also control the degree of porosity between each layer of the scaffold, which in turn permitted them to adjust its tensile and compression strength. Controlling the scaffolds design could be useful for treating focal chondral defects, where more than providing mechanical support (similar to native cartilage), it would allow at the same time for cells to proliferate inside it and rebuild the tissue.^[205]

The materials used for biomedical applications are required to follow strict international safety guidelines, being tested and approved by sanitary agencies (like FDA). Some of the clinically approved polymers that can be used for VP are: poly(ethylene glycol) (PEG), poly(caprolactone) (PCL), poly(lactic acid) (PLA) and poly(glycolic acid) (PGA).^[175,206–209] Among these materials, PEG is the best candidate for VP, since polymers with <600 MW are liquid at room temperature and they can be easily functionalized.^[210,211] Wang et al. 2015, combined poly(ethylene glycol) diacrylate (PEGDA) with GelMA and a photoinitiator to develop a biocompatible ink (bioink). Cell culturing analyses showed that for at least 5 days the mixture maintained 85% of cell viability. Moreover, the bioinks consisting of 5% PEGDA and 5% GelMA were capable of printing highly uniform 3D structures (with a resolution of 50 μm).^[212] Mau et al. 2019 used PEGDA and different concentrations of water to print an anatomically customised tubular frontal sinus implant prototype. The authors were successful in printing the prosthesis, having a high degree of dimensional accuracy. However, poor mechanical properties were observed.^[213]

Unfortunately, the objects produced via radical polymerization using pure PEGs and their derivatives have demonstrated poor mechanical properties.^[214] An alternative to improve PEGs properties while maintaining its biocompatibility could be its combination with other types of

resins: in this context, plant-based resins have attractive characteristics due to their renewability, biodegradability, and low pollutant emissions.^[116] Originated from renewable sources, they are environmentally-friendly molecules, relatively cheap to manufacture and employ, and can be modified to react with ultraviolet radiation.^[134,135] Acrylated epoxidized soybean oil (AESO), produced from soybean, has shown to be a promising material, demonstrating good biocompatibility, thermal and mechanical properties.^[134] AESO has also been used for biomedical applications.^[215] Miao et al. 2016, compared AESO to PLA, PEGDA and PCL to print scaffolds capable of changing its form depending on the temperature. Their results showed that the AESO scaffolds had an excellent shape memory effect and had cell attachment and proliferation on par with PCL and PLA.^[147]

Therefore, in this study a new formulation of a biocompatible resin composed of PEGDA and AESO was proposed. The AESO was selected due to its biocompatibility and good thermal and mechanical properties, while PEGDA was preferred due to its cell viability and already proved low cytotoxicity. Different concentrations of AESO were tested and their influence on several properties (mechanical, thermal, optical, rheological and other) were evaluated. The development of new biocompatible resins is fundamental for developing new scaffolds, implants, prosthesis or expanding the VP usage in biomedicine.

6.2 EXPERIMENTAL PART

6.2.1 Photocurable resin formulation

Photocurable resins were prepared to avoid any exposure to light. First, using a lightproof beaker, different weight ratios (varying from 50 to 90 wt.%) of AESO were mixed with poly(ethylene glycol). Then, 2 wt.% TPO was added to the mixtures, which were ultrasonicated for 10 min at room temperature to dissolve the photo-initiator, and thus vigorously stirred for 30 min. The resulting mixture had a yellowish appearance.

The bio content (*BC*) of each *PEGDA/AESO* sample is described in **Table 14** and was calculated according to **Equation 29**, where the *BRC* values of *AESO* and *PEGDA* are 86% and 0%, respectively.^[146]

Table 14: Sample code, composition, and bio-content (*BC*) of each *PEGDA/AESO* mixture.

Sample Code	PEGDA (%)	AESO (%)	BC (%)
P.A.50:50	50	50	43.0
P.A.40:60	40	60	51.6
P.A.30:70	30	70	60.2
P.A.20:80	20	80	68.8
P.A.10:90	10	90	77.4

6.3 RESULTS AND DISCUSSION

In this section, results and discussion of characterization analyses will be provided and divided depending on the analysis/characterization method employed

6.3.1 FT-IR analysis

The FTIR spectra of 3D-printed specimens obtained by uncured and UV-cured *AESO*, *PEGDA*, and their combinations are shown in **Figure 42**. In the wavenumber domain between 1800 and 700 cm^{-1} , the infrared spectrum of uncured *AESO* showed peaks between 1750 and 1700 cm^{-1} and at 1270 cm^{-1} attributed to carbonyl and ester groups, respectively. In particular, the presence of two different absorbance bands at 1737 and 1723 cm^{-1} , both assigned to C=O, is consistent with a different chemical environment for carbonyl groups on monomers. Furthermore, four characteristic absorption peaks were assigned to the stretching vibration of the C=C double bonds at 1636, 1618, 1410, and 810 cm^{-1} .^[216,217] Further infrared absorption bands for *PEGDA*

were assigned to the C–O bonds of the ester groups (1270 cm^{-1} , 1190 cm^{-1} , and 985 cm^{-1}).^[218,219] After the curing process, the FTIR spectra of both resins showed significant changes due to irradiation and copolymerization. In fact, under UV irradiation, the photo-initiator produced active radicals that opened the double bonds in the monomers, thereby promoting crosslinking reactions. The occurrence of photopolymerization was verified by monitoring the double-bond peaks at 1636 , 1618 , 1410 , and 810 cm^{-1} .^[133,163,167,187–189] As shown in **Figure 42**, at the end of the UV curing step, for the PEGDA sample, the double-bond peaks were reduced drastically, which means that they were continuously combining with the created radicals, participating in curing and increasing the crosslinking density. These modifications were more evident in the case of AESO resin, for which the disappearance of the infrared absorption bands assigned to unsaturated C=C bonds indicated that acrylate groups were completely depleted during the UV curing process. The absence of infrared bands assignable to unsaturated C=C bonds in PEGDA–AESO spectra suggests the successful formulations curing.

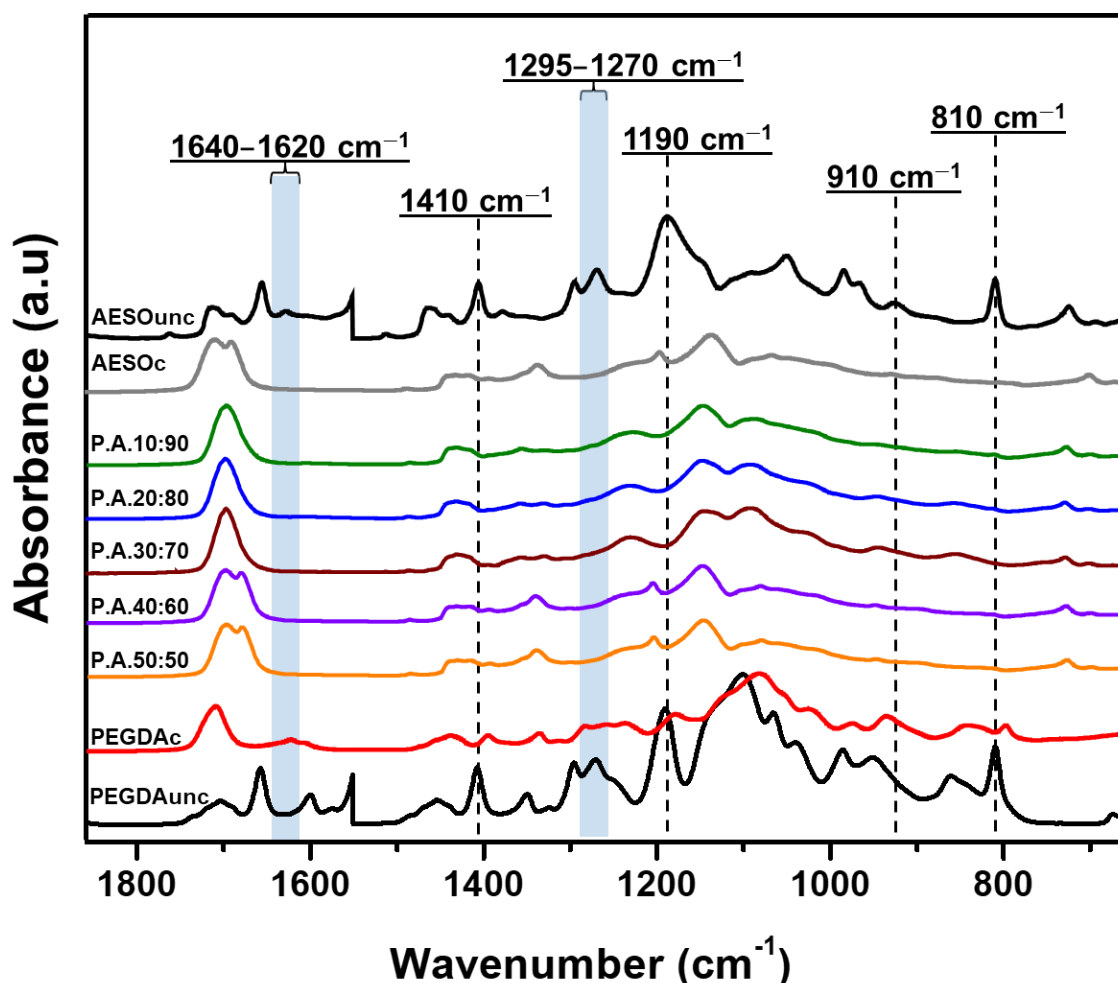


Figure 42: Infrared spectra using attenuated total reflectance of PEGDA with increasing AESO concentrations (from 50 to 90 wt.%). The samples PEGDA_{unc} and AESO_{unc} are the non-cured versions of PEGDA and AESO, respectively. The others samples described in the figure were cured for 40 min (20 min each side) under UV light.

As shown by **Table 15**, the presence of AESO in the 3D printing formulations accounted for a higher conversion of PEGDA acrylic groups, as confirmed by the 810 cm² and 1620-1640 cm² peak area^[165]. Furthermore, the presence of PEGDA did no influenced the epoxy groups conversion, where in some cases had a slightly improvement (samples P.A.40:60 and samples P.A.50:50). This phenomenon could be attributed to the structure of AESO, which has many polar groups (i.e., hydroxyl and epoxy groups) capable of interacting with PEGDA^[180]. This result is particularly interesting for biomedical applications. In fact, the conversion of double bonds is directly related to the material biocompatibility issues, as the presence of unreacted free-radical groups may cause irritation and damage to the soft tissue.^[220]

Table 15: Double-bond conversion at 810 cm^{-1} for PEGDA, AESO, and their mixtures.

Sample code	Peak at 810 cm^{-1}			Peak at 910 cm^{-1}			Peaks at $1620\text{-}1640\text{ cm}^{-1}$		
	Initial area (cm^2)	Final area (cm^2)	Conversion (%)	Initial area (cm^2)	Final area (cm^2)	Conversion (%)	Initial area (cm^2)	Final area (cm^2)	Conversion (%)
PEGDA	0.9662	0.1762	81.76	-	-	-	0.5247	0.1082	79.38
P.A.50:50	0.4978	0.0466	91.52	0.5118	0.1449	83.83	0.537	0.0268	94.47
P.A.40:60	0.5363	0.0569	91.52	0.5349	0.1524	83.83	0.5278	0.0326	94.47
P.A.30:70	0.5745	0.0388	93.25	0.5705	0.1046	81.67	0.5953	0.0249	95.82
P.A.20:80	0.4573	0.0388	89.39	0.6468	0.1046	71.51	0.5623	0.0311	93.82
P.A.10:90	0.4573	0.0388	90.64	0.6468	0.1046	71.69	0.5623	0.0311	95.01
AESO	0.4613	0.0359	92.22	0.6468	0.1218	81.17	0.3284	0.021	93.61

6.3.2 Rheological behavior

Controlling the viscosity is essential when developing resins for 3D printing applications. As discussed in the previous chapter, the viscosity of commercial resins, are usually between 0.1 Pa·s and 1.5 Pa·s.^[113] The viscosity of pure PEGDA is 0.057 Pa·s, while pure AESO has a viscosity of 15 Pa·s. When 50 to 90 wt.% AESO was mixed with PEGDA, the resin viscosity increased according to the AESO loading (**Figure 43**). Furthermore, the mixture containing 90 wt.% AESO was too viscous for the machine to print at room temperature, resulting in failures. Therefore, the maximum amount of AESO that could be mixed with PEGDA was set as 80%.

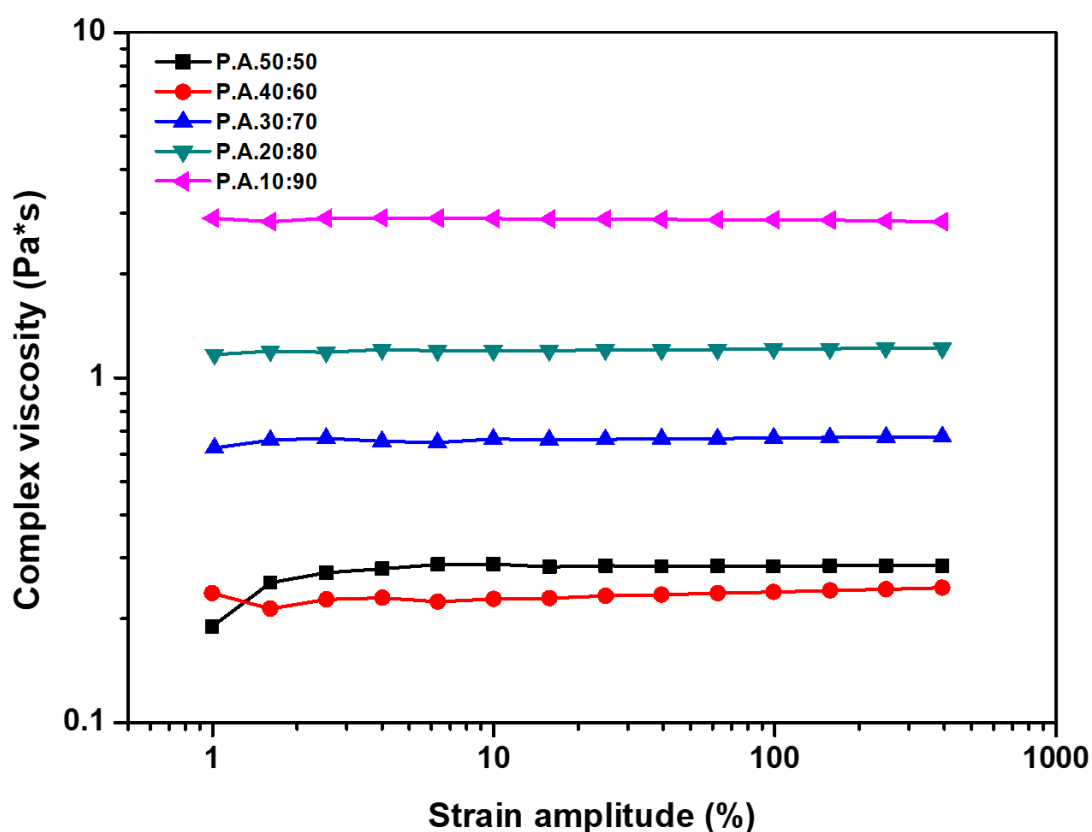


Figure 43: PEGDA viscosity variation with increasing AESO concentrations.

6.3.3 Mechanical properties

The capability to tune and control the mechanical properties of 3D-printed systems is essential when developing objects for biomedical applications.^[169] In the case of biomaterials, their molecular characteristics have a strong influence on the overall mechanical behavior.^[134,170]

The tensile strength of pure PEGDA is approximately $0.6 \text{ MPa} \pm 0.2 \text{ MPa}$.^[175,221] When PEGDA was combined with AESO, the tensile strength showed an impressive increase (**Figure 44**) by 633% ($4.4 \pm 0.2 \text{ MPa}$) when 80 wt.% AESO was added to the 3D printing formulation. However, as observed in the same figure, the samples containing 60 and 70 wt.% of AESO demonstrated an abnormal behavior, going against the expected trend of that the increment of AESO % would improve the samples tensile strength and elongation at break. This drop could be the effect of network loosening,^[135] as well as the presence of bubbles or/and cracks in the specimens (where new tests or a microscopy or SEM analysis should be performed).

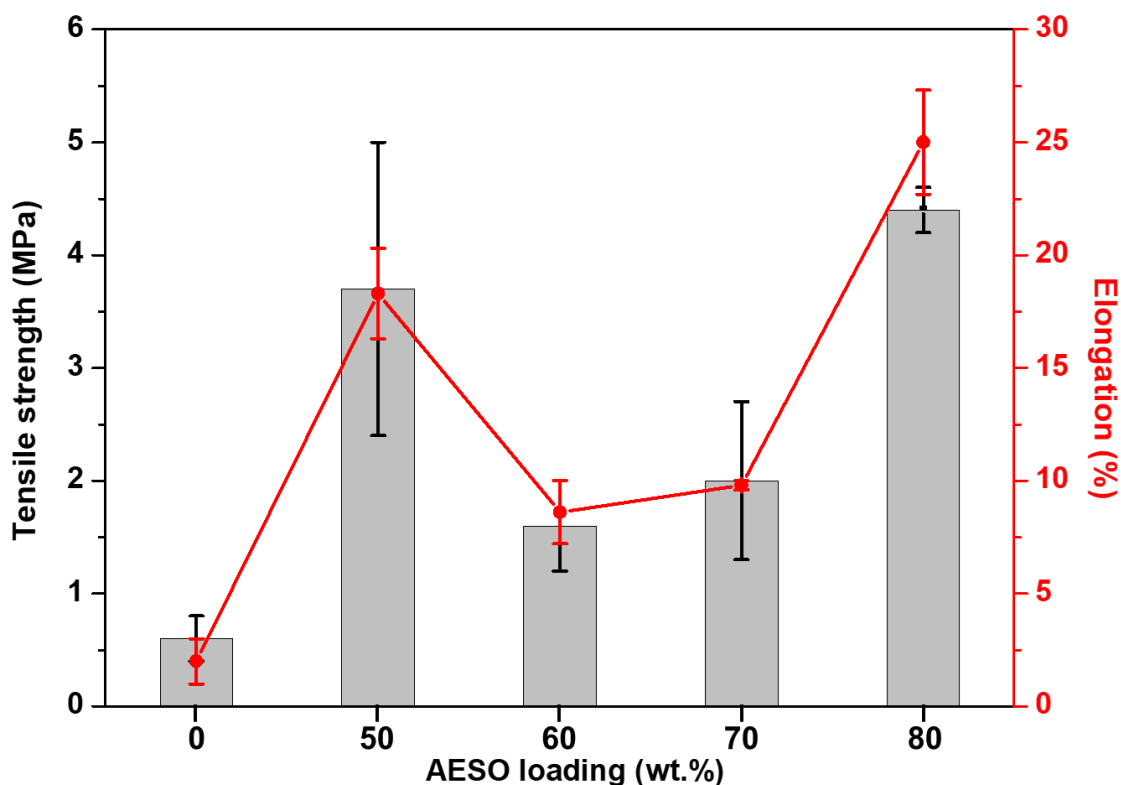


Figure 44: Variation of the tensile strength and elongation as a function of AESO loading. Statistical analysis for the elongation at break was performed using a one-way analysis of variance (ANOVA) with the level of significance set at probabilities of $p < 0.05$.

The elongation at break is related to the material's capability to bend and deform to some extent without cracking.^[172] As previously discussed plant-based resins have a high elongation at break due to the presence of free fatty acids in their structures.^[81,134,135] The addition of AESO resulted in an increase in elongation for all samples (**Figure 44**). Pure PEGDA achieves a maximum elongation of $2\% \pm 1\%$.^[175] When 50 and 80 wt.% AESO were added, and the elongation at break increased by 815% ($18.3\% \pm 2.0\%$) and 1150% ($25\% \pm 2.3\%$), respectively. Finally, among all samples, the formulation containing 80 wt.% AESO provided the best mechanical properties while having the highest bio-content percentage, equal to 68.8%.

The Young's modulus is generally used for assessing the stiffness of a solid material.^[222] Unfilled PEGDA is reported to have a Young's modulus of 26 ± 1 MPa.^[175] However, when different concentrations of AESO were added, Young's modulus decreased on average by 34.7% (**Figure 45**). This decrease is related to the AESO structure and the presence of free fatty acids in

it. Furthermore, changing the AESO concentration did not affect the Young's modulus; this finding may indicate that the elastic deformation was mainly dictated by an AESO–AESO interaction.

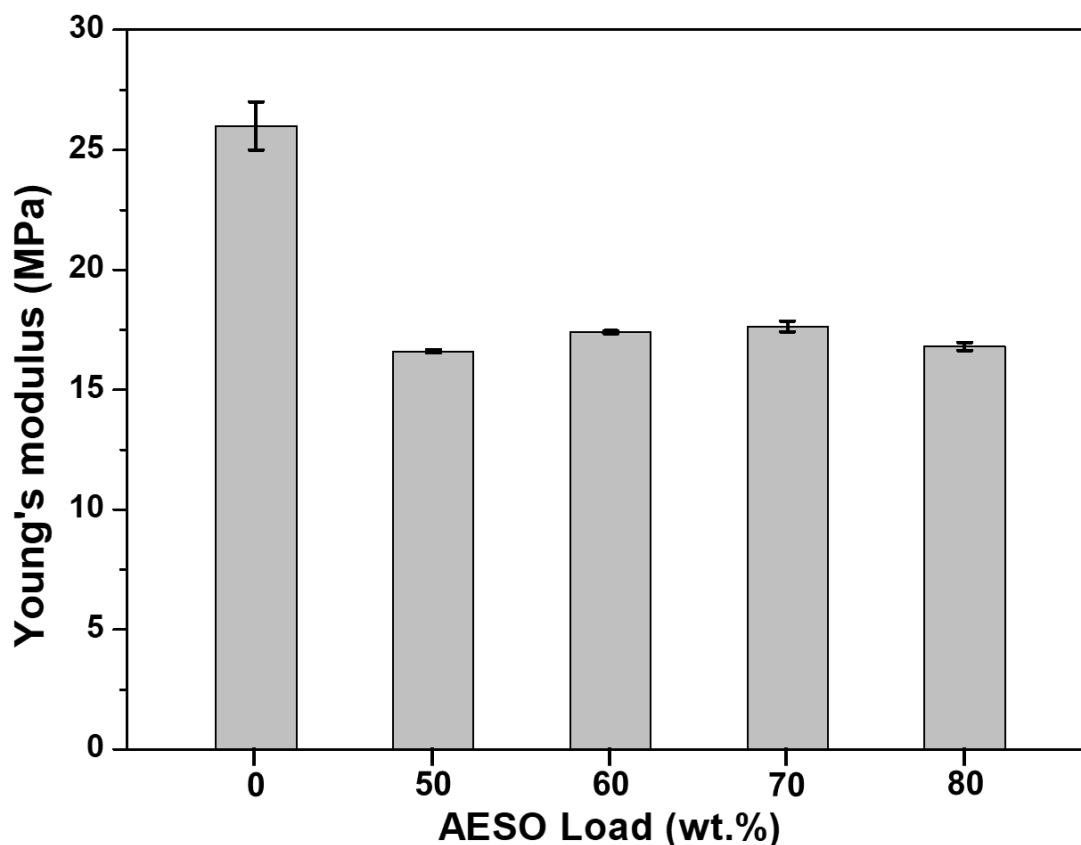


Figure 45: Young's modulus for various PEGDA/AESO ratios.

As previously discussed, the fracture energy of a material is known to have a direct relationship with its toughness. Neat PEGDA has a fracture energy of $0.6 \pm 0.2 \text{ MJ m}^{-3}$ (**Figure 46**). The addition of AESO, which has previously been demonstrated to have good elasticity (with groups in its structure acting as plasticizers), resulted in a decrease in PEGDA's fracture energy in most combinations. The highest decrease was when 60 wt.% of AESO was added, reducing by 67.5%. The only positive gain was seen when 80 wt.% of AESO was added, in which the fracture energy increased by 3.4% (to $0.62 \pm 0.03 \text{ MJ m}^{-3}$).

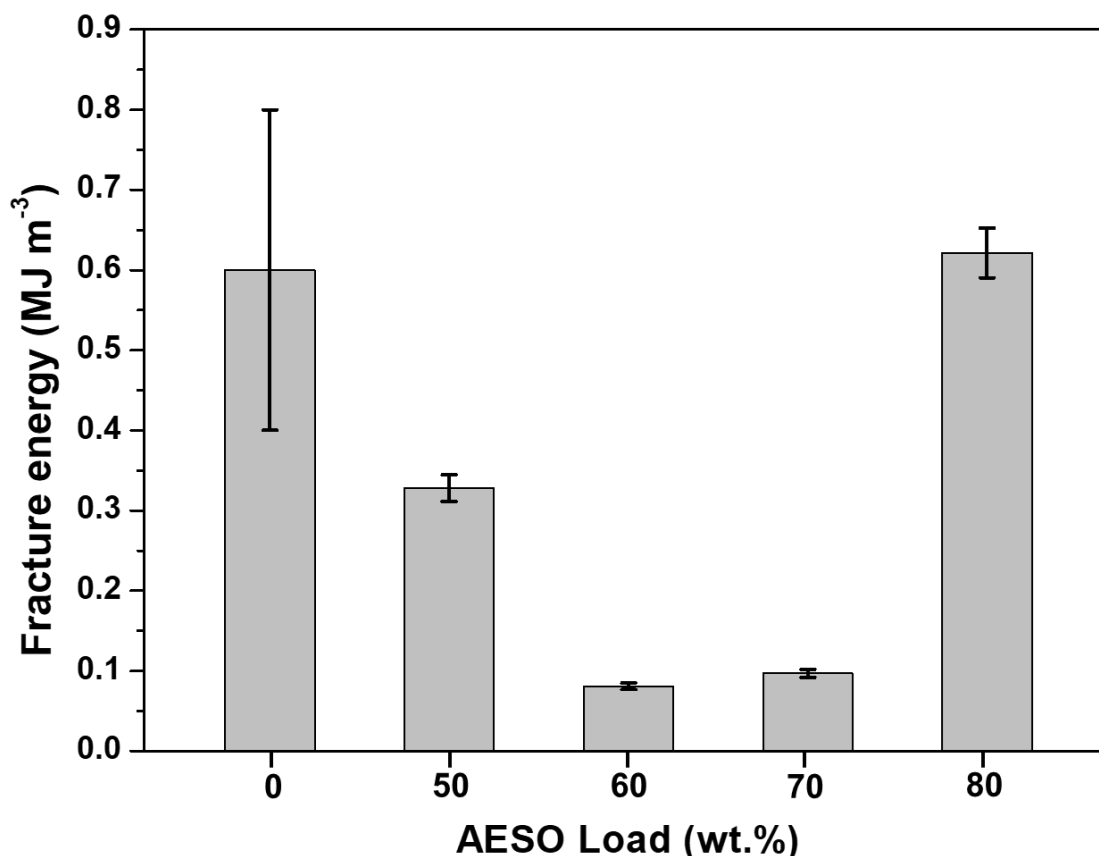


Figure 46: Fracture energy change according to the AESO concentration.

6.3.4 Thermogravimetric Analysis

Thermogravimetric analyses were carried out to assess the thermal and thermo-oxidative behavior of the different UV-cured systems. In nitrogen, the degradation of both PEGDA and AESO, as well as of their UV-cured mixtures, took place with a single degradation step between 300 °C and 500 °C, during which a progressive breaking of the (co)polymer network occurred. Conversely, the degradation in air showed two steps; the first involved the breaking of the (co)polymer network (between about 380 °C and 480 °C), and the second referred to the oxidation of the products formed during the first step. As observed from the data collected in **Table 16**, increasing the acrylated epoxidized soybean oil content decreased the $T_{5\%}$ values in either air or inert atmosphere. This finding can be ascribed to the chemical structure and composition of AESO, which made the molecule less stable and, hence, more prone to degradation; meanwhile,

the bio-sourced resin showed a sort of charring effect, as witnessed by the increase in residues collected in nitrogen at the end of the test.

Table 16: Thermogravimetric data for the different AESO/PEGDA ratios (w/w).

Sample code	Atmosphere	T _{5%} (°C)	T _{max1} ^a (°C)	Residue at T _{max1} (%)	T _{max2} ^a (°C)	Residue at T _{max2} (%)	Residue at 700 °C (%)
PEGDA	Nitrogen	337	420	37.9	-	-	0.5
P.A.50:50		339	429	38.9	-	-	0.5
P.A.40:60		336	429	36.9	-	-	0.9
P.A.30:70		332	432	33.9	-	-	1.0
P.A.20:80		322	428	33.1	-	-	1.4
AESO		308	390	59.0	-	-	2.7
PEGDA	Air	308	413	37.2	538	2.4	0
P.A.50:50		310	424	43.6	554	2.6	0
P.A.40:60		312	428	38.8	528	4.0	0
P.A.30:70		308	425	39.1	539	3.6	0
P.A.20:80		299	426	39.5	554	3.7	0
AESO		293	397	54.0	552	5.7	0

^aFrom derivative curve.

6.3.5 Contact angle

In general, surfaces with moderate wettability are more able to bind to cells and tissues as compared with highly hydrophobic or hydrophilic surfaces.^[175,176,223] Therefore, to determine the surface wettability of investigated composites, PEGDA and AESO contact angles and their combinations, were evaluated, as shown in **Figure 47**. PEGDA, which is known to be

hydrophilic,^[224] showed a contact angle of $72.1^\circ \pm 3.83^\circ$, similar to what has been reported in the literature.^[175] On the other hand, AESO displayed a contact angle of $92^\circ \pm 1.6^\circ$, indicating that it is practically hydrophobic. In fact, even though AESO bears some hydroxyl and epoxy functionalities (i.e., hydrophilic groups), it mainly consists of large nonpolar carboxylic chains.^[180] Thus, upon adding AESO, the PEGDA wettability decreased, and the P.A.20:80 mixture exhibited a contact angle of $93^\circ \pm 2.3^\circ$, which was very close to that of pure AESO.

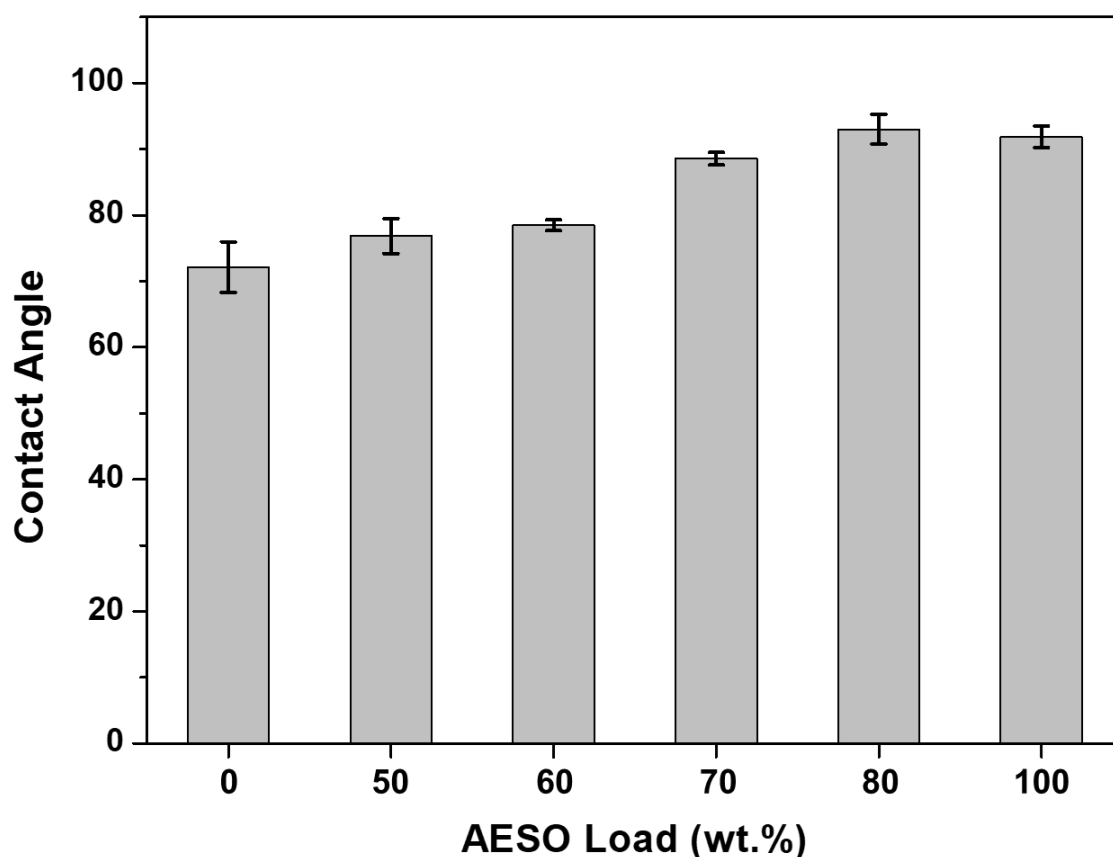


Figure 47: Water contact angle measurements of 3D-printed samples with different AESO concentrations. Statistical analysis for the contact angle was carried out using a one-way analysis of variance (ANOVA) with the level of significance set at probabilities of $p < 0.05$.

6.3.6 Swelling properties

The ability to not deform in an aqueous solution is crucial for tissue engineering when designing implants.^[175,210] Changes in the material's volume can result in deformations affecting the long-term mechanical resistance of the component.^[177,225] As shown in **Figure 48**, pure PEGDA absorbed between 38% and 40% of its weight in water over a 30-day period. The addition of AESO drastically decreased the water sorption of the 3D-printed specimens. After 10 days of immersion in water, the water sorption of the samples containing AESO stabilized without further significant changes. The samples containing 50 and 80 wt.% AESO showed swelling values of 9.4% (a 76% decrease) and 2.75% (a 93% decrease), respectively, after 30 days. The swelling decrease could be attributed to two factors: the AESO large carboxylic chains that prevented water molecules from interacting with the PEGDA hydroxyl groups and the increase in crosslinking density^[179]. In fact, as more AESO was added to PEGDA, the chains became more entangled (and compact), further decreasing the space into which water could diffuse.

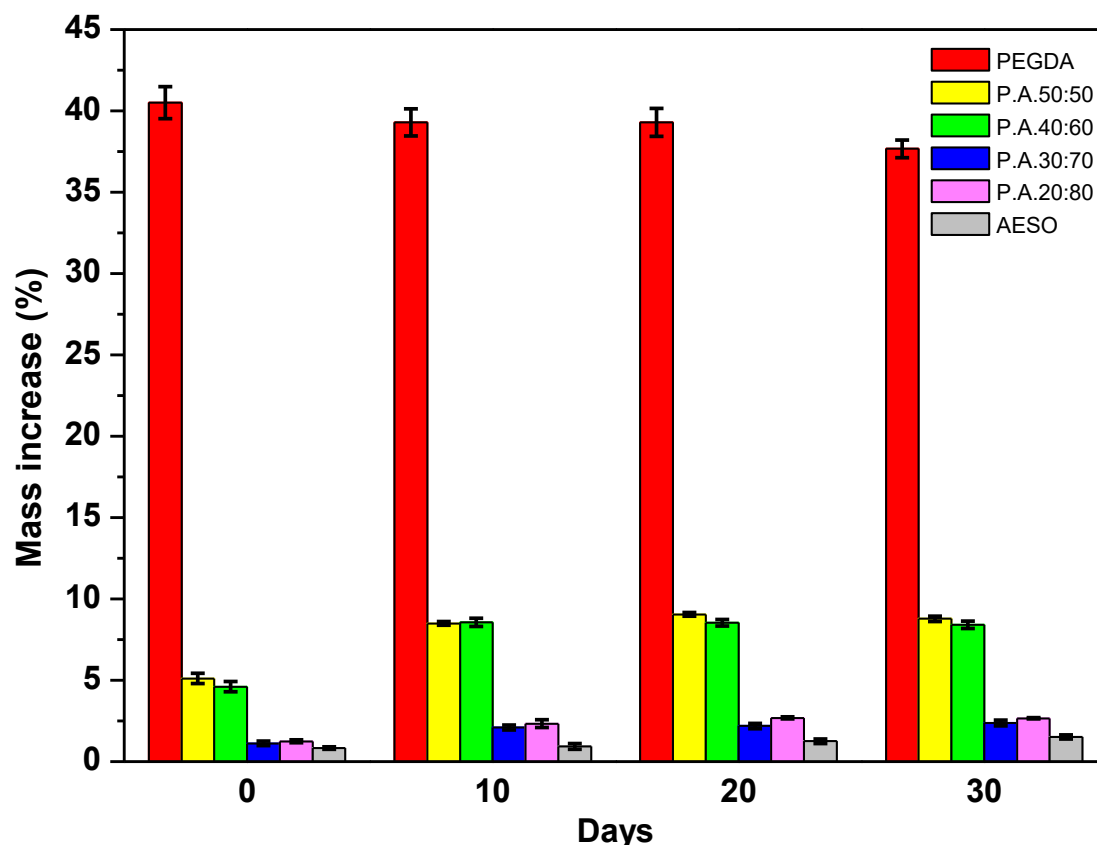


Figure 48: Swelling behavior of 3D-printed parts for 5, 10, 20, and 30 days with different AESO loadings

6.3.7 PEGDA/AESO working curve

The working curve parameters for the PEGDA/AESO mixtures were calculated by ordinary least squares (OLS) regression of the cure depth C_d vs. $\ln(E_{max})$ and are described on **Figure 49** and **Table 17**. During the experiments, neat PEGDA showed to be very sensitive to light, where the scanning speed needed to be increased from 80 mm/s to 100 mm/s in order the last squares to have variations in their heights. This higher light sensitive of PEGDA could be related to its depth light penetration, which is higher than typical commercial resins (**Table 8**, Chapter 4). The light penetration of commercial resins such as Formlabs Clear or PR48, are 0.192 mm and 0.053 mm respectively, where PEGDA's was 1.34 mm. A possible solution to decrease its light sensibility would be the addition of photo blockers or photo absorbers. Nevertheless,

when PEGDA was combined with AESO, its D_p was reduced drastically. The reason behind that could be the neat AESO color. As previously stated, AESO has an amber-like color, which could absorb more UV light at its surface. As PEGDA (transparent) was added, the mixtures' colors became more translucent, allowing more UV to penetrate them.

Table 17: Depth penetration (D_p) and critical energy (E_c) as a function of AESO loadings. Statistical analyses were performed using Pearson's correlation with $p < 0.05$.

Sample code	Loading (wt.%)	E_c (mJ mm ⁻²)	D_p (mm)	R^2
PEGDA _{neat}	-	1.1	1.34	0.95
P.A.50:50	50	1.27	1.01	0.98
P.A.40:60	60	1.30	0.71	0.96
P.A.30:70	70	1.33	0.68	0.97
P.A.20:80	80	1.49	0.42	0.98
P.A.10:90	90	1.41	0.46	0.96
AESO _{neat}	-	1.44	0.88	0.95

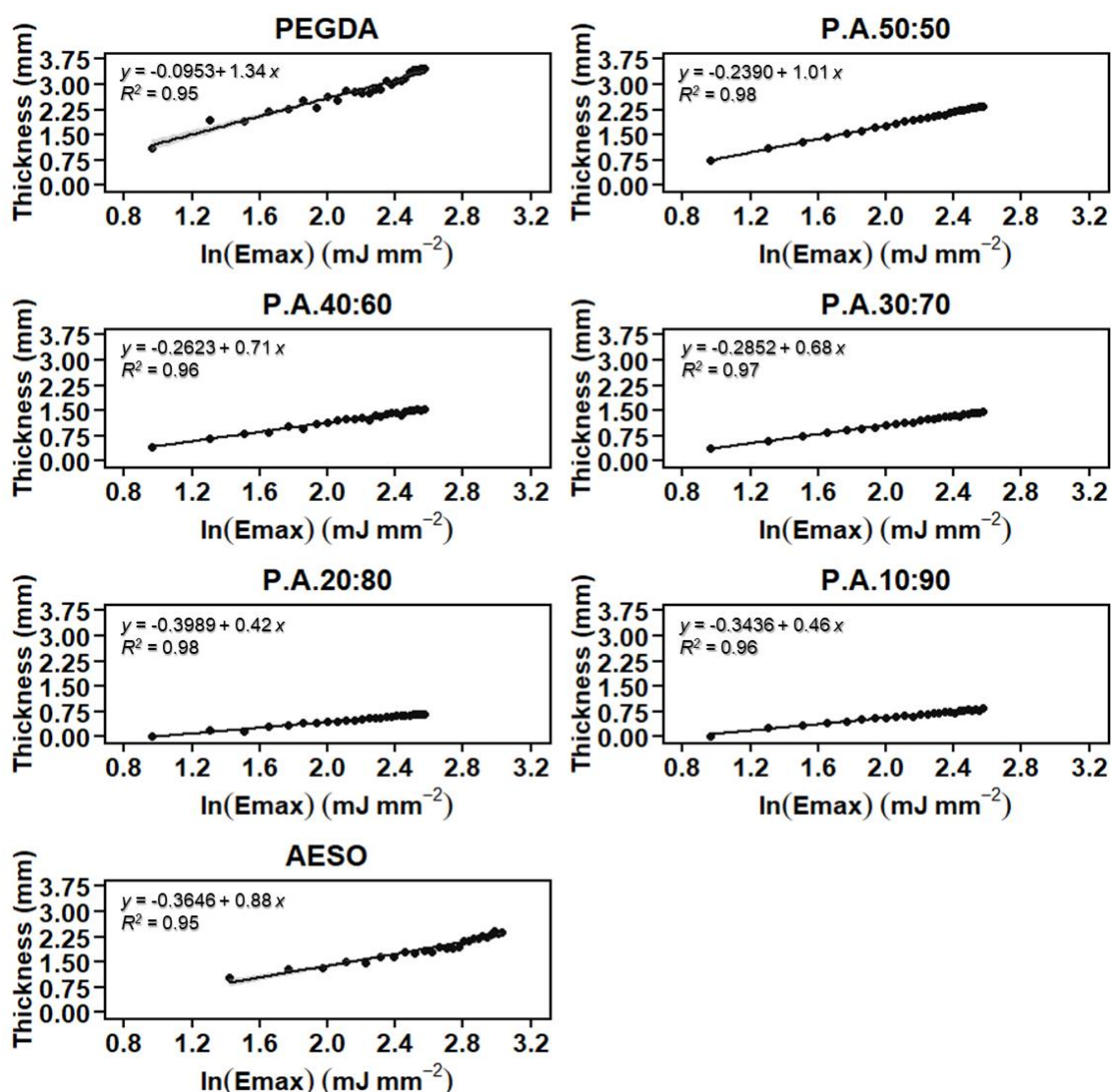


Figure 49: Working curve for pure PEGDA, pure AESO and their mixtures, with AESO concentration varying from 50 wt.% to 90 wt.%.

6.4 CONCLUSIONS

The development of biobased resins for 3D printing is essential to reduce the impact of fossil-based materials in nature and to design new applications. This study focused on the development of a biocompatible resin with good mechanical and thermal properties. Thus, different ratios of PEGDA-to-AESO were tested to identify the best ratio combination for the 3D printing process, i.e., with an appropriate viscosity, good mechanical properties, high bio-content, and optimal reactivity.

In order to evaluate if the resins were suitable for use in a standard 3D-printer, FT-IR and rheological analyses were carried. The addition of AESO resulted in an overall improvement of PEGDA photopolymerization, where all mixtures had conversions above 95%. However, during rheological analyses, the mixture containing 90 wt.% of AESO was too viscous to be used for 3D printing, and thus was discarded.

The remaining resins had their thermal, optical and mechanical properties evaluated. All samples demonstrated similar thermal and optical characteristics. On the other hand, mechanical and swelling analyses showed that their properties were dictated by the AESO concentration in the sample. The sample with 80 wt.% of AESO had the highest tensile strength and elongation at break, 4.4 ± 0.2 MPa and $25 \pm 2.3\%$, respectively. Furthermore, the AESO addition reduced the parts water intake and improved their resistance to deformation.

The development of a new biocompatible resin is important to expand the application of 3D-printing, in which the resin developed in this study showed well defined mechanical and thermal properties. Nevertheless, more studies need to be performed to investigate the parts behavior in a living organism (cellular viability and toxicity). Moreover, the usage of reinforcement materials or different types of resins can also be explored.

CHAPTER 7

REINFORCEMENT AND CHARACTERIZATION OF BIOBASED RESINS WITH MICRO- OR NANOCRYSTALLINE CELLULOSE

In this chapter, microcrystalline cellulose (MCC) and cellulose nanocrystals (CNC) were evaluated as possible reinforcement materials for stereolithography resins. For that, varying amounts of MCC and CNC were mixed in, and different properties were investigated (mechanical, optical, and thermal). The resin used as a base was the P.A.20:80 that was discussed in the previous chapter.

Before describing of the experimental part and discussing of the main results, a short introduction about the types of reinforcement materials for 3D printing, how to disperse them, and applications were presented. Then, materials, general methods, and instrumentation for characterization were reported in Chapter 3.

7.1 INTRODUCTION

The utilization of micro- and nanoparticles as reinforcement materials in additive manufacturing is a well-known practice.^[57,197,210,226] A material is considered a nanoparticle if at least one of its dimensions is under 100 nm,^[227] while microparticles when their dimension is in the range between 1 to 1000 μm .^[228] These materials are usually added to improve the mechanical properties of the final product,^[229] but they can also be used to add new properties to the resin, such as thermal resistance, electrical properties, cell viability and others.^[230] In stereolithography, different types of nanomaterials have been tested such as clay,^[229,231] carbon nanotubes (CNTs) and multiwalled carbon nanotubes (MWCNTs),^[232–234] graphene,^[235] cellulose nanocrystal (CNC),^[175,236] nano silicates,^[237] and many others.

According to the type of material, size, and resin physical and chemical properties, there are different methods to disperse these particles. The main objective is to achieve a homogenous mixture with a printable viscosity. Mechanical methods such as stirring, sonication and ultrasonication are often effective in dispersing the particles. Usually, for low-viscosity resins or small loads of fillers, the particles can be dispersed by stirring^[238] and sonification.^[234] Meanwhile, for high-viscosity resins or high filler loads, the particles are dispersed by ultrasonication (or by combining all methods).^[239,240] However, the heat generated during the sonication process can damage the resin or induce the gelation phase. Nevertheless, it's possible to avoid excessive heat by simply changing the water as it gets hotter or adding ice.^[197,232]

Dispersants are also used to prevent the aggregation of particles when using high loads of materials. Lee et al. used 5 wt.% of Triton X-100, a non-ionic surfactant, with 60 wt.% of copper powder in an SL resin. Since high loads of filler were used, the surfactant was applied to improve the light penetration promoting a scattering effect.^[241] Another possibility is to modify the fillers and increase the affinity between resins and particles. Yun et al. coated Al_2O_3 with silane coupling agents, vinyltriethoxysilane (VTES), through hydrolysis and condensation reactions. Their results showed that when the resin was mixed with 20 wt.% of fillers, coated and

non-coated, the coated particles were more evenly distributed across the liquid. Meanwhile, pure Al_2O_3 agglomerated and sedimented at the bottom, affecting the light penetration and the resin printability.^[242]

Post-processing is usually needed after the homogeneous mixtures are successfully printed in order to remove the support materials or unpolymerized monomers.^[226] The support materials are removed (if needed) manually, using cut pliers or carefully by hand. The process of removing the unpolymerized monomers is divided into two parts. In the first part, the product is washed using an organic solvent, like isopropyl alcohol (IPA), ethanol anhydride or acetone, where the unpolymerized resin is removed from the product.^[113,130,169,175] In the second part, water is used to wash off the alcohol or acetone from the product and then it is dried using air, towel paper or under vacuum (which accelerates the process).^[243]

Post-curing using UV chambers, or even sunlight, is a common practice after cleaning the product. UV light exposure is used to guarantee that any unreacted monomers (inside the object) are photopolymerized, improving its three-dimensional network, resulting in better mechanical properties.^[244] Thermal treatments have also been applied to reinforce the bond between the filler and the resin^[245] or to remove the resin, leaving only the filler.^[241,246,247]

7.1.1 Types of reinforcement fillers used in photopolymerization

7.1.1.1 *Carbon nanotubes and multi-wall carbon nanotubes*

Carbon nanotubes (CNTs) are cylindrical nanomaterials with a large surface area, known for having excellent mechanical, thermal and electrical properties.^[248] They have low density (2.6 g cm^{-3}), high flexibility, high aspect ratio ($\sim 1000:1$), and excellent tensile strength (150 GPa) and are capable of conducting electricity ($\sim 0.5 \mu\Omega\text{m}$).^[249,250] However, proper dispersion of CNTs on systems has shown to be a challenge since it tends to entangle and agglomerate together even in

small concentrations (less than 1 wt.%) due to strong Van der Waals forces.^[248,250,251] Zhang, Y. et al.^[252] examined how various concentrations of CNTs impacts the printability, microwave absorption and electromagnetic properties of his samples. Their research group found out that higher loads of CNTs (1.5%) would lead to frequent aggregate formations and poorer dispersions.^[252] Another important characteristic that must be considered is that CNTs are strong UV absorbers. Eng, H. et al.^[233] reported that the addition of 0.25% of CNTs in photosensitive resins had decreased the UV penetration through the resin. This led to under-curing parts and an increment from 4 seconds to 10 seconds on the cure time needed for each layer.

Nevertheless, small concentrations of CNTs were successfully incorporated into resins.^[253] Gonzalez et al.^[254] studied the impact of different loads of CNTs (0.1, 0.3, 0.5, 1.0 and 1.5 wt.%) on the electrical and mechanical properties of a polyethylene glycol diacrylate combined with polyethylene glycol methyl ether methacrylate macromer (PEGMEMA) mixture. The research team started by investigating the ideal PEGDA:PEGMEMA ratio for the 3D printing process. For that, the viscosity was adjusted to be as low as possible while being able to print. Thus, the best PEGDA:PEGMEMA ratio was found to be 1:1.5 wt./wt. resulting in a 0.015 Pa s viscosity. Furthermore, the viscosity was also used to determine the optimal CNTs concentration, since even small amounts of CNTs could drastically increase the viscosity, affecting the material's printability. Their results showed that with the addition of 1.5 wt.% of CNTs, the viscosity increased from 0.015 to 1370 Pa s. This led to part of the UV light being absorbed, affecting the printer's ability to print. On the other hand, with the addition of 0.1 wt.% of CNTs, the elastic modulus increased by 70%, tensile strength increased by 61% and conductivity doubled.^[254]

7.1.1.2 Nano-clays

There are two important mechanisms of nano-clays to be considered for reinforcing polymers. First, the fillers have a natural resistance to strain due to their high modulus. Second, the single clay particles have a stiffening effect on polymers chains. These two factors resulted in

ressignificantly improved mechanical properties of polymers using small loads of materials.^[255] Weng et al.^[168] combined a photosensitive resin with different concentrations (1, 3, 5 and 10 wt.%) of silica, organic modified montmorillonite (OMMT) and attapulgite (ATP). The addition of 1 wt.% of montmorillonite increased the tensile strength and elongation by 5.7% and 23.49%, respectively. However, both nano-clays (OMMT and ATP) provoked a small distortion on the final part.^[168] Eng H. et al.^[256] applied 1-5 wt.% surface-modified montmorillonite with 35-45 wt.% dimethyl dialkyl into a standard commercial resin. The addition of modified montmorillonite nanoparticles increased tensile strength by 20%, and with 3 wt.% elongation and young's modulus improved 100% and 70%, respectively

7.1.1.3 *Ceramics*

Ceramic particles such as zirconia (ZrO₂), bioactive-glass (BG), alumina (Al₂O₃) and hydroxyapatite, have been used to enhance the mechanical strength and bioactivity of different photopolymers.^[210,257-260] These materials have excellent properties, including high mechanical strength,^[261] excellent thermal and chemical stability,^[262,263] and good optical,^[264] magnetic and electrical performances.^[239,265,266]

For SLA Castro, N. J et al.^[267] combined 10 and 20 wt.% of hydrothermally treated nanocrystalline hydroxyapatite (nHA) with a PEGDA solution (60% of PEGDA 700 Mn with 40% PEG 300 Mw) to fabricate osteochondral scaffolds. Their results showed that the nanoparticles increased the overall elastic modulus by 29% and significantly improved in vitro cell adhesion and proliferation.^[267] Guillaume O. et al.^[268] reinforced poly(trimethylene carbonate) methacrylate (PTMC-MA) with 20 and 40 wt.% of hydroxyapatite nanoparticles to fabricate scaffolds that promote bone repair. Scaffolds containing 40 wt.% of HA had more cell adhesion and absorbed more proteins in comparison with 20 wt.% of HA and no-fillers.^[268]

7.1.1.4 *Silicates*

Nano-silica (SiO_2) is a widely studied additive for photopolymer resins. Silica particles have excellent mechanical and thermal properties,^[237,269] and can improve the cure rate and print accuracy.^[231,270,271] Moreover, it is possible to disperse uniformly nano-silica even at high loads.^[272] Weng Z. et al.^[168] mixed 1, 3, and 5 wt.% loads of SiO_2 in commercial 3D-printing resin. The 5 wt.% SiO_2 loads increased the tensile strength by 20.6% (from 45 to 54 MPa) and the elastic modulus by 65.1% (from 1.7 to 2.7 GPa), without affecting the printer accuracy. Another study proposed by Zhang C. et al.^[271] tested the impact of small silica loads (up to 0.7%) on the SLA mechanical properties. Their results showed that adding of 0.3 wt.% improved the impact strength by 165% and tensile strength by 47%, while achieving excellent particle dispersion. Moreover, 0.7 wt.% silica loads improved the flexural modulus by 130% (from 1.7 to 8.0 GPa).^[271]

7.1.1.5 *Metallic particles*

A variety of metallic fillers (copper, silver, titanium, gold, iron, etc.) have been combined with polymeric materials to improve their mechanical, thermal, and electrical properties.^[273–275] In stereolithography, metallic materials are used in combination with additives and dispersants to decrease the slur viscosity and improve light penetration.^[152,276] Furthermore, after the process is complete, the product can undergo thermal treatments and sintering to better bind or remove the polymer matrix, leaving only a metal structure.^[274]

Sciancalepore C. et al.^[277] applied 1 wt.% of silver nanoparticles (AgNPs) into an acrylic base SLA resin composed of pentaerythritoltriacylate (PETA) combined with Ebecryl 7100 (an amine functional acrylate) and photoinitiators. The presence of AgNPs had an overall improvement in the mechanical properties of the printed parts, where tensile strength increased by 126%, Young's modulus by 254% and stiffness by 153%.^[277] Fantino E. et al.^[278] combined

PEGDA with AgNO_3 , using Irgacure 819 as a photoinitiator, to produce conductive structures. Their samples showed a resistance of $3.6 \text{ M}\Omega$, enough to achieve the illumination of a LED.

7.1.2 Lignocellulosic materials

Cellulose, part of the lignocellulosic components, is the most abundant natural polymer on Earth.^[279] Cellulose can be derived from a variety of sources, such as wood, seeds, plants, animals and microorganisms.^[280] The esterification of cellulose allows it to be processed into various forms, including solutions, fibers and reinforcement materials.^[281] The reinforcement materials derived from cellulose are environmentally friendly, relatively cheap to produce and they can be combined with other materials.^[11–16]

Two major nanomaterials can be produced from cellulose through physical, chemical, or enzymatic approaches. The first one, cellulose nanofibrils (CNF), which is also known as nanofibrillated cellulose (NFC), or the related micro-fibrillated cellulose (MFC), is a flexible material with an average length greater than $1 \mu\text{m}$ and widths in the nanoscale. It has an abundant number of hydroxyl groups, which makes it easier to form hydrogels. It has also been tested as reinforcement material for 3D-printer filaments in the past decade.^[236,288,289] Dong et al.^[290] exploited the abundant hydroxyl groups presented on the CNF to polymerize acid lactic by ring-opening polymerization. Using this process, poly (lactic acid) (PLA) was grafted into the CNF chain, which was subsequently mixed with a PLA filament using different ratios. Their experiments demonstrated that with low dosages of PLA-g-CNFs (3 wt.%), an improvement of 28.56% of young's modulus and 66.28% of tensile strength was obtained. However, for stereolithography applications, cellulose nanofibers are yet to be explored as a possible reinforcement material.

Cellulose nanocrystal (CNC) is the second nanomaterial derived from nano cellulose. It is a very promising reinforcement material for producing green composites due to its ability to

undergo chemical modifications.^[291,292] It demonstrates excellent properties, such as impressive mechanical properties (its tensile strength can reach 200 MPa), optical transparency and high specific surface area.^[293–295] It is hydrophilic, fully biodegradable with the ability to improve thermal resistance.^[286,296,297]

In stereolithography, cellulose nanocrystals were initially tested as a reinforcement for standard commercial SLA resins.^[298] Kumar et al.^[298] investigated how different loads of CNCs would impact the resin mechanical properties. The team tested CNCs loads of 0.5, 1.0, 2.0, and 5.0 wt.%, in which they found out that these loads did not influence the machine capability to print. The storage modulus, tensile strength and flexural modulus had significantly improved when adding 5 and 2 wt.%, respectively, of CNCs. Storage modulus improved 587% when compared with the neat resin. Meanwhile, tensile strength increased from 69 MPa to 82 MPa (a 17% rise) and flexural modulus from 2.6 to 3.3 GPa (a 27% rise).^[298] Feng X, et al.^[299] incorporated various small ratios (0.1, 0.5 and 1 wt.%) of lignin-coated cellulose nanocrystals (L-CNC) into methacrylate to improve its mechanical and thermal properties. The addition of 0.5 wt.% of L-CNC increased the tensile strength by 2.85% (from 66.7 to 68.6 MPa), the tensile modulus by 3.48% (from 1.15 to 1.19 GPa) and elongation by 7.14% (from 2.8 to 3%). Furthermore, with 0.5 wt.%, the thermal stability was improved since it shifted the $T_{5\%}$, T_{max} to higher temperatures.^[299]

In this study, the reinforcement properties of micro- and nano- crystalline cellulose to improve the mechanical properties of the biobased and biocompatible resin developed in the previous chapter was investigated. With this goal, different concentrations of both particles were added to the AESO and PEGDA combination with the best results.

7.2 EXPERIMENTAL PART

7.2.1 Photocurable resin formulation

The mixture of PEGDA/AESO with a 20:80 ratio was selected for the present investigation since it had the best mechanical properties with the most significant bio-content percentage, equal to 68.8%. Then, different percentages of MCCs or CNCs (ranging from 0.15 to 2.4 wt.%) were incorporated into the selected mixture. The fillers were added in a small amount (maximum 0.2 g at a time) and ultrasonicated for 10 min at 30 °C to avoid the formation of aggregates.

7.3 RESULTS AND DISCUSSIONS

7.3.1 Influence of nano fillers on UV curing process

FTIR was also used to investigate the impact of the two fillers on the UV curing process. As shown in **Table 18**, the incorporation of MCCs and CNCs into the resin system containing 80 wt.% AESO did not have a significant impact on the conversion. The spectra, which displayed the typical bands of both cellulosic fillers, are shown in **Figures 50**. The broad peaks at around 3400–3300 cm^{-1} , 2918–2849 cm^{-1} , and 1500–1450 cm^{-1} were assigned to O–H stretching, to the asymmetric and symmetric stretching of methylene ($-\text{CH}_2-$) groups in long alkyl chains, and to C–H in-plane bending of cellulose, respectively. Additionally, the infrared absorption bands at 1369, 1316, 1053 and 897 cm^{-1} were ascribed to C–H deformation stretching, C–H wagging and in-plane ring stretching, C–O stretching, and C–O–C stretching of the β -(1→4)-glycosidic linkage in cellulose, respectively. The incorporation of MCC and CNC into the PEGDA/AESO formulation was not expected to affect the UV-curing process, the same bands were still visible

in the spectrum of the composite containing 2.4 wt.% MCCs or CNCs, where the signals at 1630 cm^{-1} and 830 cm^{-1} , associated with stretching vibration for asymmetric vibration of out-of-plane vinyl groups, indicated the presence of unreacted double bonds.

Table 18: P.A.20:80 photopolymerization conversion in the presence of different loadings of MCCs and CNCs.

Filler type	Filler percentage (%)	Peak at 810 cm ⁻¹			Peak at 910 cm ⁻¹			Peaks at 1620-1640 cm ⁻¹		
		Initial area (cm ²)	Final area (cm ²)	Conversion (%)	Initial area (cm ²)	Final area (cm ²)	Conversion (%)	Initial area (cm ²)	Final area (cm ²)	Conversion (%)
MCC	0.15	0.5419	0.0861	84.11	0.5454	0.1539	71.78	0.5234	0.0595	88.63
	0.30	0.5563	0.0825	85.17	0.5611	0.1512	73.05	0.5249	0.0531	89.88
	0.60	0.5542	0.0516	90.69	0.561	0.1666	70.30	0.5269	0.0906	82.81
	1.20	0.5557	0.0468	91.58	0.5631	0.1666	70.41	0.5208	0.0906	82.60
	2.40	0.5557	0.0702	87.37	0.5631	0.1406	75.03	0.5208	0.0468	91.01

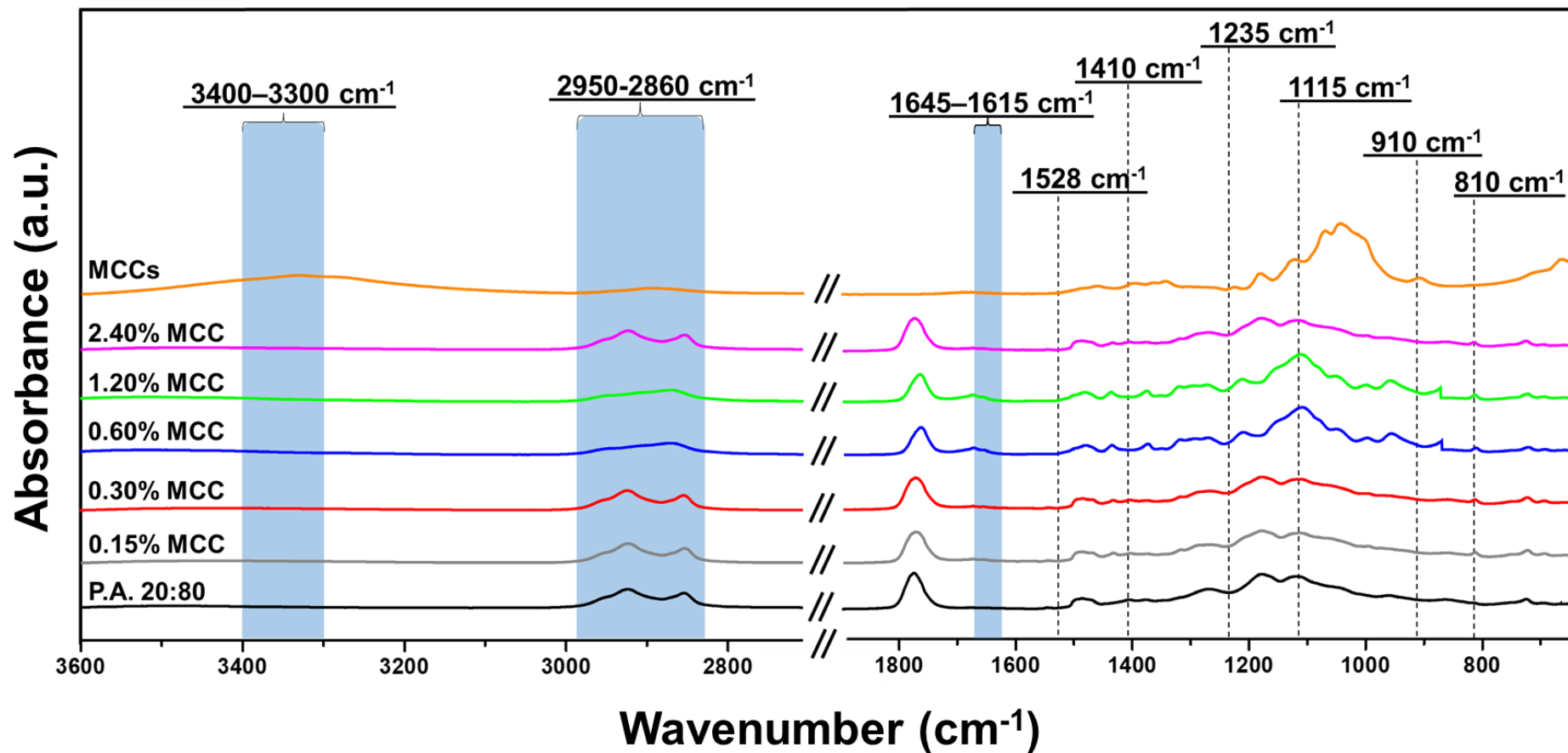


Figure 50: ATR-FTIR spectra of P.A.20:80 sample with varying MCC concentrations. With exception of MCCs, all samples were post-cured under UV light for 40 min (20 min each side).

7.3.2 Viscosity analyses

In order to successfully disperse a filler into a stereolithography resin, it is crucial to know the rheological properties of the system.^[300] Adding fillers can also increase the resin viscosity; thus, their form, sizes, and properties have a greatly impact the outcome.^[65] Even though some printers allows the user to manually set the redistribution time of each layer, by increasing it, the printing time also increases. When particles are added to the resin, the viscosity is influenced by the particle-solvent and particle-particle interactions.^[239]

When a nano dispersion becomes colloidal, unstable particles start to aggregate, which increases drastically the viscosity.^[58,301] These aggregates proceed to accumulate at the printer's vet, which could damage the equipment or, in the case of CLIP printers, disturb the oxygen passage through the membrane. Moreover, the usage of fillers also influences the gel time in two opposite ways. First, the nanoparticles may block the light, which would inhibit the polymerization, prolonging the gel time. Second, the nanoparticles reinforcement effect could promote crosslink, shortening the gel time.^[168] **Table 19** presents some literature examples of the impact of different fillers on viscosity.

Table 19: Different types of fillers and their impact on viscosity.

Filler Type	Amount [wt.%]	Viscosity without fillers [Pa s]	Viscosity with fillers [Pa s]	Ref.
Copper powder	60.0	0.004	0.10	[241]
Hydroxyapatite powder	60.0	0.3	27.44	[302]
Organic modified nano-silica	5.0	0.475	0.75	[237]
Nano-SiO ₂	0.3	0.088	0.09	[271]
MWCNTs	0.5	0.015	36.6	[254]

Cellulose nanocrystals	10	0.13	0.89	[298]
------------------------	----	------	------	-------

a) the ratio for the MWCTs was in weight/volume.

For CNCs and MCCs, both fillers showed similar behavior (**Figure 51** and **Table 20**). The only difference was a slightly higher increase in viscosity when MCCs were dispersed. This difference could be attributed either to the larger particle size of MCCs or to the formation of small aggregates (tested using SEM).

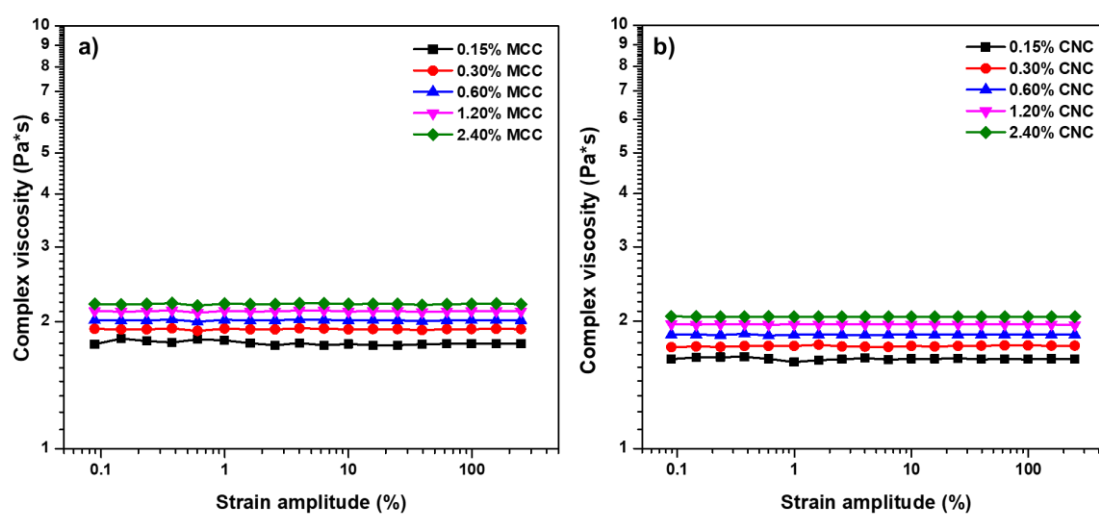


Figure 51: Complex viscosity values of the UV-curable systems as a function of the filler loading in P.A.20:80, where a) corresponds to MCCs and b) to CNCs.

Table 20: Complex viscosity values of the UV-curable systems as a function of the filler loading in P.A.20:80.

Filler type	Loading (wt. %)	Complex viscosity (Pa s)	Increase (%)
-	-	1.27	-
MCC	0.15	1.77	39.37
	0.30	1.92	51.18
	0.60	2.01	58.27
	1.20	2.11	66.14

	2.40	2.20	73.23
	0.15	1.62	27.56
	0.30	1.75	37.79
CNC	0.60	1.86	46.46
	1.20	1.96	54.33
	2.40	2.05	61.42

7.3.3 Mechanical properties

The addition of MCCs and CNCs to the P.A.20:80 mixture had opposite effects on tensile strength and elongation (**Figure 52**). When the fillers were incorporated into P.A.20:80, the elongation at break drastically decreased, from $25\% \pm 2.3\%$ (unfilled resin system) to $3.6\% \pm 0.9\%$, with 0.6 wt.% MCC, and to $8.6\% \pm 0.2\%$, with 2.4 wt.% CNCs (i.e., corresponding to the highest loading). On the other hand, the tensile strength increased by 2.3% and 59.1% when 2.4 wt.% MCCs or CNCs were added, respectively. These findings can be attributed to the inherent stiffness of the cellulose structure.^[298] However, although both fillers are derived from cellulose, CNCs performed better at higher loadings than MCCs; this finding could be ascribed to (i) the lower ductility of MCCs that may result in early breaks, or (ii) the formation of aggregates, which can decrease the tensile strength, as already observed by dos Santos et al., who incorporated CNCs and MCCs into poly(lactide).^[303]

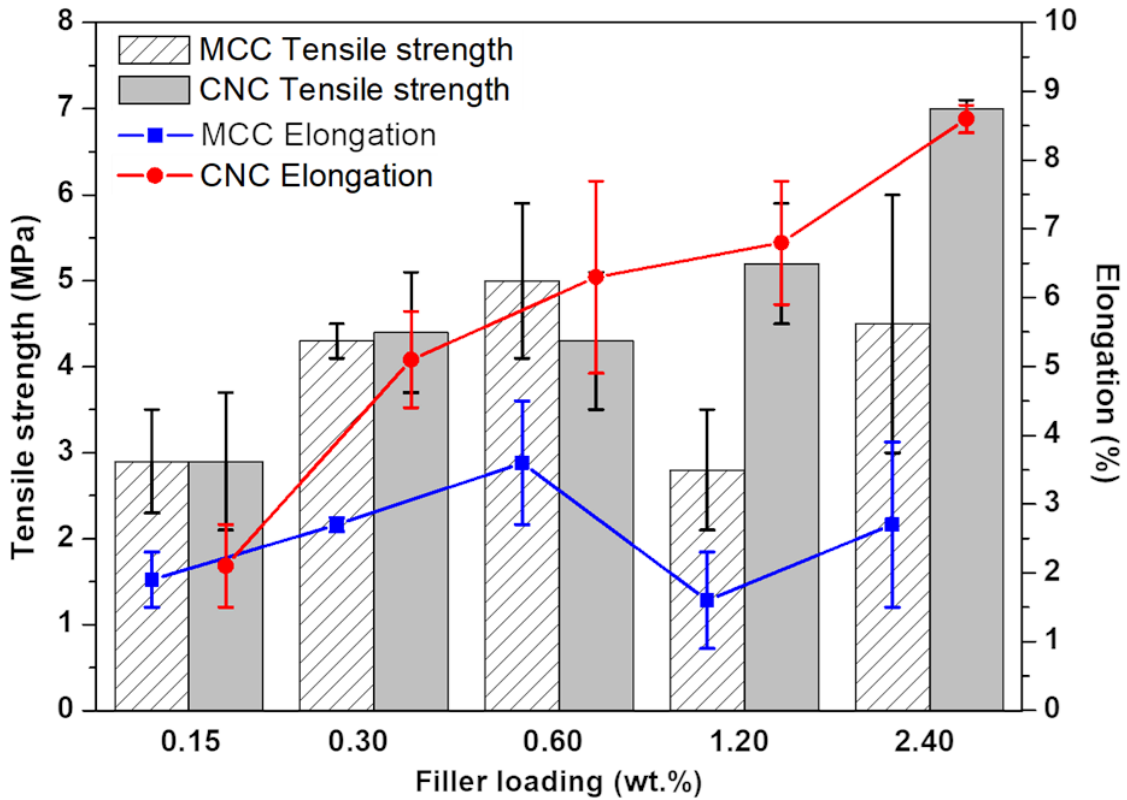


Figure 52: Influence of MCC and CNC loadings on P.A.20:80 tensile strength and elongation at break. Statistical analysis for the elongation at break was performed using a one-way analysis of variance (ANOVA) with the level of significance set at probabilities of $p < 0.05$.

The incorporation of MCCs and CNCs remarkably increased the Young's modulus of the optimized resin formulation. As observed in **Figure 53**, when 0.15 wt.% MCCs or CNCs were incorporated, and both fillers determined an increase in Young's modulus from 16.8 ± 0.17 MPa to 145 ± 0.16 MPa and 144 ± 1.74 MPa, respectively. However, as the weight percentage of fillers in the resin system increased, the presence of MCCs resulted in a higher Young's modulus, nearly achieving two times the value observed in the presence of CNCs, when 2.4 wt.% of each filler was used. This variation could be due to the differences in morphology and chemical surface structure of the fillers, as already reported in the scientific literature.^[303,304]

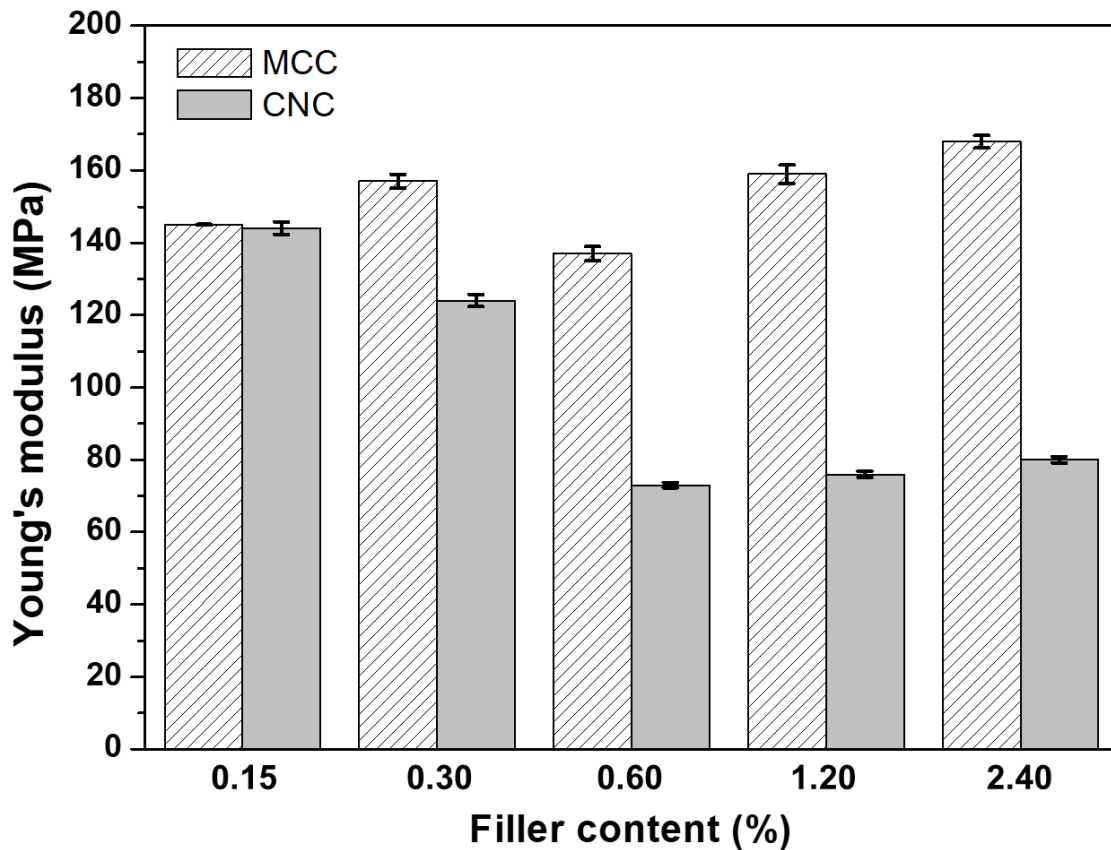


Figure 53: Young's modulus values of P.A.20:80 containing different amounts of MCCs and CNCs.

On the other hand, the addition of MCCs and CNCs drastically reduced P.A.20:80 fracture energy (**Figure 54**). Neat P.A.20:80 has a fracture energy of $0.62 \pm 0.03 \text{ MJ m}^{-3}$. When 0.15 wt.% of MCCs and CNCs were incorporated, the fracture energy was reduced by 95.6% and 94.8%, respectively. Even though adding higher loads of CNCs increased the mixtures fracture energy, reaching 0.29 MJ m^{-3} when 2.4% was added, it still was 53.2% lower than neat P.A.20:80. This reduction is related to the crystalline structure of cellulose, which in one hand improved the tensile resistance of the mixtures but made them less tough, similarly to what happened to their ductility.

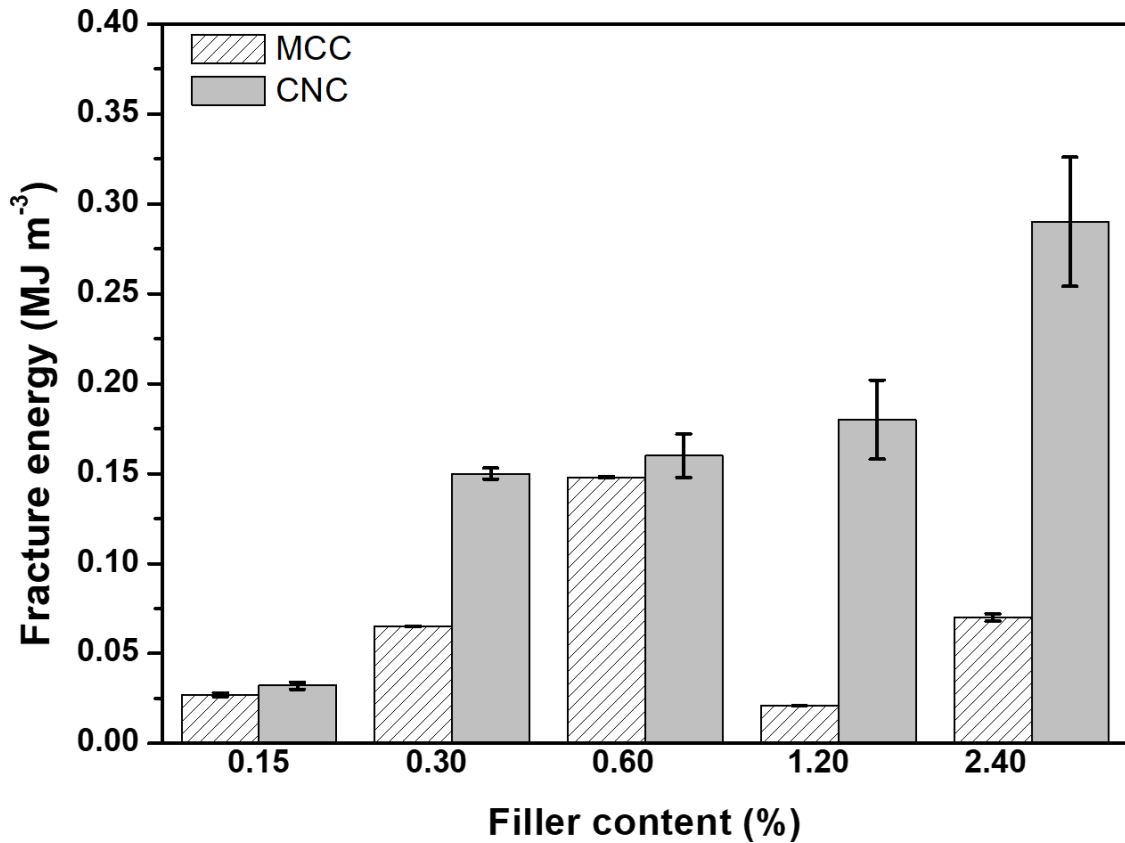


Figure 54: Influence of increasing loads of MCCs and CNCs on the P.A.20:80 fracture energy.

7.3.4 Scanning electron microscopy

SEM analysis was carried out to assess the morphology of the composites and the level of distribution of the micro- and nanocellulose crystals. Some typical SEM images are shown in **Figure 55**. Unfilled 3D-printed P.A.20:80 (**Figures 55 a and b**) showed a rough surface, which became quite smooth when each filler was embedded. The micrographs of the systems containing MCCs and CNCs (**Figures 55 c to f**) showed the achievement of good interfacial adhesion between the embedded fillers and the resin. Furthermore, it is noteworthy that both the systems were prone to forming some aggregates (average size between 10 and 20 microns), although the overall dispersion was quite uniform.

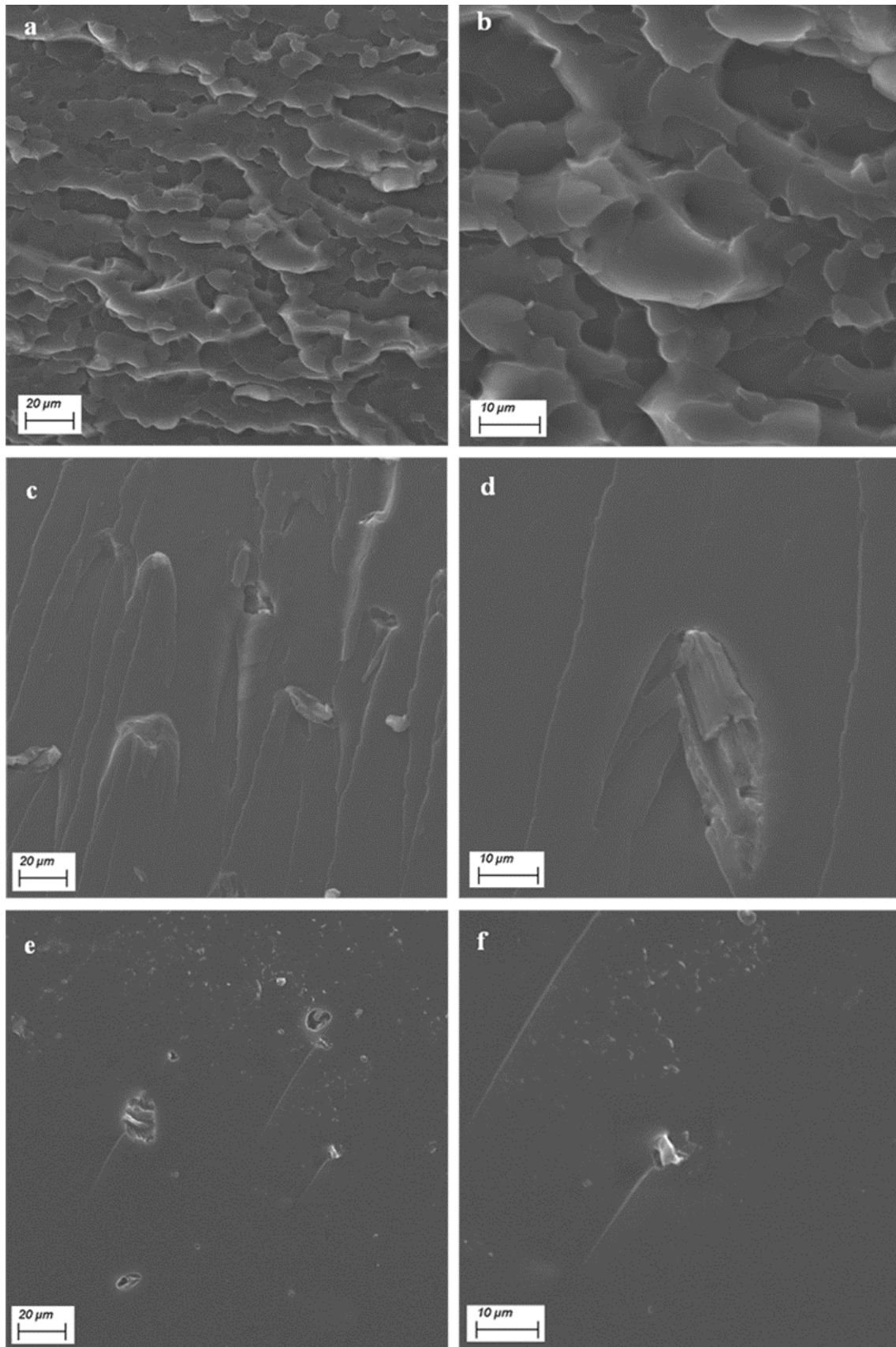


Figure 55: Typical SEM micrographs of (a,b) unfilled P.A.20:80 and samples containing 0.60 wt.% (c,d) MCC and (e,f) CNC.

7.3.5 Thermogravimetric characteristics

The incorporation of micro-cellulose crystals into the optimized resin mixture containing 80 wt.% AESO seemed to have a very limited effect on the thermal and thermo-oxidative stability of the 3D-printed composites (**Figure 56**). In fact, all the characteristic temperatures were almost unchanged and very close to those of the unfilled system (see **Table 21**). Similar behavior was also found for the 3D-printed composites containing different amounts of nanocellulose crystals (see **Table 22**), notwithstanding a slight decrease in the T5% values in nitrogen for all filled systems, regardless of CNC loading.

Table 21: Thermogravimetric data for MCCs-based composites.

Sample code	Atmosphere	T _{5%} (°C)	T _{max1} ^a (°C)	Residue at T _{max1} (%)	T _{max2} ^a (°C)	Residue at T _{max2} (%)	Residue at 700 °C (%)
P.A.20:80	Nitrogen	322	428	33.1	-	-	0.9
+ 0.15% MCC		322	431	34.2	-	-	1.1
+ 0.30% MCC		320	430	32.1	-	-	0.9
+ 0.60% MCC		317	429	32.9	-	-	0.8
+ 1.20% MCC		320	429	34.2	-	-	1.2
+ 2.40% MCC		316	429	33.0	-	-	1.1
P.A.20:80	Air	299	426	39.5	554	3.7	0
+ 0.15% MCC		297	420	41.2	555	4.3	0
+ 0.30% MCC		298	421	39.6	550	4.3	0
+ 0.60% MCC		300	421	40.0	547	4.2	0
+ 1.20% MCC		298	419	41.2	547	4.1	0
+ 2.40% MCC		297	421	39.5	551	4.2	0

^a From derivative curve.

Table 22: Thermogravimetric data for CNCs-based composites.

Sample code	Atmosphere	T _{5%} (°C)	T _{max1} ^a (°C)	Residue at T _{max1} (%)	T _{max2} ^a (°C)	Residue at T _{max2} (%)	Residue at 700 °C (%)
P.A.20:80	Nitrogen	322	428	33.1	-	-	0.9
+ 0.15% CNC		312	423	33.7	-	-	0.9
+ 0.30% CNC		315	424	35.8	-	-	1.0
+ 0.60% CNC		317	424	34.9	-	-	1.1
+ 1.20% CNC		316	424	34.4	-	-	1.2
+ 2.40% CNC		308	422	34.4	-	-	1.3
P.A.20:80	Air	299	426	39.5	554	3.7	0
+ 0.15% CNC		284	412	47.2	544	4.4	0
+ 0.30% CNC		290	417	45.0	544	4.5	0
+ 0.60% CNC		295	421	39.0	552	4.1	0
+ 1.20% CNC		292	420	40.3	550	4.2	0
+ 2.40% CNC		297	421	40.2	546	4.0	0

^a From derivative curve.

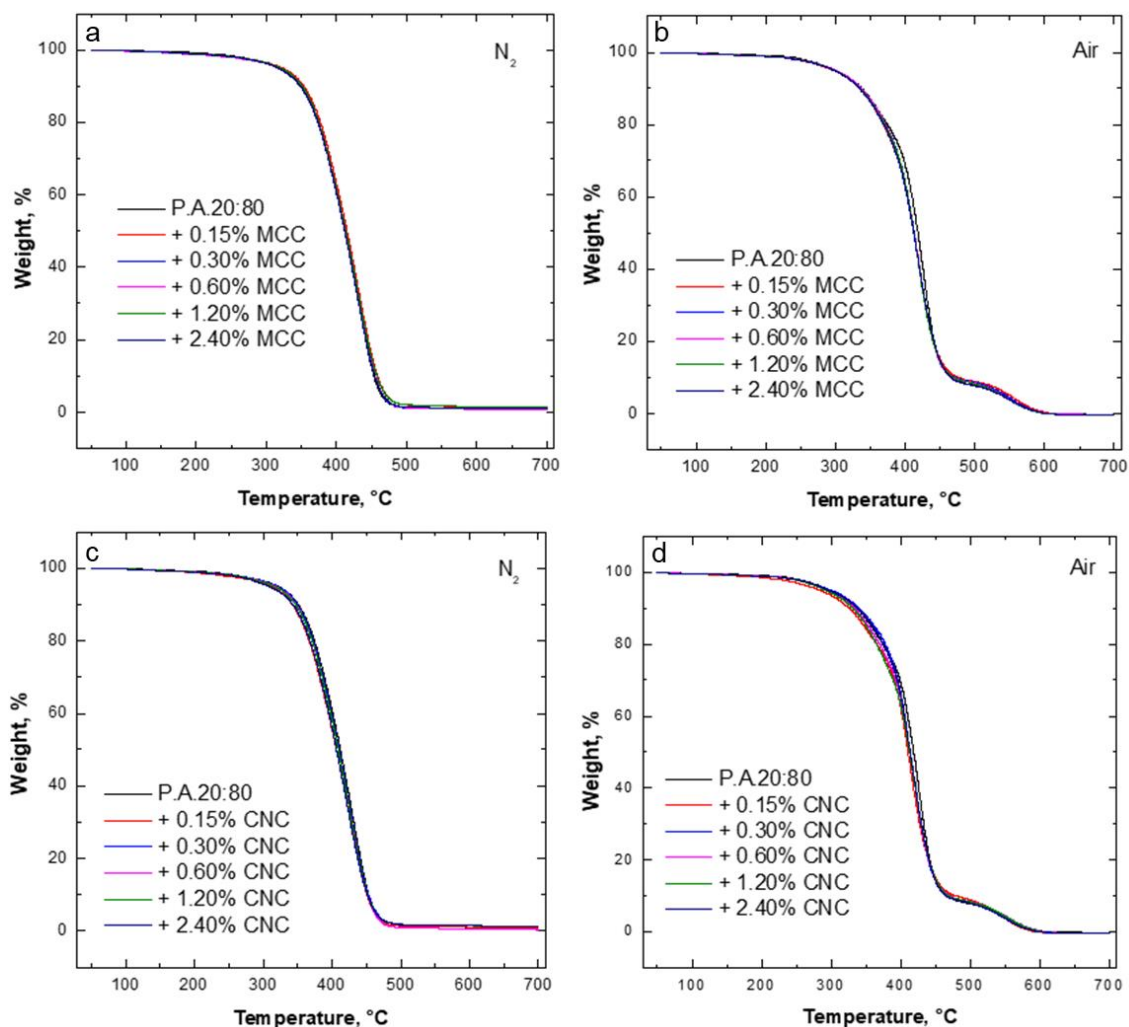


Figure 56: Thermogravimetric curves of the resin mixture containing 80 wt.% AESO with varying concentrations of MCC (a,b) and CNC (c,d) in air and N₂ heated at a constant rate of 10 °C·min⁻¹.

7.3.6 Swelling analyses

When MCCs and CNCs were added to P.A.20:80, its swelling demonstrated a small variation after 30 days of immersion, in the range of 2 and 2.5% (**Figure 57**). Even though the addition of the fillers did not significantly impact the water sorption of the 3D printed parts, increasing their concentration led to higher swelling. This finding could be attributed to the high number of -OH groups present in the cellulose structure, which increases the hydrophilicity.^[221]

Finally, all the printed parts showed good mechanical integrity during the 30 days of dipping in water.

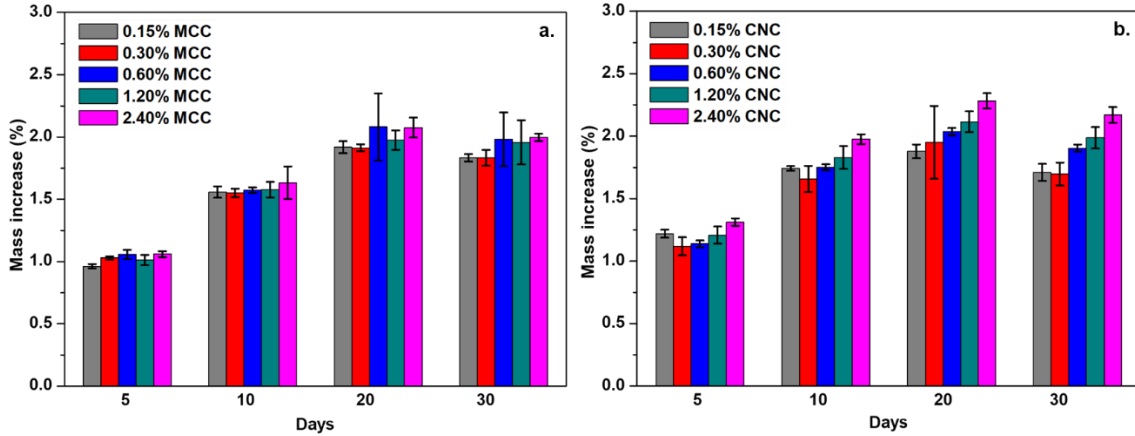


Figure 57: Water intake of P.A.20:80 with increasing amounts of (a) MCC and (b) CNC over a 30 days period of time.

7.3.7 Contact angle

As previously discussed the addition of MCCs and CNCs increased the parts water intake due to the hydrophilic nature of cellulose.^[221] Thus, one expects that the wettability of the parts would increase. Indeed, as presented in **Table 23**, the contact angle decreased by about 34%, in the presence of MCCs, and by 43%, in the presence of CNCs. However, the wettability increase was not correlated with the filler concentration.

Table 23: Contact angle values using water for P.A.20:80 and its composites containing MCCs or CNCs. Statistical analyses were performed using Pearson’s correlation for MCC and CNC with $p < 0.05$.

Filler type	Loading (wt. %)	Contact angle (°)	Standard deviation
-	-	93.0	2.3
MCC	0.15	61.9	5.1
	0.30	61.8	5.7

	0.60	60.5	3.8
	1.20	63.2	3.0
	2.40	59.0	4.0
	0.15	51.9	2.1
	0.30	58.4	4.2
CNC	0.60	53.9	0.7
	1.20	48.7	0.2
	2.40	52.1	2.4

7.3.8 Working curve parameters

Another important factor that must be considered when adding fillers to resins is the effect of particles on the scattering of UV light. Typically, the cure depth of a given resin is determined by the amount of light the resin was exposed.^[86,305] However, when fillers are added to a resin, the scattering of light by these particles starts to influence the energy needed to cure the resin (Table 24).^[155] As the concentration of particles increases, it becomes more difficult for the UV light to pass through the resin and cure the layers.^[155] This happens because part of the UV is absorbed by the particle. Finally, depending on the particle size, filler type, photoinitiator or resin used, the depth of cure will vary.^[239]

Table 24: Changes in E_c and D_p with the addition of different types of fillers.

Filler type	Filler content [wt.%]	Critical exposure value E_c [mJ cm ⁻²]		Penetration depth D_p [mm]		Ref.
		Initial	Final	Initial	Final	
VTES-coated Al ₂ O ₃	15.0	13.50	25.40	0.12	0.96	[242]
Organic modified nano silica	1.0	11.46	12.94	0.11	0.10	[237]

Nano-SiO ₂	0.3	9.82	10.98	0.12	0.11	[271]
MWCNTs	0.1	11.50	19.50	0.16	0.16	[250]

The P.A.20:80 had a E_c and D_p of 1.49 mm and 0.42 mJ cm⁻², respectively. When MCC and CNC particles were added D_p decreased as their concentration increased, as shown by **Table 25** and **Figures 58** and **59**. The lowest value of D_p was reached when 2.4 wt.% cellulose was incorporated; specifically, it shifted from 0.43 mm to 0.32 mm, with MCC, and to 0.35 mm, with CNC. Although this decrease would imply that more energy (or time) would be needed to perform the UV curing, its value is still higher than other standard commercial resins. Moreover, the addition of particles reduced the amount of energy needed to start the photopolymerization reaction, as represented by a reduction of E_c . The effect of scattering particle size on the reduction of energy efficiency could be the reason behind that, where part of the light that would penetrate the resin is now being redirected sideways. Lastly, the variation between MCC and CNC E_c values could be related to their particles sizes^[306].

Table 25: Depth penetration (D_p) and critical energy (E_c) as a function of MCCs and CNCs loadings. Statistical analyses were performed using Pearson’s correlation for MCC and CNC with $p < 0.05$.

Filler type	Loading (wt. %)	E_c (mJ mm ⁻²)	D_p (mm)	R ²
MCC	0.15	0.94	0.34	0.98
	0.30	0.92	0.35	0.98
	0.60	1.06	0.35	0.96
	1.20	1.00	0.32	0.96
	2.40	0.97	0.32	0.97
CNC	0.15	1.16	0.39	0.99
	0.30	1.04	0.36	0.98
	0.60	1.05	0.37	0.96

1.20	1.03	0.36	0.98
2.40	1.04	0.35	0.97

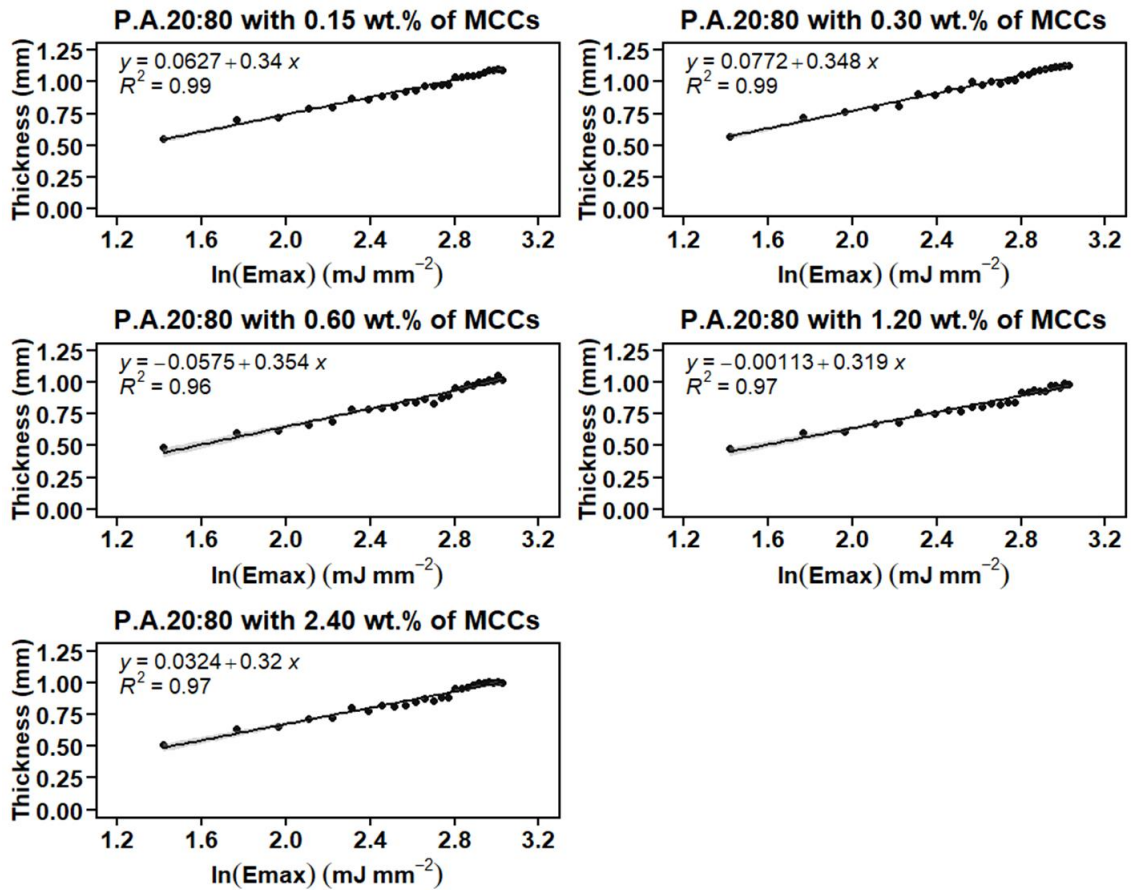


Figure 58: Working curve for P.A.20:80 with increasing concentrations of MCCs, from 0.15 wt.% to 2.40 wt.%.

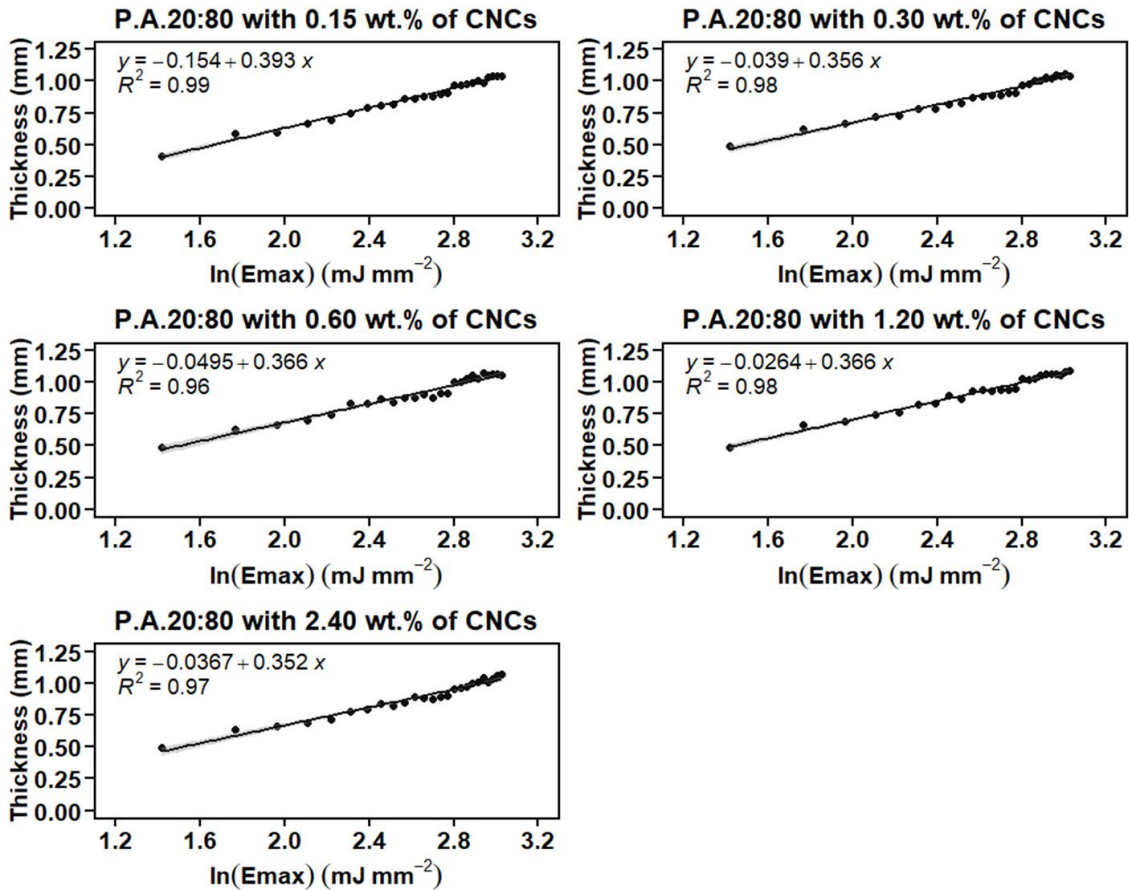


Figure 59: Working curve for P.A.20:80 with increasing concentrations of CNCs, from 0.15 wt.% to 2.40 wt.%.

7.4 CONCLUSIONS

The development of new types of biobased resins for 3D printing is essential to reduce the usage of fossil-based materials and to expand their applications. This study focused on the reinforcement of a biocompatible to improve its mechanical properties.

The incorporation of various loads of fillers (up to 2.4 wt.%) into the P.A.20:80 resin did not interfere with the 3D-printing process. Although the light ability to penetrate the resin reduced as the particle loads increased, the presence of these particles also reduced the energy needed to start the photopolymerization (through scattering effect). The presence of the cellulose crystals, irrespective of their size, increased the wettability of the printed parts, with a lowering of the water contact angle values by about 34% and 43%, when 2.4 wt.% of CNC and MCC were

incorporated, respectively. Moreover, the water intake also slightly increased by an average of 1 – 2.5% over 30 days period with the filler's incorporation. These findings were attributed to the high polar characteristic of the fillers, bearing several hydroxyl groups, increasing the P.A.20:80 hydrophilicity. Meanwhile, as assessed by mechanical tests, the tensile strength increased by about 59%, in the presence of 2.4 wt.% of CNCs, and the Young's modulus by 890%, when the same MCC loading was employed. However, further research on the influence of AESO:PEGDA resins and its combination with CNCs and MCCs on cellular proliferation and tissue response is needed understand its impact on living cells better. In conclusion, the composite system developed in this work may represent a sustainable solution to the increasing demand for new environmentally friendly materials for additive manufacturing processes.

CHAPTER 8

CONCLUSIONS AND FUTURE PERSPECTIVES

As the world becomes more environmentally conscious, there has been a lot of research and investment in the development of new technologies that could improve productivity while decreasing the amount of raw material and energy needed during the process. Among the different types of technology developed in the last decade, vat photopolymerization, one of the seven additive manufacturing technologies, has been gaining a lot of attention due its versatility, cost, and ability to fabricate complex structure using a range of materials.

Initially, vat photopolymerization was used for very limited applications, such as for producing small prototypes. Still, with the development of new technologies and their optimization, nowadays many industrial and non-industrial sectors are using this new technology for manufacturing high end products. Furthermore, thanks to scientific research, vat photopolymerization has been integrated with other technologies, such as imaging technologies, which allows the user to replicate real structures precisely. This is particularly interesting for biomedical applications, where implants and prothesis need to be tailored specifically for each patient.

In order to keep up with the advances of VP, new types of materials also needed to be developed. Especially biobased, biocompatible and (bio)degradable materials since most of the resins that were initially developed for VP in the beginning (and are still used nowadays) are derived from petroleum. These new bio-resins can be produced from various types of raw materials, but vegetable- and plant-based resins are particularly interesting. They can be produced worldwide, are cheap to manufacture and can have their structure modified by different types of chemical processes (addition, grafting, ring opening) to have epoxy and acrylic groups added to it.

Among the several types of vegetable-oils and plant-based materials, acrylated epoxidized soybean oil (AESO) showed to have good mechanical, curing and thermal properties, low shrinking rates and swelling as well as biocompatible and biodegradable. It has already been used for coating applications but its potential for photopolymerization has yet to be fully studied.

Different concentrations of AESO were combined with a standard commercial petroleum-based resin where their impact on several properties was investigated. The photopolymerization efficiency was confirmed by using FT-IR analyzes, which showed that even at high concentrations of AESO the reaction proceeded normally. Furthermore, working curve analysis showed that AESO have similar curing properties of the standard resin that it was mixed into, so there is no need to add photo blockers or absorbers to the mixture. Thermal and mechanical analyzes of the mixtures showed different behaviors. In the first case, only a slight variation was observed, where in the second the tensile strength reduced almost by half when AESO was added and continued decreasing as its concentration increased. Nevertheless, when compared to other commercial resins, the mixture containing 20% of AESO still demonstrated similar properties. Finally, the lost in tensile strength was gained in elongation, as the parts became more flexible.

Having used AESO to improve the biocarbon content of a commercial resin to make it more environmentally friendly, the next step was to develop a complete biobased resin. For that a plant-based resin/diluent was used, known as IBOMA. They were mixed at different mass ratios and the combination that produced parts with the best mechanical properties was compared to

standard commercial resins. The photopolymerization reaction and conversion rate was verified using FT-IR analysis, which showed conversions above 80%. Furthermore, curing tests revealed that the bio-based resin needs less energy to cure when compared to commercial resins. Another good result was obtained when mechanical evaluations were performed. The resin demonstrated great tensile strength, tunable elongation at break and swelling resistance, which were similar to standard petroleum-based resins. This shows its potential to substitute these resins on the short period of time and with further research and optimization to surpass high performance resins.

On another field that AESO demonstrated to have great potential is for biomedical application. Literature reviews had demonstrated a few applications of AESO for creating scaffolds, but its high viscosity indicated to be a deterrent. In this work, for the first time AESO was combined with another biocompatible material, PEGDA, and its properties were investigated. Compared to raw PEGDA, the combination with AESO demonstrated significant gains in its mechanical and swelling properties, where the produced parts had higher resistance and deformed less. Moreover, its curing and photopolymerization degree also improved, requiring less energy to fabricate objects. On the other hand, PEGDA reduced the AESO viscosity, making it compatible with most 3D-printers available on the market.

With the results obtained from the AESO-PEGDA combination, an optimal ratio of both materials was determined. This new resin was used for further research, where this time reinforcement materials were explored to improve its mechanical properties. Micro- and nanocrystalline cellulose were already known by its ability to enhance the mechanical properties of polymers even at small loads. Thus, when they were added to the AESO-PEGDA resin, a gain in tensile strength was observed. However, the same properties that make cellulose crystals improve a material's tensile strength also show to reduce its elongation. Nevertheless, they could be used as a form to tune the mechanical properties of the resin. The addition of fillers did not impact the photopolymerization reaction, nor the curing behavior. Finally, both fillers reduced the resin contact angle (making it more hydrophilic), which literature research demonstrated that it could have a direct correlation with cellular growth.

Despite the investment in the development of new types of bio-photosensitive resins, several challenges still need to be addressed. The first being regarding its inferior mechanical properties. Most vegetable- and plant-based resins have shown low mechanical properties due to network loosening, whereas only a handful of bio resins were able to show similar properties to their petroleum counterparts. Moreover, bio resins also have a higher production cost, which further reduces their usage. Thus, more research is necessary to expand the variety of resins and make them more competitive.

REFERENCES

- [1] S. S. Muthu, M. M. Savalani, **2016**, pp. 1–5.
- [2] S. Ford, T. Minshall, *Addit. Manuf.* **2019**, *25*, 131.
- [3] E. Buehler, N. Comrie, M. Hofmann, S. McDonald, A. Hurst, *ACM Trans. Access. Comput.* **2016**, *8*, 1.
- [4] Grand View Research, *Additive Manufacturing Market Size, Share & Trends Analysis Report By Component, By Printer Type, By Technology, By Software, By Application, By Vertical, By Material, By Region, And Segment Forecasts, 2022 - 2030*, **2021**.
- [5] Grand View Research, *3D Printing Market Size, Share & Trends Analysis Report By Material, By Component (Hardware, Services), By Printer Type (Desktop, Industrial), By Technology, By Software, By Application, By Vertical, And Segment Forecasts, 2020 - 2027*, **2020**.
- [6] C. Zhu, T. Li, M. M. Mohideen, P. Hu, R. Gupta, S. Ramakrishna, Y. Liu, *Polymers (Basel)*. **2021**, *13*, 744.
- [7] A. G. Rodríguez-Hernández, A. Chiodoni, S. Bocchini, R. Vazquez-Duhalt, *Environ. Pollut.* **2020**, *267*, 115609.
- [8] U. N. E. Programme, *FROM POLLUTION TO SOLUTION: A GLOBAL ASSESSMENT OF MARINE LITTER AND PLASTIC POLLUTION*, Nairobi, **2021**.
- [9] S. A. M. Tofail, E. P. Koumoulos, A. Bandyopadhyay, S. Bose, L. O. Donoghue, C. Charitidis, *Mater. Today* **2018**, *21*, 22.
- [10] R. Januszewicz, J. P. Rolland, J. R. Tumbleston, N. Ermoshkin, D. Kelly, A. R. Johnson, R. Pinschmidt, D. Shirvanyants, A. Ermoshkin, J. M. DeSimone, K. Chen, E. T. Samulski, *Science (80-.)*. **2015**, *347*, 1349.
- [11] I. Gibson, D. W. Rosen, B. Stucker, *Addit. Manuf. Technol. Rapid Prototyp. to Direct Digit. Manuf.* **2010**, 1.
- [12] H. Paris, H. Mokhtarian, E. Coatanéa, M. Museau, I. F. Ituarte, *CIRP Ann.* **2016**, *65*, 29.
- [13] K. Markstedt, V. Kuzmenko, I. C. Henriksson, C. de la Peña Vázquez, P. Enoksson, P. Gatenholm, K. M. O. Håkansson, *Adv. Mater. Technol.* **2016**, *1*, 1600096.
- [14] M. Guvendiren, J. Molde, R. M. D. Soares, J. Kohn, *ACS Biomater. Sci. Eng.* **2016**, *2*, 1679.
- [15] B. Berman, *Bus. Horiz.* **2012**, *55*, 155.
- [16] S. Ford, M. Despeisse, *J. Clean. Prod.* **2016**, *137*, 1573.
- [17] M. Attaran, *Bus. Horiz.* **2017**, *60*, 677.
- [18] T. D. Ngo, A. Kashani, G. Imbalzano, K. T. Q. Nguyen, D. Hui, *Compos. Part B Eng.* **2018**, *143*, 172.
- [19] ISO/ASTM 52900, *Additive manufacturing - General principles - Terminology*, Geneva,

- Switzerland, **2018**.
- [20] P. J. Bártolo, Ed., *Stereolithography*, Springer US, Boston, MA, **2011**.
- [21] A. Barkane, O. Platnieks, M. Jurinovs, S. Kasetaitė, J. Ostrauskaite, S. Gaidukovs, Y. Habibi, *Polymers (Basel)*. **2021**, *13*, 1195.
- [22] S. Bechtold, *IIC - Int. Rev. Intellect. Prop. Compet. Law* **2016**, *47*, 517.
- [23] Z. Jiang, B. Diggle, M. L. Tan, J. Viktorova, C. W. Bennett, L. A. Connal, *Adv. Sci.* **2020**, *7*, 2001379.
- [24] M. A. Gibson, N. M. Mykulowycz, J. Shim, R. Fontana, P. Schmitt, A. Roberts, J. Ketkaew, L. Shao, W. Chen, P. Bordeenithikasem, J. S. Myerberg, R. Fulop, M. D. Verminski, E. M. Sachs, Y.-M. Chiang, C. A. Schuh, A. John Hart, J. Schroers, *Mater. Today* **2018**, *21*, 697.
- [25] M. K. Mohan, A. V. Rahul, G. De Schutter, K. Van Tittelboom, *Cem. Concr. Compos.* **2021**, *115*, 103855.
- [26] C. Tan, W. Y. Toh, G. Wong, L. Lin, *Int. J. Bioprinting* **2018**, *4*.
- [27] N. Shahrubudin, T. C. Lee, R. Ramlan, *Procedia Manuf.* **2019**, *35*, 1286.
- [28] I. J. Solomon, P. Sevvel, J. Gunasekaran, *Mater. Today Proc.* **2021**, *37*, 509.
- [29] S. B. Balani, S. H. Ghaffar, M. Chougan, E. Pei, E. Şahin, *Results Eng.* **2021**, *11*, 100257.
- [30] W. L. Ng, J. M. Lee, M. Zhou, Y.-W. Chen, K.-X. A. Lee, W. Y. Yeong, Y.-F. Shen, *Biofabrication* **2020**, *12*, 022001.
- [31] A. Davoudinejad, L. C. Diaz-Perez, D. Quagliotti, D. B. Pedersen, J. A. Albajez-García, J. A. Yagüe-Fabra, G. Tosello, *Procedia CIRP* **2018**, *75*, 98.
- [32] A. Davoudinejad, In *Additive Manufacturing*, Elsevier, **2021**, pp. 159–181.
- [33] R. M. Mahamood, T. C. Jen, S. A. Akinlabi, S. Hassan, K. O. Abdulrahman, E. T. Akinlabi, In *Additive Manufacturing*, Elsevier, **2021**, pp. 107–126.
- [34] D. Dev Singh, T. Mahender, A. Raji Reddy, *Mater. Today Proc.* **2021**, *46*, 350.
- [35] M. Mehrpouya, D. Tuma, T. Vaneker, M. Afrasiabi, M. Bambach, I. Gibson, *Rapid Prototyp. J.* **2022**, *28*, 1.
- [36] R. Velu, D. K. Jayashankar, K. Subburaj, In *Additive Manufacturing*, Elsevier, **2021**, pp. 635–659.
- [37] S. Sun, M. Brandt, M. Easton, In *Laser Additive Manufacturing*, Elsevier, **2017**, pp. 55–77.
- [38] H. P. Le, *J. IMAGING Sci. Technol.* **1998**, *42*, 49.
- [39] I. Karakurt, L. Lin, *Curr. Opin. Chem. Eng.* **2020**, *28*, 134.
- [40] O. Gülcan, K. Günaydın, A. Tamer, *Polymers (Basel)*. **2021**, *13*, 2829.
- [41] A. Jadhav, V. S. Jadhav, *Mater. Today Proc.* **2022**, *62*, 2094.
- [42] M. Ziaee, N. B. Crane, *Addit. Manuf.* **2019**, *28*, 781.
- [43] A. Mostafaei, A. M. Elliott, J. E. Barnes, F. Li, W. Tan, C. L. Cramer, P. Nandwana, M. Chmielus, *Prog. Mater. Sci.* **2021**, *119*, 100707.

- [44] M. Li, W. Du, A. Elwany, Z. Pei, C. Ma, *J. Manuf. Sci. Eng.* **2020**, 142.
- [45] W. Du, X. Ren, C. Ma, Z. Pei, In *Volume 14: Emerging Technologies; Materials: Genetics to Structures; Safety Engineering and Risk Analysis*, American Society of Mechanical Engineers, **2017**.
- [46] M. Molitch-Hou, In *Additive Manufacturing*, Elsevier, **2018**, pp. 1–38.
- [47] I. Gibson, D. Rosen, B. Stucker, *Additive Manufacturing Technologies*, Springer New York, New York, NY, **2015**.
- [48] W. T. Nugroho, Y. Dong, A. Pramanik, In *Composite Materials*, Elsevier, **2021**, pp. 65–115.
- [49] A. Dass, A. Moridi, *Coatings* **2019**, 9, 418.
- [50] D.-G. Ahn, *Int. J. Precis. Eng. Manuf. Technol.* **2021**, 8, 703.
- [51] A. Hehr, M. Norfolk, *Rapid Prototyp. J.* **2019**, 26, 445.
- [52] T. Obikawa, M. Yoshino, J. Shinozuka, *J. Mater. Process. Technol.* **1999**, 89–90, 171.
- [53] T. Singh, S. Kumar, S. Sehgal, *Mater. Today Proc.* **2020**, 28, 1927.
- [54] C. Yu, L. Qie, S. Jing, Y. Yan, *Rapid Prototyp. J.* **2019**, 25, 1647.
- [55] J. M. Dulieu-Barton, M. C. Fulton, *Strain* **2000**, 36, 81.
- [56] N. N. Kumbhar, A. V. Mulay, *J. Inst. Eng. Ser. C* **2018**, 99, 481.
- [57] J. R. C. Dizon, A. H. Espera, Q. Chen, R. C. Advincula, *Addit. Manuf.* **2018**, 20, 44.
- [58] S. A. Skoog, P. L. Goering, R. J. Narayan, *J. Mater. Sci. Mater. Med.* **2014**, 25, 845.
- [59] R. Simič, J. Mandal, K. Zhang, N. D. Spencer, *Soft Matter* **2021**, 17, 6394.
- [60] F. P. W. Melchels, J. Feijen, D. W. Grijpma, *Biomaterials* **2010**, 31, 6121.
- [61] A. Khadilkar, J. Wang, R. Rai, *Int. J. Adv. Manuf. Technol.* **2019**, 102, 2555.
- [62] Y.-M. Huang, C.-P. Jiang, *J. Mater. Process. Technol.* **2005**, 159, 257.
- [63] J. Huang, Q. Qin, J. Wang, *Processes* **2020**, 8, 1138.
- [64] Z. Zhao, X. Tian, X. Song, *J. Mater. Chem. C* **2020**, 8, 13896.
- [65] R. Palucci Rosa, G. Rosace, *Macromol. Mater. Eng.* **2021**, 2100345.
- [66] H. Quan, T. Zhang, H. Xu, S. Luo, J. Nie, X. Zhu, *Bioact. Mater.* **2020**, 5, 110.
- [67] R. Januszewicz, J. R. Tumbleston, A. L. Quintanilla, S. J. Mecham, J. M. DeSimone, *Proc. Natl. Acad. Sci.* **2016**, 113, 11703.
- [68] J. Balli, S. Kumpaty, V. Anewenter, In *Volume 5: Education and Globalization*, American Society of Mechanical Engineers, **2017**.
- [69] M. Emons, K. Obata, T. Binhammer, A. Ovsianikov, B. N. Chichkov, U. Morgner, *Opt. Mater. Express* **2012**, 2, 942.
- [70] A. Ovsianikov, B. N. Chichkov, **2008**, pp. 427–446.
- [71] M. Bass, *Handbook of Optics: Fundamentals, Techniques, and Design* (Ed.: McGraw-Hill Professional), New York, **1994**.

- [72] J. V. Crivello, E. Reichmanis, *Chem. Mater.* **2014**, *26*, 533.
- [73] X. Zheng, W. Smith, J. Jackson, B. Moran, H. Cui, D. Chen, J. Ye, N. Fang, N. Rodriguez, T. Weisgraber, C. M. Spadaccini, *Nat. Mater.* **2016**, *15*, 1100.
- [74] J. Warner, P. Soman, W. Zhu, M. Tom, S. Chen, *ACS Biomater. Sci. Eng.* **2016**, *2*, 1763.
- [75] L. S. S. M. Magalhães, F. E. P. Santos, C. de M. V. Elias, S. Afewerki, G. F. Sousa, A. S. A. Furtado, F. R. Marciano, A. O. Lobo, *J. Funct. Biomater.* **2020**, *11*, 12.
- [76] C. Warr, J. C. Valdoz, B. P. Bickham, C. J. Knight, N. A. Franks, N. Chartrand, P. M. Van Ry, K. A. Christensen, G. P. Nordin, A. D. Cook, *ACS Appl. Bio Mater.* **2020**, *3*, 2239.
- [77] M. Vehse, S. Petersen, K. Sternberg, K.-P. Schmitz, H. Seitz, *Macromol. Symp.* **2014**, *346*, 43.
- [78] T. M. Seck, F. P. W. Melchels, J. Feijen, D. W. Grijpma, *J. Control. Release* **2010**, *148*, 34.
- [79] K. Arcaute, B. Mann, R. Wicker, *Acta Biomater.* **2010**, *6*, 1047.
- [80] A. V. Healy, E. Fuenmayor, P. Doran, L. M. Geever, C. L. Higginbotham, J. G. Lyons, *Pharmaceutics* **2019**, *11*, 645.
- [81] M. Lebedevaite, V. Talacka, J. Ostrauskaite, *J. Appl. Polym. Sci.* **2021**, *138*, 50233.
- [82] B. Steyrer, P. Neubauer, R. Liska, J. Stampfl, *Materials (Basel)*. **2017**, *10*, 1445.
- [83] E. E. Totu, A. C. Nechifor, G. Nechifor, H. Y. Aboul-Enein, C. M. Cristache, *J. Dent.* **2017**, *59*, 68.
- [84] S.-M. Park, J.-M. Park, S.-K. Kim, S.-J. Heo, J.-Y. Koak, *Materials (Basel)*. **2020**, *13*, 3970.
- [85] S. C. Ligon-Auer, M. Schwentenwein, C. Gorsche, J. Stampfl, R. Liska, *Polym. Chem.* **2016**, *7*, 257.
- [86] E. Andrzejewska, *Prog. Polym. Sci.* **2001**, *26*, 605.
- [87] O. D. McNair, A. P. Janisse, D. E. Krzeminski, D. E. Brent, T. E. Gould, J. W. Rawlins, D. A. Savin, *ACS Appl. Mater. Interfaces* **2013**, *5*, 11004.
- [88] A. Oesterreicher, J. Wiener, M. Roth, A. Moser, R. Gmeiner, M. Edler, G. Pinter, T. Griesser, *Polym. Chem.* **2016**, *7*, 5169.
- [89] A. Hoffmann, H. Leonards, N. Tobies, L. Pongratz, K. Kreuels, F. Kreimendahl, C. Apel, M. Wehner, N. Nottrodt, *J. Tissue Eng.* **2017**, *8*, 204173141774448.
- [90] H. Leonards, S. Engelhardt, A. Hoffmann, L. Pongratz, S. Schriever, J. Bläsius, M. Wehner, A. Gillner, (Eds.: Helvajian, H.; Piqué, A.; Wegener, M.; Gu, B.), **2015**, p. 93530F.
- [91] Z. CHERKAoui, P. ESFANDIARI, R. Frantz, J.-J. Lagref, R. Liska, *Stable curable thiol-ene composition*, Parrini, Lorenzo, Switzerland, **2012**, p. 32.
- [92] D. M. Glaser, A. F. Jacobine, P. J. Grabek, *Stabilizer system for thiol-ene and thiol-nene compositions.*, **1995**.
- [93] M. Peerzada, S. Abbasi, K. T. Lau, N. Hameed, *Ind. Eng. Chem. Res.* **2020**, *59*, 6375.
- [94] W.-F. Su, *Principles of Polymer Design and Synthesis*, Vol. 82, Springer Berlin

- Heidelberg, Berlin, **2013**.
- [95] L. Lecamp, B. Youssef, C. Bunel, P. Lebaudy, *Polymer (Guildf)*. **1997**, *38*, 6089.
- [96] J. Zhang, P. Xiao, *Polym. Chem.* **2018**, *9*, 1530.
- [97] H. K. Park, M. Shin, B. Kim, J. W. Park, H. Lee, *NPG Asia Mater.* **2018**, *10*, 82.
- [98] C. T. W. Meereis, F. B. Leal, G. S. Lima, R. V. de Carvalho, E. Piva, F. A. Ogliari, *Dent. Mater.* **2014**, *30*, 945.
- [99] G.-T. Kim, H.-B. Go, J.-H. Yu, S.-Y. Yang, K.-M. Kim, S.-H. Choi, J.-S. Kwon, *Polymers (Basel)*. **2022**, *14*, 979.
- [100] J. Zhang, F. Dumur, P. Xiao, B. Graff, D. Bardelang, D. Gigmes, J. P. Fouassier, J. Lalevée, *Macromolecules* **2015**, *48*, 2054.
- [101] K. S. Lim, B. S. Schon, N. V. Mekhileri, G. C. J. Brown, C. M. Chia, S. Prabakar, G. J. Hooper, T. B. F. Woodfield, *ACS Biomater. Sci. Eng.* **2016**, *2*, 1752.
- [102] A. Al Mousawi, C. Poriel, F. Dumur, J. Toufaily, T. Hamieh, J. P. Fouassier, J. Lalevée, *Macromolecules* **2017**, *50*, 746.
- [103] A. Tursi, *Biofuel Res. J.* **2019**, *6*, 962.
- [104] S. Miao, P. Wang, Z. Su, S. Zhang, *Acta Biomater.* **2014**, *10*, 1692.
- [105] R. Wang, T. P. Schuman, *Express Polym. Lett.* **2012**, *7*, 272.
- [106] S. G. Tan, W. S. Chow, *Polym. - Plast. Technol. Eng.* **2010**, *49*, 1581.
- [107] P. Zhang, J. Zhang, *Green Chem.* **2013**, *15*, 641.
- [108] Y. Su, H. Lin, S. Zhang, Z. Yang, T. Yuan, *Polymers (Basel)*. **2020**, *12*, 1165.
- [109] P. Saithai, J. Lecomte, E. Dubreucq, V. Tanrattanakul, *Express Polym. Lett.* **2013**, *7*, 910.
- [110] D. S. Branciforti, S. Lazzaroni, C. Milanese, M. Castiglioni, F. Auricchio, D. Pasini, D. Dondi, *Addit. Manuf.* **2019**, *25*, 317.
- [111] L. Fertier, H. Koleilat, M. Stemmelen, O. Giani, C. Joly-Duhamel, V. Lapinte, J. J. Robin, *Prog. Polym. Sci.* **2013**, *38*, 932.
- [112] J. T. Sutton, K. Rajan, D. P. Harper, S. C. Chmely, *ACS Appl. Mater. Interfaces* **2018**, *10*, 36456.
- [113] A. W. Bassett, A. E. Honnig, C. M. Breyta, I. C. Dunn, J. J. La Scala, J. F. Stanzione, *ACS Sustain. Chem. Eng.* **2020**, *8*, 5626.
- [114] V. Gold, Ed., *The IUPAC Compendium of Chemical Terminology*, International Union of Pure and Applied Chemistry (IUPAC), Research Triangle Park, NC, **2019**.
- [115] T. P. Haider, C. Völker, J. Kramm, K. Landfester, F. R. Wurm, *Angew. Chemie Int. Ed.* **2019**, *58*, 50.
- [116] V. S. D. Voet, J. Guit, K. Loos, *Macromol. Rapid Commun.* **2021**, *42*, 2000475.
- [117] Y. Luo, G. Le Fer, D. Dean, M. L. Becker, *Biomacromolecules* **2019**, *20*, 1699.
- [118] G. Le Fer, M. L. Becker, *ACS Appl. Mater. Interfaces* **2020**, *12*, 22444.
- [119] F. P. W. Melchels, J. Feijen, D. W. Grijpma, *Biomaterials* **2009**, *30*, 3801.

- [120] A. Ronca, L. Ambrosio, D. W. Grijpma, *Acta Biomater.* **2013**, *9*, 5989.
- [121] L. Elomaa, S. Teixeira, R. Hakala, H. Korhonen, D. W. Grijpma, J. V. Seppälä, *Acta Biomater.* **2011**, *7*, 3850.
- [122] B. J. Green, K. S. Worthington, J. R. Thompson, S. J. Bunn, M. Rethwisch, E. E. Kaalberg, C. Jiao, L. A. Wiley, R. F. Mullins, E. M. Stone, E. H. Sohn, B. A. Tucker, C. A. Guymon, *Biomacromolecules* **2018**, *19*, 3682.
- [123] L. Elomaa, A. Kokkari, T. Närhi, J. V. Seppälä, *Compos. Sci. Technol.* **2013**, *74*, 99.
- [124] S. Schüller-Ravoo, E. Zant, J. Feijen, D. W. Grijpma, *Adv. Healthc. Mater.* **2014**, *3*, 2004.
- [125] T. Brossier, G. Volpi, J. Vasquez-Villegas, N. Petitjean, O. Guillaume, V. Lapinte, S. Blanquer, *Biomacromolecules* **2021**, *22*, 3873.
- [126] B. van Bochove, G. Hannink, P. Buma, D. W. Grijpma, *Macromol. Biosci.* **2016**, *16*, 1853.
- [127] I. Chiulan, E. B. Heggset, Ş. I. Voicu, G. Chinga-Carrasco, *Biomacromolecules* **2021**, *22*, 1795.
- [128] T. Matsuda, M. Mizutani, S. C. Arnold, *Macromolecules* **2000**, *33*, 795.
- [129] T. Kuhnt, R. Marroquín García, S. Camarero-Espinosa, A. Dias, A. T. ten Cate, C. A. van Blitterswijk, L. Moroni, M. B. Baker, *Biomater. Sci.* **2019**, *7*, 4984.
- [130] B. Wu, A. Sufi, R. Ghosh Biswas, A. Hisatsune, V. Moxley-Paquette, P. Ning, R. Soong, A. P. Dicks, A. J. Simpson, *ACS Sustain. Chem. Eng.* **2020**, *8*, 1171.
- [131] C. Guttridge, A. Shannon, A. O'Sullivan, K. J. O'Sullivan, L. W. O'Sullivan, *Ann. 3D Print. Med.* **2022**, *5*, 100044.
- [132] L. Elomaa, E. Keshi, I. M. Sauer, M. Weinhardt, *Mater. Sci. Eng. C* **2020**, *112*, 110958.
- [133] A. M. Salih, M. Bin Ahmad, N. A. Ibrahim, K. Z. HjMohd Dahlan, R. Tajau, M. H. Mahmood, W. M. Z. W. Yunus, *Molecules* **2015**, *20*, 14191.
- [134] J. Guit, M. B. L. Tavares, J. Hul, C. Ye, K. Loos, J. Jager, R. Folkersma, V. S. D. Voet, *ACS Appl. Polym. Mater.* **2020**, *2*, 949.
- [135] Y. Cui, J. Yang, D. Lei, J. Su, *Ind. Eng. Chem. Res.* **2020**, *59*, 11381.
- [136] R. Ding, Y. Du, R. B. Goncalves, L. F. Francis, T. M. Reineke, *Polym. Chem.* **2019**, *10*, 1067.
- [137] O. Jeon, K. H. Bouhadir, J. M. Mansour, E. Alsberg, *Biomaterials* **2009**, *30*, 2724.
- [138] J. Field, J. W. Haycock, F. M. Boissonade, F. Claeysens, *Molecules* **2021**, *26*, 1199.
- [139] E. M. Wilts, A. Gula, C. Davis, N. Chartrain, C. B. Williams, T. E. Long, *Eur. Polym. J.* **2020**, *130*, 109693.
- [140] FAO, *Vegetable oil production, World*, **2019**.
- [141] Y. LI, E. GRIFFING, M. HIGGINS, M. OVERCASH, *J. Food Process Eng.* **2006**, *29*, 429.
- [142] USDA, *Oilseeds: World Markets and Trade*, **2021**.
- [143] B. P. Lamsal, P. A. Murphy, L. A. Johnson, *J. Am. Oil Chem. Soc.* **2006**, *83*, 973.
- [144] M.-H. Cheng, J. J. K. Sekhon, K. A. Rosentrater, T. Wang, S. Jung, L. A. Johnson, *Food*

- Bioprod. Process.* **2018**, *108*, 58.
- [145] Q. Wu, Y. Hu, J. Tang, J. Zhang, C. Wang, Q. Shang, G. Feng, C. Liu, Y. Zhou, W. Lei, *ACS Sustain. Chem. Eng.* **2018**, *6*, 8340.
- [146] E. Skliutas, M. Lebedevaite, S. Kasetaitė, S. Reikšytė, S. Lileikis, J. Ostrauskaite, M. Malinauskas, *Sci. Rep.* **2020**, *10*, 9758.
- [147] S. Miao, W. Zhu, N. J. Castro, M. Nowicki, X. Zhou, H. Cui, J. P. Fisher, L. G. Zhang, *Sci. Rep.* **2016**, *6*, 27226.
- [148] R. Palucci Rosa, G. Rosace, R. Arrigo, G. Malucelli, *Polymers (Basel)*. **2022**, *14*, 1886.
- [149] X. Yang, S. Li, J. Xia, J. Song, K. Huang, M. Li, *BioResources* **2015**, *10*.
- [150] R. Liu, J. Zhu, J. Luo, X. Liu, *Prog. Org. Coatings* **2014**, *77*, 30.
- [151] S. Grauzeliene, D. Valaityte, G. Motiekaityte, J. Ostrauskaite, *Materials (Basel)*. **2021**, *14*, 2675.
- [152] K. Zhang, C. Xie, G. Wang, R. He, G. Ding, M. Wang, D. Dai, D. Fang, *Ceram. Int.* **2019**, *45*, 203.
- [153] S. Y. Song, M. S. Park, D. Lee, J. W. Lee, J. S. Yun, *Mater. Des.* **2019**, *180*, 107960.
- [154] J. Bennett, *Addit. Manuf.* **2017**, *18*, 203.
- [155] S. Zakeri, M. Vippola, E. Levänen, *Addit. Manuf.* **2020**, *35*, 101177.
- [156] A. Mitchell, U. Lafont, M. Hołyńska, C. Semprimoschnig, *Addit. Manuf.* **2018**, *24*, 606.
- [157] L. Lebreton, A. Andrady, *Palgrave Commun.* **2019**, *5*, 6.
- [158] OECD, *Plastic pollution is growing relentlessly as waste management and recycling fall short*, **2022**.
- [159] Greenpeace, *Plastic Recycling Is A Dead-End Street—Year After Year, Plastic Recycling Declines Even as Plastic Waste Increases*, **2022**.
- [160] S. Dahiya, R. Katakojwala, S. Ramakrishna, S. V. Mohan, *Mater. Circ. Econ.* **2020**, *2*, 7.
- [161] Y. Xia, R. C. Larock, *Green Chem.* **2010**, *12*, 1893.
- [162] Y. H. Lin, K. H. Liao, N. K. Chou, S. S. Wang, S. H. Chu, K. H. Hsieh, *Eur. Polym. J.* **2008**, *44*, 2927.
- [163] D. S. Tathe, R. N. Jagtap, *J. Coatings Technol. Res.* **2015**, *12*, 187.
- [164] C. Li, H. Xiao, X. Wang, T. Zhao, *J. Clean. Prod.* **2018**, *180*, 272.
- [165] Z. Jiao, X. Wang, Q. Yang, C. Wang, *Polym. Bull.* **2017**, *74*, 2497.
- [166] V. Jančovičová, M. Mikula, B. Havlínová, Z. Jakubíková, *Prog. Org. Coatings* **2013**, *76*, 432.
- [167] A. Barkane, O. Platnieks, M. Jurinovs, S. Gaidukovs, *Polym. Degrad. Stab.* **2020**, *181*, 109347.
- [168] Z. Weng, Y. Zhou, W. Lin, T. Senthil, L. Wu, *Compos. Part A Appl. Sci. Manuf.* **2016**, *88*, 234.
- [169] P. Dijkstra, M. Tietema, R. Folkersma, V. S. D. Voet, T. Strating, K. Loos, A. J. J.

- Woortman, G. H. M. Schnelting, J. Jager, J. Xu, *ACS Omega* **2018**, *3*, 1403.
- [170] E. Skliutas, S. Kasetaitė, L. Jonušauskas, J. Ostrauskaite, M. Malinauskas, *Opt. Eng.* **2018**, *57*, 1.
- [171] S.-J. Park, F.-L. Jin, J.-R. Lee, *Mater. Sci. Eng. A* **2004**, *374*, 109.
- [172] P. Hiemenz, T. Lodge, *Polymer chemistry*, **2007**.
- [173] C. Zhang, M. Yan, E. W. Cochran, M. R. Kessler, *Mater. Today Commun.* **2015**, *5*, 18.
- [174] K. P. Menard, *Dynamic Mechanical Analysis*, CRC Press, **2008**.
- [175] N. B. Palaganas, J. D. Mangadlao, A. C. C. De Leon, J. O. Palaganas, K. D. Pangilinan, Y. J. Lee, R. C. Advincula, *ACS Appl. Mater. Interfaces* **2017**, *9*, 34314.
- [176] A. S. Hoffman, *Adv. Drug Deliv. Rev.* **2002**, *54*, 3.
- [177] IUPAC, *Swelling definition*.
- [178] A. Sienkiewicz, P. Krasucka, B. Charnas, W. Stefaniak, J. Goworek, *J. Therm. Anal. Calorim.* **2017**, *130*, 85.
- [179] R. A. Omer, A. Hughes, J. R. Hama, W. Wang, H. Tai, *J. Appl. Polym. Sci.* **2015**, *132*, n/a.
- [180] W. Liu, M. Fei, Y. Ban, A. Jia, R. Qiu, *Polymers (Basel)*. **2017**, *9*, 541.
- [181] Y. Li, Q. Mao, J. Yin, Y. Wang, J. Fu, Y. Huang, *Addit. Manuf.* **2021**, *37*, 101716.
- [182] A. Licciulli, C. Esposito Corcione, A. Greco, V. Amicarelli, A. Maffezzoli, *J. Eur. Ceram. Soc.* **2005**, *25*, 1581.
- [183] S. Kasetaitė, S. De la Flor, A. Serra, J. Ostrauskaite, *Polymers (Basel)*. **2018**, *10*, 439.
- [184] R. A. Sheldon, M. Norton, *Green Chem.* **2020**, *22*, 6310.
- [185] E. Bioplastic, *Bioplastics market data*, **2022**.
- [186] M. Maturi, C. Pulignani, E. Locatelli, V. Vetri Buratti, S. Tortorella, L. Sambri, M. Comes Franchini, *Green Chem.* **2020**, *22*, 6212.
- [187] D. Kunwong, N. Sumanochitraporn, S. Kaewpirom, *Songklanakarin J. Sci. Technol.* **2011**, *33*, 201.
- [188] H. Pelletier, N. Belgacem, A. Gandini, *J. Appl. Polym. Sci.* **2006**, *99*, 3218.
- [189] Z. Yang, H. Peng, W. Wang, T. Liu, *J. Appl. Polym. Sci.* **2010**, *116*, 2658.
- [190] I. K. Cingesar, M.-P. Marković, D. Vrsaljko, *Addit. Manuf.* **2022**, *55*, 102813.
- [191] A. R. M. Martins, I. D. Silva, L. Machado-Santos, R. P. Vitti, M. A. C. Sinhoreti, W. C. Brandt, *J. Appl. Polym. Sci.* **2021**, *138*, 50498.
- [192] T. E. of E. Britannica, *Young's modulus*, **2022**.
- [193] F.-L. Jin, S.-J. Park, *Mater. Sci. Eng. A* **2008**, *478*, 402.
- [194] G. Rosace, R. Palucci Rosa, R. Arrigo, G. Malucelli, *J. Appl. Polym. Sci.* **2021**, *138*, 51292.
- [195] K. S. Anseth, M. D. Goodner, M. A. Reil, A. R. Kannurpatti, S. M. Newman, C. N. Bowman, *J. Dent. Res.* **1996**, *75*, 1607.

- [196] P. Tack, J. Victor, P. Gemmel, L. Annemans, *Biomed. Eng. Online* **2016**, *15*, 115.
- [197] G. Taormina, C. Sciancalepore, M. Messori, F. Bondioli, *J. Appl. Biomater. Funct. Mater.* **2018**, *16*, 151.
- [198] S. C. Ligon, R. Liska, J. Stampfl, M. Gurr, R. Mülhaupt, *Chem. Rev.* **2017**, *117*, 10212.
- [199] M. Salmi, *Materials (Basel)*. **2021**, *14*, 191.
- [200] M. Javaid, A. Haleem, *J. Clin. Orthop. Trauma* **2018**, *9*, 202.
- [201] M. Patel, Z. Al-Momani, N. Hodson, P. J. Nixon, D. Mitchell, *Dent. Update* **2013**, *40*, 564.
- [202] F. Baino, G. Magnaterra, E. Fiume, A. Schiavi, L. Tofan, M. Schwentenwein, E. Verné, *J. Am. Ceram. Soc.* **2022**, *105*, 1648.
- [203] J. P. Vacanti, R. Langer, *Lancet* **1999**, *354*, S32.
- [204] A. Carnicer-Lombarte, S.-T. Chen, G. G. Malliaras, D. G. Barone, *Front. Bioeng. Biotechnol.* **2021**, *9*.
- [205] S. A. Schoonraad, K. M. Fischenich, K. N. Eckstein, V. Crespo-Cuevas, L. M. Savard, A. Muralidharan, A. A. Tomaschke, A. C. Uzcategui, M. A. Randolph, R. R. McLeod, V. L. Ferguson, S. J. Bryant, *Biofabrication* **2021**, *13*, 044106.
- [206] H.-Y. Cheung, K.-T. Lau, T.-P. Lu, D. Hui, *Compos. Part B Eng.* **2007**, *38*, 291.
- [207] I. M. El-Sherbiny, M. H. Yacoub, *Glob. Cardiol. Sci. Pract.* **2013**, *2013*, 38.
- [208] J.-M. Lü, X. Wang, C. Marin-Muller, H. Wang, P. H. Lin, Q. Yao, C. Chen, *Expert Rev. Mol. Diagn.* **2009**, *9*, 325.
- [209] J. Gong, Y. Qian, K. Lu, Z. Zhu, L. Siow, C. Zhang, S. Zhou, T. Gu, J. Yin, M. Yu, H. Wang, H. Yang, *Biomed. Mater.* **2022**, *17*, 062004.
- [210] M. Hassan, K. Dave, R. Chandrawati, F. Dehghani, V. G. Gomes, *Eur. Polym. J.* **2019**, *121*, 109340.
- [211] T. Serra, M. Ortiz-Hernandez, E. Engel, J. A. Planell, M. Navarro, *Mater. Sci. Eng. C* **2014**, *38*, 55.
- [212] Z. Wang, R. Abdulla, B. Parker, R. Samanipour, S. Ghosh, K. Kim, *Biofabrication* **2015**, *7*, 045009.
- [213] R. Mau, J. Nazir, S. John, H. Seitz, *Curr. Dir. Biomed. Eng.* **2019**, *5*, 249.
- [214] F. Della Sala, M. Biondi, D. Guarnieri, A. Borzacchiello, L. Ambrosio, L. Mayol, *J. Mech. Behav. Biomed. Mater.* **2020**, *110*, 103885.
- [215] D. Mondal, A. Srinivasan, P. Comeau, Y.-C. Toh, T. L. Willett, *Mater. Sci. Eng. C* **2021**, *118*, 111400.
- [216] J. . Stansbury, S. . Dickens, *Dent. Mater.* **2001**, *17*, 71.
- [217] C. Decker, L. Keller, K. Zahouily, S. Benfarhi, *Polymer (Guildf)*. **2005**, *46*, 6640.
- [218] N. Auclair, A. Kaboorani, B. Riedl, V. Landry, *Ind. Crops Prod.* **2015**, *76*, 530.
- [219] C. M. González-Henríquez, G. del C. Pizarro, M. A. Sarabia-Vallejos, C. A. Terraza, Z. E. López-Cabaña, *Arab. J. Chem.* **2019**, *12*, 1413.

- [220] R. L. dos Santos, G. A. de M. Sampaio, F. G. de Carvalho, M. M. Pithon, G. M. T. Guênes, P. M. Alves, *J. Adhes. Dent.* **2014**, *16*, 15.
- [221] J. Yang, C. R. Han, J. F. Duan, F. Xu, R. C. Sun, *ACS Appl. Mater. Interfaces* **2013**, *5*, 3199.
- [222] D. R. H. Jones, In *Engineering Materials 1: An Introduction to Properties, Applications and Design*, **2019**, pp. 31–47.
- [223] Y. Yuan, M. P. Hays, P. R. Hardwidge, J. Kim, *RSC Adv.* **2017**, *7*, 14254.
- [224] T. Zhao, H. Zhang, D. Zhou, Y. Gao, Y. Dong, U. Greiser, H. Tai, W. Wang, *RSC Adv.* **2015**, *5*, 33823.
- [225] S. Necchi, D. Molina, S. Turri, F. Rossetto, M. Rietjens, G. Pennati, *J. Mech. Behav. Biomed. Mater.* **2011**, *4*, 2002.
- [226] J. Z. Manapat, Q. Chen, P. Ye, R. C. Advincula, *Macromol. Mater. Eng.* **2017**, *302*, 1.
- [227] N. Strambeanu, L. Demetrovici, D. Dragos, M. Lungu, In *Nanoparticles' Promises and Risks*, Springer International Publishing, Cham, **2015**, pp. 3–8.
- [228] B. Mishra, J. Singh, In *Targeting Chronic Inflammatory Lung Diseases Using Advanced Drug Delivery Systems*, Elsevier, **2020**, pp. 57–95.
- [229] H. Eng, S. Maleksaeedi, S. Yu, Y. Y. C. Choong, F. E. Wiria, C. L. C. Tan, P. C. Su, J. Wei, *Procedia Eng.* **2017**, *216*, 1.
- [230] E. P. Koumoulos, E. Gkartzou, C. A. Charitidis, *Manuf. Rev.* **2017**, *4*, 12.
- [231] M. Gurr, D. Hofmann, M. Ehm, Y. Thomann, R. Kubier, R. Mülhaupt, *Adv. Funct. Mater.* **2008**, *18*, 2390.
- [232] D. Lin, S. Jin, F. Zhang, C. Wang, Y. Wang, C. Zhou, G. J. Cheng, *Nanotechnology* **2015**, *26*, 434003.
- [233] H. Eng, S. Maleksaeedi, S. Yu, Y. Y. C. Choong, F. E. Wiria, R. E. Kheng, J. Wei, P.-C. Su, H. P. Tham, *Rapid Prototyp. J.* **2017**, *23*, 129.
- [234] M. N. dos Santos, C. V. Opelt, F. H. Lafratta, C. M. Lepienski, S. H. Pezzin, L. A. F. Coelho, *Mater. Sci. Eng. A* **2011**, *528*, 4318.
- [235] J. Z. Manapat, J. D. Mangadlao, B. D. B. Tiu, G. C. Tritchler, R. C. Advincula, *ACS Appl. Mater. Interfaces* **2017**, *9*, 10085.
- [236] L. Dai, T. Cheng, C. Duan, W. Zhao, W. Zhang, X. Zou, J. Aspler, Y. Ni, *Carbohydr. Polym.* **2019**, *203*, 71.
- [237] H. Liu, J. Mo, *J. Reinf. Plast. Compos.* **2010**, *29*, 909.
- [238] T. Chartier, A. Badev, Y. Abouliatim, P. Lebaudy, L. Lecamp, *J. Eur. Ceram. Soc.* **2012**, *32*, 1625.
- [239] M. Wozniak, T. Graule, Y. de Hazan, D. Kata, J. Lis, *J. Eur. Ceram. Soc.* **2009**, *29*, 2259.
- [240] P. Cai, L. Guo, H. Wang, J. Li, J. Li, Y. Qiu, Q. Zhang, Q. Lue, *Ceram. Int.* **2020**, *46*, 16833.
- [241] J. W. Lee, I. H. Lee, D.-W. Cho, *Microelectron. Eng.* **2006**, *83*, 1253.
- [242] J. Sun, Y. T. Park, Y. Hun, J. Jeong, H. Cho, *Appl. Phys. A* **2016**, *122*, 1.

- [243] I. Cooperstein, M. Layani, S. Magdassi, *J. Mater. Chem. C* **2015**, *3*, 2040.
- [244] E. S. Schwahn, Using Controlled Curing in a Custom Stereolithography-based 3D Printing Machine to Obtain Graded Property Variations, University of Nebraska, **2015**.
- [245] C. Liu, B. Qian, X. Liu, L. Tong, J. Qiu, *RSC Adv.* **2018**, *8*, 16344.
- [246] R. He, W. Liu, Z. Wu, D. An, M. Huang, H. Wu, Q. Jiang, X. Ji, S. Wu, Z. Xie, *Ceram. Int.* **2018**, *44*, 3412.
- [247] S. Mubarak, D. Dhamodharan, N. Divakaran, M. B. Kale, T. Senthil, L. Wu, J. Wang, *Nanomaterials* **2020**, *10*, 79.
- [248] S. Ghoshal, *Fibers* **2017**, *5*, 40.
- [249] G. Rosace, V. Trovato, C. Colleoni, M. Caldara, V. Re, M. Brucale, E. Piperopoulos, E. Mastronardo, C. Milone, G. De Luca, M. R. Plutino, *Sensors Actuators B Chem.* **2017**, *252*, 428.
- [250] J. H. Sandoval, R. B. Wicker, *Rapid Prototyp. J.* **2006**, *12*, 292.
- [251] S. K. Soni, B. Thomas, V. R. Kar, *Mater. Today Commun.* **2020**, *25*, 101546.
- [252] Y. Zhang, H. Li, X. Yang, T. Zhang, K. Zhu, W. Si, Z. Liu, H. Sun, *Polym. Compos.* **2018**, *39*, E671.
- [253] U. Staudinger, G. Zyla, B. Krause, A. Janke, D. Fischer, C. Esen, B. Voit, A. Ostendorf, *Microelectron. Eng.* **2017**, *179*, 48.
- [254] G. Gonzalez, A. Chiappone, I. Roppolo, E. Fantino, V. Bertana, F. Perrucci, L. Scaltrito, F. Pirri, M. Sangermano, *Polymer (Guildf).* **2017**, *109*, 246.
- [255] S. Laske, Ed., *Polymer Nanoclay Composites*, 1st Editio., **2015**.
- [256] H. Eng, S. Maleksaeedi, S. Yu, Y. Y. C. Choong, F. E. Wiria, C. L. C. Tan, P. C. Su, J. Wei, *Procedia Eng.* **2017**, *216*, 1.
- [257] G. Allen Brady, J. W. Halloran, *Rapid Prototyp. J.* **1997**, *3*, 61.
- [258] J. W. Halloran, V. Tomeckova, S. Gentry, S. Das, P. Cilino, D. Yuan, R. Guo, A. Rudraraju, P. Shao, T. Wu, T. R. Alabi, W. Baker, D. Legdzina, D. Wolski, W. R. Zimbeck, D. Long, *J. Eur. Ceram. Soc.* **2011**, *31*, 2613.
- [259] J. W. Halloran, *Annu. Rev. Mater. Res.* **2016**, *46*, 19.
- [260] M. L. Griffith, J. W. Halloran, *J. Am. Ceram. Soc.* **1996**, *79*, 2601.
- [261] H. Xing, B. Zou, S. Li, X. Fu, *Ceram. Int.* **2017**, *43*, 16340.
- [262] K. Zhang, K. Wei, J. Chen, B. Liang, D. Fang, R. He, *J. Eur. Ceram. Soc.* **2021**, *41*, 2796.
- [263] K. Zhang, R. He, G. Ding, X. Bai, D. Fang, *Ceram. Int.* **2021**, *47*, 2303.
- [264] G. Ding, R. He, K. Zhang, N. Zhou, H. Xu, *Ceram. Int.* **2020**, *46*, 18785.
- [265] E. MacDonald, R. Salas, D. Espalin, M. Perez, E. Aguilera, D. Muse, R. B. Wicker, *IEEE Access* **2014**, *2*, 234.
- [266] R. Clasen, *Key Eng. Mater.* **2001**, 206–213, 235.
- [267] N. J. Castro, J. O'Brien, L. G. Zhang, *Nanoscale* **2015**, *7*, 14010.

- [268] O. Guillaume, M. A. Geven, C. M. Sprecher, V. A. Stadelmann, D. W. Grijpma, T. T. Tang, L. Qin, Y. Lai, M. Alini, J. D. de Bruijn, H. Yuan, R. G. Richards, D. Eglin, *Acta Biomater.* **2017**, *54*, 386.
- [269] F. Li, S. Zhou, L. Wu, *J. Appl. Polym. Sci.* **2005**, *98*, 1119.
- [270] S.-H. Chiu, D.-C. Wu, *J. Appl. Polym. Sci.* **2008**, *107*, 3529.
- [271] C. Zhang, Y. Cui, J. Li, D. Jiang, *J. Appl. Polym. Sci.* **2015**, *132*, 42307.
- [272] F. B. Löffler, E. C. Bucharsky, K. G. Schell, S. Heißler, M. J. Hoffmann, *J. Eur. Ceram. Soc.* **2020**, *40*, 4556.
- [273] S.-B. Kim, N.-H. Kim, J.-H. Kim, H.-S. Moon, *J. Prosthet. Dent.* **2018**, *120*, 693.
- [274] P. J. Bartolo, J. Gaspar, *CIRP Ann.* **2008**, *57*, 235.
- [275] T. Moritz, S. Maleksaeedi, In *Additive Manufacturing*, Elsevier, **2018**, pp. 105–161.
- [276] V. Tomeckova, J. W. Halloran, *J. Eur. Ceram. Soc.* **2010**, *30*, 3023.
- [277] C. Sciancalepore, F. Moroni, M. Messori, F. Bondioli, *Compos. Commun.* **2017**, *6*, 11.
- [278] E. Fantino, A. Chiappone, F. Calignano, M. Fontana, F. Pirri, I. Roppolo, *Materials (Basel)*. **2016**, *9*, 21.
- [279] D. Klemm, B. Heublein, H.-P. Fink, A. Bohn, *Angew. Chemie Int. Ed.* **2005**, *44*, 3358.
- [280] A. Carlmark, E. Larsson, E. Malmström, *Eur. Polym. J.* **2012**, *48*, 1646.
- [281] O. Korhonen, A. H. Hamzaoui, T. Budtova, M. Zrida, K. Labidi, *Ind. Crops Prod.* **2018**, *127*, 135.
- [282] A. Naseem, S. Tabasum, K. M. Zia, M. Zuber, M. Ali, A. Noreen, *Int. J. Biol. Macromol.* **2016**, *93*, 296.
- [283] A. Chakrabarty, Y. Teramoto, *Polymers (Basel)*. **2018**, *10*, 517.
- [284] J. Liu, L. Sun, W. Xu, Q. Wang, S. Yu, J. Sun, *Carbohydr. Polym.* **2019**, *207*, 297.
- [285] Y. Shao, C. Guizani, P. Grosseau, D. Chaussy, D. Beneventi, *Compos. Part B* **2018**, *149*, 206.
- [286] G. Siqueira, J. Bras, A. Dufresne, **2010**, 728.
- [287] A. C. de Leon, Q. Chen, N. B. Palaganas, J. O. Palaganas, J. Manapat, R. C. Advincula, *React. Funct. Polym.* **2016**, *103*, 141.
- [288] Q. Wang, C. Ji, L. Sun, J. Sun, J. Liu, *Molecules* **2020**, *25*, 2319.
- [289] J. Yang, X. An, L. Liu, S. Tang, H. Cao, Q. Xu, H. Liu, *Carbohydr. Polym.* **2020**, *250*, 116881.
- [290] J. Dong, M. Li, L. Zhou, S. Lee, C. Mei, X. Xu, Q. Wu, *J. Polym. Sci. Part B Polym. Phys.* **2017**, *55*, 847.
- [291] E. Skliutas, S. Kašėtaitė, G. Grigalevičiūtė, L. Jonušauskas, S. Rekštytė, J. Ostrauskaitė, M. Malinauskas, In *Proc SPIE* (Eds.: Freymann, G. von; Schoenfeld, W. V.; Rumpf, R. C.), **2017**, p. 1011514.
- [292] H.-W. Kang, J.-W. Rhie, D.-W. Cho, *Microelectron. Eng.* **2009**, *86*, 941.

-
- [293] L. Wågberg, G. Decher, M. Norgren, T. Lindström, M. Ankerfors, K. Axnäs, *Langmuir* **2008**, *24*, 784.
- [294] A. Isogai, T. Saito, H. Fukuzumi, *Nanoscale* **2011**, *3*, 71.
- [295] N. Lavoine, I. Desloges, A. Dufresne, J. Bras, *Carbohydr. Polym.* **2012**, *90*, 735.
- [296] R. Z. Khoo, H. Ismail, W. S. Chow, *Procedia Chem.* **2016**, *19*, 788.
- [297] H. Kargarzadeh, J. Huang, N. Lin, I. Ahmad, M. Mariano, A. Dufresne, S. Thomas, A. Gałęski, *Prog. Polym. Sci.* **2018**, *87*, 197.
- [298] S. Kumar, M. Hofmann, B. Steinmann, E. J. Foster, C. Weder, *ACS Appl. Mater. Interfaces* **2012**, *4*, 5399.
- [299] X. Feng, Z. Yang, S. Chmely, Q. Wang, S. Wang, Y. Xie, *Carbohydr. Polym.* **2017**, *169*, 272.
- [300] P. Robert J., B. Lennart, *Surface and Colloid Chemistry in Advanced Ceramics Processing* (Eds.: Pugh, R. J.; Bergstrom, L.), 12th ed., CRC Press, **2017**.
- [301] S. Meng, H. He, Y. Jia, P. Yu, B. Huang, J. Chen, *J. Appl. Polym. Sci.* **2017**, *134*, 1.
- [302] F. Scalera, C. E. Corcione, F. Montagna, A. Sannino, A. Maffezzoli, *Ceram. Int.* **2014**, *40*, 15455.
- [303] F. A. dos Santos, G. C. V. Iulianelli, M. I. B. Tavares, *Polym. Test.* **2017**, *61*, 280.
- [304] F. A. dos Santos, G. C. Valle Iulianelli, M. I. Bruno Tavares, *Polym. Eng. Sci.* **2017**, *57*, 464.
- [305] J. M. Dulieu-Barton, M. C. Fulton, *Strain* **2000**, *36*, 81.
- [306] G. Fei, C. Parra-Cabrera, K. Zhong, M. L. Tietze, K. Clays, R. Ameloot, *ACS Appl. Polym. Mater.* **2021**, *3*, 6705.

LIST OF TABLES

Table 1: Advantages and disadvantages of the seven AM technologies.	17
Table 2: Name, chemical structure, molecular weight and wavelength of popular photoinitiators.	35
Table 3: Biobased, biocompatible, and biodegradable photosensitive materials for stereolithography 3D-printing.	47
Table 4: Mechanical properties of various popular commercial resins.	67
Table 5: Photopolymerization conversion degree of PY/AESO mixtures.....	74
Table 6: Thermogravimetric data for the different UV-cured systems.	81
Table 7: Depth penetration (D_p) and critical energy (E_c) for different commercial resins.	86
Table 8: Depth penetration (D_p) and critical energy (E_c) calculated as a function of AESO loadings.....	86
Table 9: Sample code, composition, and bio-content (BC) of each PEGDA/AESO mixture.	94
Table 10: Double-bond conversion at 810, 910 and 1620-1640 cm^{-1} for IBOMA, AESO, and their mixtures.	97
Table 11: Comparison of the mechanical behavior of I.A.50:50 with some common 3D-printing commercial resins.....	101
Table 12: Thermogravimetric data for the IBOMA and AESO mixtures.....	104
Table 13: Depth penetration (D_p) and critical energy (E_c) calculated as a function of IBOMA and AESO ratios.....	106
Table 14: Sample code, composition, and bio-content (BC) of each PEGDA/AESO mixture.	113
Table 15: Double-bond conversion at 810 cm^{-1} for PEGDA, AESO, and their mixtures.	117

Table 16: Thermogravimetric data for the different AESO/PEGDA ratios (w/w).	123
Table 17: Depth penetration (D_p) and critical energy (E_c) as a function of AESO loadings. Statistical analyses were performed using Pearson's correlation with $p < 0.05$.	127
Table 18: P.A.20:80 photopolymerization conversion in the presence of different loadings of MCCs and CNCs.	141
Table 19: Different types of fillers and their impact on viscosity.	143
Table 20: Complex viscosity values of the UV-curable systems as a function of the filler loading in P.A.20:80.	144
Table 21: Thermogravimetric data for MCCs-based composites.....	150
Table 22: Thermogravimetric data for CNCs-based composites.....	151
Table 23: Contact angle values using water for P.A.20:80 and its composites containing MCCs or CNCs. Statistical analyses were performed using Pearson's correlation for MCC and CNC with $p < 0.05$.....	153
Table 24: Changes in E_c and D_p with the addition of different types of fillers.	154
Table 25: Depth penetration (D_p) and critical energy (E_c) as a function of MCCs and CNCs loadings. Statistical analyses were performed using Pearson's correlation for MCC and CNC with $p < 0.05$.	155

LIST OF FIGURES

Figure 1. The seven types of additive manufacturing technologies and some of their processes according to the ISO/ASTM 52900.^[19].....	7
Figure 2: Schematic diagrams of two material extrusion technologies: (a) fused deposition modeling and (b) direct writing.	9
Figure 3: Visual representation of “top-down” vat photopolymerization process.....	10
Figure 4: Representation of a power bed fusion machine using a computer aided laser to select melt the particles together on the build platform.	12
Figure 5: Material jetting 3D-printer using droplets of liquids (photopolymer and support material) and an UV light lamp to fabricate a 3D object.	13
Figure 6: Description of a binder jetting 3D process. Droplets of a liquid binder is used to glue the particles together forming an object.	14
Figure 7: Direct energy deposition using an articulated robotic arm and a powerful laser beam to melt powder or thin filaments of metal on a surface.	16
Figure 8: Description of the sheet lamination technique.	17
Figure 9: Schematics of a “bottom-up” stereolithography printer.....	21
Figure 10: Description of the mechanisms behind a digital light processing 3D printer....	22
Figure 11: Visual representation of the interior of an LCD-DLP.....	23
Figure 12: Using an oxygen-permeable membrane CLIP machines can control the photopolymerization reaction.	24
Figure 13: Schematic description of a 2PP process. By using a near-infrared laser (700 – 800 nm), the light can pass through the surface of the photosensitive material and will only react at the point where the two photons intersect.	25
Figure 14: The five types of photopolymerization reaction.....	26

Figure 15: Chemical structure of commonly used acrylates monomers for developing SL resins.....	28
Figure 16: Chemical structure of thiol-ene and thiol-yne monomers for developing SL resins.....	30
Figure 17: Chemical structure of epoxy monomers for developing SL resins.....	31
Figure 18: (Meth)acrylate modification of vegetable oil.....	42
Figure 19: Epoxy modification of vegetable oil.	43
Figure 20: PEGDA polymeric structure modification by grafting or addition techniques.	45
Figure 21: Acrylated epoxidized soybean oil structure.	51
Figure 22: The 3D model used to determine the resin curing characteristics.	62
Figure 23: ATR-FTIR analysis of PY_{AESO50} with and without TPO and PY_{AESO} at different types of post treatment process in the range of 840 – 800 cm⁻¹. The tested samples were post-cured for 40 min (20 min each side) under UV light.....	71
Figure 24: Infrared spectra under attenuated total reflectance of PY resin with different AESO concentrations (increasing from 10 to 50 wt.%). Only the sample PY_{uncured} was analyzed before being photopolymerized, the rest was after being 3D-printed and post-cured.....	75
Figure 25: PY resin viscosity variation with increasing AESO loads (viscosity curves of pure PY and AESO are also included).....	77
Figure 26: Tensile strength comparison between Peopoly moai standard with 20 wt.% AESO and different types of commercial resins.....	78
Figure 27: Variation of the tensile strength (gray bars) and elongation (red squares) as a function of AESO loadings. Statistical analysis for the elongation at break was done using a one-way analysis of variance (ANOVA) with the level of significance set at p < 0.05.....	79
Figure 28: Fracture energy for 3D-printed samples with different AESO loadings.....	80
Figure 29: Variation of the Young's modulus with increasing concentrations of AESO. ..	81

Figure 30: Water contact angle measurements of 3D-printed samples with different AESO loadings. Statistical analysis for the contact angle was carried out using a one-way analysis of variance (ANOVA) with the level of significance set at probabilities of $p < 0.05$.	83
Figure 31: Swelling behavior of 3D-printed parts with different AESO loadings, after 5, 10, 20 and 30 days of immersion in water.	85
Figure 32: Working curve for Peopoly Clear, AESO and their mixtures.....	87
Figure 33: Digital images of the boat prototypes (48 x 24.8 x 38.4 mm) printed with different AESO concentrations. Boat A was printed with pure Peopoly resin and boats B and C with 10 and 50 wt.% of AESO mixed in it. The images A*, B* and C* are close-ups of their respective counterparts.....	88
Figure 34: 2021 global production of bioplastics. Data retrieved from European Bioplastic.^[185]	92
Figure 35: ATR-FTIR spectra of AESO, IBOMA and their combinations. Samples I_{unc} and A_{unc} are relative to the uncured IBOMA and AESO resin, respectively. The other samples were post-cured under UV-light for 40 min (20min each side).....	95
Figure 36: Viscosity variation with increasing AESO concentration.	99
Figure 37: Samples tensile strength and elongation variation as a function of AESO loads.	100
Figure 38: Fracture energy of the samples having different AESO concentration.....	102
Figure 39: Young's modulus of the samples with varying loads of AESO.....	103
Figure 40: Change in the samples contact angle in relationship to the AESO weight percentage.	104
Figure 41: IBOMA, AESO and their respective combinations working curve.	107
Figure 42: Infrared spectra using attenuated total reflectance of PEGDA with increasing AESO concentrations (from 50 to 90 wt.%). The samples PEGDA_{unc} and AESO_{unc} are the non-cured versions of PEGDA and AESO, respectively. The others samples described in the figure were cured for 40 min (20 min each side) under UV light.....	115

Figure 43: PEGDA viscosity variation with increasing AESO concentrations.	118
Figure 44: Variation of the tensile strength and elongation as a function of AESO loading. Statistical analysis for the elongation at break was performed using a one-way analysis of variance (ANOVA) with the level of significance set at probabilities of $p < 0.05$.	120
Figure 45: Young’s modulus for various PEGDA/AESO ratios.	121
Figure 46: Fracture energy change according to the AESO concentration.	122
Figure 47: Water contact angle measurements of 3D-printed samples with different AESO concentrations. Statistical analysis for the contact angle was carried out using a one-way analysis of variance (ANOVA) with the level of significance set at probabilities of $p < 0.05$.	124
Figure 48: Swelling behavior of 3D-printed parts for 5, 10, 20, and 30 days with different AESO loadings.	126
Figure 49: Working curve for pure PEGDA, pure AESO and their mixtures, with AESO concentration varying from 50 wt.% to 90 wt.%.	128
Figure 50: ATR-FTIR spectra of P.A.20:80 sample with varying MCC concentrations. With exception of MCCs, all samples were post-cured under UV light for 40 min (20 min each side).	142
Figure 51: Complex viscosity values of the UV-curable systems as a function of the filler loading in P.A.20:80, where a) corresponds to MCCs and b) to CNCs.	144
Figure 52: Influence of MCC and CNC loadings on P.A.20:80 tensile strength and elongation at break. Statistical analysis for the elongation at break was performed using a one-way analysis of variance (ANOVA) with the level of significance set at probabilities of $p < 0.05$.	146
Figure 53: Young’s modulus values of P.A.20:80 containing different amounts of MCCs and CNCs.	147
Figure 54: Influence of increasing loads of MCCs and CNCs on the P.A.20:80 fracture energy.	148

Figure 55: Typical SEM micrographs of (a,b) unfilled P.A.20:80 and samples containing 0.60 wt.% (c,d) MCC and (e,f) CNC.....	149
Figure 56: Thermogravimetric curves of the resin mixture containing 80 wt.% AESO with varying concentrations of MCC (a,b) and CNC (c,d) in air and N₂ heated at a constant rate of 10 °C·min⁻¹.	152
Figure 57: Water intake of P.A.20:80 with increasing amounts of (a) MCC and (b) CNC over a 30 days period of time.....	153
Figure 58: Working curve for P.A.20:80 with increasing concentrations of MCCs, from 0.15 wt.% to 2.40 wt.%.	156
Figure 59: Working curve for P.A.20:80 with increasing concentrations of CNCs, from 0.15 wt.% to 2.40 wt.%.	157

LIST OF SCHEMES

Scheme 1: Layer-by-layer process of creating an object.	6
Scheme 2: Simplified process of fabricating a part using a 3D-printer: (1-2) designing or scanning the object, (3) converting it to a series of coordinates and (4) printing it.	19
Scheme 3: Free-radical photopolymerization steps: (1) Initiation, (2) first chain and (3) n-chain propagation.....	27
Scheme 4: Effects of oxygen on the photopolymerization reaction.	29
Scheme 6: Simplified description of the preparation and 3D printing process of photocurable systems. The term COMPX refers to PY, IBOMA, and PEGDA.	56